Dissertation

Optimized imaging and post-imaging technologies for the evaluation of biodegradable implants

submitted by

DI Johannes Eichler, BSc

for the Academic Degree of

Doctor of Medical Science

at the

Medical University of Graz

Department of orthopaedic Surgery

under the Supervision of

Assoc.Prof.PD.Dr.med. Annelie-Martina WEINBERG

2016

Eidesstattliche Erklärung

Ich erkläre ehrenwörtlich, dass ich die vorliegende Arbeit selbständig angefertigt und abgefasst und jene Personen und Institutionen, die am Zustandekommen der Forschungsdaten beteiligt waren, namentlich genannt habe. Andere als die angegebenen Quellen habe ich nicht verwendet und die den benutzten Quellen wörtlich oder inhaltlich entnommenen Stellen habe ich als solche kenntlich gemacht. Die Arbeit an der Dissertation und daraus entstandener Publikationen wurde gemäß den Regeln der "Good Scientific Practice" durchgeführt.

Declaration

I hereby declare that this thesis is my own original work and that I have fully acknowledged by name all of those individuals and organisations that have contributed to the research for this thesis. Due acknowledgement has been made in the text to all other material used. Throughout this thesis and in all related publications I followed the guidelines of "Good Scientific Practice".

06.04.2016,	JOHANNES EICHLER
Date,	(Signature)

Danksagung

Zu Beginn meiner Danksagung möchte ich meine Familie erwähnen, die es mir durch ständige mentale und finanzielle Unterstützung ermöglicht hat, mein Studium bis hin zu dieser Dissertation zu absolvieren. Besonders bei meiner Mutter Herta Eichler und meinen Großeltern Hedwig und Andreas Schnaitl möchte ich mich an dieser Stelle nochmals ausdrücklich bedanken. Einen bedeutenden Anteil durch Untersützung bei jeglichen Arbeiten zur Erstellung dieser Dissertation hatten meine Kollegen und Freunde Elisabeth Martinelli, Claudia Kleinhans, Anastasia Myrissa, Stefan Fischerauer und Leopold Berger.

Mein besonderer Dank gilt Annelie-Martina Weinberg, die mit Enthusiasmus und Einsatzfreude meine wissenschaftliche Denkweise geprägt hat.

Table of Contents

Abbreviations

Bin	Binning Level
BR3 (-pol)	ESIN nail made from material BRI.Mag® with 3 mm diameter (-polished surface)
BR45 (-pol)	ESIN nail made from material BRI.Mag® with 4.5 mm diameter (-polished surface)
BV	Bone Volume
BW	Body Weight
Ca	Calcium
ESIN	Elastic stable intramedullary nailing
ET	Exposure Time
FOV	Field of View
Gy	Gray
Gd	Gadolinium
HU	Hounsfield units
M	Mean
Mag	MAgnification
Mg	Magnesium
N	Number

P	Polyhydroxybutyrate
P3Z	Polyhydroxybutyrate with 3w% Zircondioxid
P3Z30H	Polyhydroxybutyrate with 3w% Zircondioxid and 30w% Herafill®
P30H	Polyhydroxybutyrate with 30w% Herafill® powder
PHA	Polyhydroxyalkanoate
PHB	Polyhydroxybutyrate
PLA	Polylactic acid
PLGA	Poly(lactic-co-glycolic acid)
PLLA	Poly (L-lactic acid)
R	Range
RS	Rotation Steps
RD	Rotation Degrees
SD	Standard deviation
SG	Surface gain
Sv of mSv	Sievert or milli Sievert
Ti	Titanium
TV	Total Volume
µCT or micro CT	Microfocus computed tomography
VG	Volume gain
Zn	Zinc
ZX10	Magnesium-Zinc-Calcium alloy

List of Figures

List of Tables

Abstract

Introduction Biodegradable implant materials are subject of intensive research during the last years. Fracture healing after clinical application of biodegradable implants is an important goal to avoid an operation for metal removal and simultaneously improve bone healing through adapted implant rigidity. Acceptance of those materials by bone cells like osteoblasts and osteoclasts is crucial, as well as suitable degradation characteristics and a low and homogeneous hydrogen gas formation, which can not be completely avoided for Magnesium implants.

Materials & Methods Clinical devices for radiological diagnostics were adapted to pre-clinical imaging methods in case of the well known μCT method for high resolution small animal imaging, which was used for implant characterisation during the following studies. Also standard clinical CT method was used successfully with special protocol settings in a large animal model. Another method for tomographic imaging of molecular processes by near infra-red fluorescence in vivo was also used within this work. The in vivo characterization of biodegradable polymers, iron alloys and the latest and very promising Magnesium-Zinc-Calcium alloys by pre clinical and clinical imaging was conducted and evaluated for applicability of those imaging methods. Optimizations of imaging protocol parameters were applied which increased the evaluation accuracy for the different materials. Cylindrical pins were machines of the polymer Polyhydroxybutyrate (PHB) and composites, pure Iron and

Iron-Manganese-(Carbon)-Palladium alloys and the Magnesium-Gadolinium alloy Mg10Gd, as well as the extra high purified Magnesium-Zinc-Calcium alloy BRI.Mag. Implants were inserted into rat tibiae and observed with in vivo and ex vivo imaging methods in μCT and fluorescence molecular tomography. Imaging protocols were adapted to best performance with different implant characteristics like radiological density and bone ingrowth. Furthermore, full-size ESIN implants and interlocking systems, made of conventional Ti were implanted into sheep tibiae and imaged ex vivo in μCT, to evaluate the resulting internal bone damage after mechanical loading. Similar shaped ESIN implants were manufactured from the observed Mg-Zn-Ca materials and implanted into sheep tibiae, to examine degradation, fracture healing and hard- and soft tissue reactions by radiological imaging in a clinical CT device. As a last step, biodegradable screws were manufactured from the Mg-Zn-Ca alloy and tested in sheep tibiae. To ensure a detailed visualisation of the thread-bone interface area, high resolution imaging was performed with the explanted tibiae in μCT.

Results The examined PHB composites exhibited a very low radiological density, which required special protocol settings and high resolution ex vivo scanning to achieve suitable contrast. Addition of ZrO_2 and Herafill led to an distinct increase and made a longitudinal characterization in vivo possible. However, the degradation of the material was found to be very low and the implant volumes were actually increasing over time. Bioresorbable Fe alloys imaging in μCT showed intense metallic artifacts through the high radiological density of the material. Beam hardening filtration and appropriate protocols led to a possible characterization of implant volume and surface parameters ex vivo. The Fe alloy implants were actually expected to corrode within a suitable timeframe, due to several published in vitro results. The μCT results show only minor changes in implant volumes after a period of 52 weeks. FMT results of BRI.Mag (Mg-Zn-Ca) and Mg10Gd materials show an

increase in osteoblast activity for Mg10Gd animals after 8-10 weeks, while BRI.Mag and sham group values did not deviate from the baseline. The corresponding μCT data was used to indicate the very fast an inhomogeneous degradation behaviour of this material. Clinical CT results of ESIN implants, made from Mg-Zn-Ca materials showed the gas evolution and degradation of over a period of 52 and also 76 weeks. Surface treatment by polishing was found to influence velocity and homogeneity of ESIN degradation. Fracture models showed solid callus formation and bone healing between 6 and 12 weeks. BRI.Mag screws, implanted into sheep tibiae, showed different behaviour between polished and unpolished versions after 6 weeks in vivo. Closer bone contact and lower gas formation was found for the unpolished screws.

Discussion PHB implant characteristics were discussed within the publication Meischel and Eichler et al. in [1] and were considered to be unsuitable for orthopaedic load bearing devices due their low rates of bone incorporation on the surface, low bone-implant interface connection and also their low degradation rates in vivo. Actually ZrO_2, which should act as a radiological contrast agent within the composites, was found to introduce higher bone incorporation in combination with the bone substitude material Herafill. The iron alloys within this work were discussed in Kraus et al. [2], where the low degradation in vivo was explained with a lacking oxygen concentration in the surrounding, or the introduction of a protective layer on the implant surfaces. Radiological evaluation in μCT showed metallic artifacts which were definitely reduced by beam hardening filtration. However, accuracy in the bone implant interface areas would still be decreased by remaining artifacts. FMT fluorescence tomography found an increase in osteoblast activity in the Mg10Gd material after 8-10 weeks. The corresponding μCT image shows a very fast and inhomogeneous degradation of this material, which is also applying high gas pressure on the surrounding bone. High osteoblast activity may be a result of high bone turnover during this fast degradation and may indicate an increased repair

activity. The assessment of screw migration after biomechanical testing of ESIN interlocking systems showed differences in internal bone damages, depending on the interlocking type and number of screws. In case of the ender nail, the accuracy of the evaluation may be less through metallic artifacts on μCT images. Clinical CT imaging of full size ESIN implants was suitable for the characterization of implant degradation, gas formation and tissue reactions. The initial surface quality and also the influences on the surface by the surgical implantation process may play a major role in later in vivo behavior. For fracture osteosynthesis, an increase in diameter of the implants is definitely necessary. BRI.Mag screws exhibited a very close bone incorporation in the cortical area. After a chemical polishing process, this contact decreased and may be a result of volume loss by the surface treatment. Very quick overgrow of the screw heads by the periosteum was found for both versions.

Zusammenfassung

Einleitung Die klinische Anwendung von biodegradierbaren Materialien zur Stabilisierung von Frakturen ist ein großes Ziel der langjährigen Forschung im Zuge des Projektes Laura Bassi BRIC. Ein sich auflösendes Implantat erspart eine zweite Operation zur Metallentfernung und wäre daher von großem Vorteil für Patienten und Gesundheitssystem. Die Charakterisierung verschiedenster Biomaterialien im Klein- und Großtiermodell wurde im Zuge dieser Arbeit mit klinischer, radiologischer Bildgebung und auch prä-klinischer Bildgebung durchgeführt. Neben hauptsächlich auf Röntgenstrahlung basierender Verfahren (klinisches CT, klinisches Röntgen und prä-klinisches μCT) wurde das auf nah-Infrarot Fluoreszenz basierende Verfahren der Fluoreszenz Tomographie verwendet, um auch molekulare Prozesse im lebenden Tier beobachten zu können. Seit dem Jahr 2008 wurden innerhalb von Laura Bassi BRIC mehrere Biomaterialien untersucht. Einige davon konnten in dieser Arbeit erwähnt und charakterisiert werden, wie die anfänglich evaluierten Polyhydroxybutyrat Komposite, gefolgt von degradierbaren Eisen Legierungen. Die aktuellsten und vielversprechendsten Legierungen stellen Magnesium-Zink-Calcium Systeme dar. Alle Materialien wurden im Zuge dieser Arbeit durch bildgebende Verfahren evaluiert. Die verschiedenen Parameter der Bildgebung wurden angepasst, um einen höchstmöglichen Informationsgehalt und eine bestmögliche Auswertbarkeit zu erzielen.

Material & Methoden Zylindrische Pins wurden aus den PHB Kompositen, Eisen Legierungen und der Mg-Zn-Ca Legierung BRI.Mag, sowie der Magnesium-Gadolinium Legierung Mg10Gd gefertigt. Nach chirurgischer Implantation in die Femora von wachsenden Ratten, wurde hochauflösende in vivo und ex vivo Bildgebung in μCT und FMT durchgeführt. Die verwendeten Parameter der Scanprotokolle wurden an das jeweilige Implantat angepasst, um optimale Resultate zu ermöglichen. Klinische Titan ESIN Implantate und Verriegelungssysteme wurden in einem Großtier Schafmodell implantiert und mit Hilfe des ex vivo μCT gescannt, um die mechanische Qualität anhand der Dislozierung der Schraube innerhalb des Knochens nach mechanischer Belastung zu analysieren. ESIN Implantate mit gleichen Abmessung wurden im Anschluss aus den im Kleintier getesteten Mg-Zn-Ca Legierungen gefertigt, in Schaf Tibiae implantiert und hinsichtlich ihrer Degradation, Gas Entwicklung, Knochenanwuchs und Frakturheilung getestet. Als bildgebende Methode wurde ein Klinisches CT Gerät verwendet. Aus dem Material BRI.Mag wurden im letzten Schritt resorbierbare Schrauben gefertigt und in Schaf tibiae implantiert. Zur genauen Untersuchung feiner Gewindestrukturen und dem umliegenden Knochengewebe wurden ex vivo μCT scans des explantierten Knochens durchgeführt.

Resultate Die sehr geringe radiologische Dichte von PHB führt zu schlechter Sichtbarkeit durch niedrigen Kontrast bei μCT Bildgebung. Die Beimengung von ZrO_2 und Herafill konnte den Kontrast der erstellten CT Bilder deutlich erhöhen und ermöglichte eine hinreichende Quantifizierbarkeit in vivo. Es wurde eine sehr geringe Degradationsrate aller Komposite innerhalb der Studie festgestellt. Die μCT Bildgebung von bioresorbierbaren Fe Legierungen zeigte starke Artefakte, basierend auf der hohen radiologischen Dichte des Materials. Durch gezielten Einsatz von Beam-Hardening Filtern konnte eine ausreichende Reduktion der Artefakte für die Quantifizierung der Volumina erreicht werden. Die erwartete Resorption der Eisen-

legierungen, die in verschiedenen in vitro Versuchen demonstriert wurde, konnte in vivo nicht beobachtet werden. Das Material zeigte nur geringe Oberflächliche Veränderungen nach 52 Wochen. Die FMT Technologie demonstriert einen deutlichen Anstieg der Osteoblastenaktivität für das Material Mg10Gd nach 8 bis 10 Wochen. Zugehörige μCT Ergebnisse zeigen eine sehr schnelle und inhomogene Degradation des Materials. Im Gegensatz dazu wurde für BRI.Mag ein Aktivitätslevel nahe dem der SHAM Gruppe gemessen. Resultate der klinischen CT Scans von Mg-Zn-Ca ESIN Implantaten ermöglichten die Charakterisierung von Parametern wie Gas Bildung, Degradation, Knochenanwuchs und Frakturheilungsverhalten. Die Behandlung der ESIN Oberfläche durch Polieren führte zu geringerer Gas Entwicklung und verlangsamter Degradation. Ein deutlicher Kallus mit konsolidierter Frakturheilung wurde zwischen Woche 6 und Woche 12 festgestellt. BRI.Mag Schrauben zeigten eine unterschiedliche Reaktion nach chemischer Politur der Oberfläche. Das sehr eng anliegend Knochen Interface bei unpolierten Schrauben wurde nach chemischer Oberflächenbehandlung nicht erreicht. Ein sehr schnelles Einwachsen des Periost über die Schraubenköpfe wurde an beiden Varianten festgestellt.

Diskussion Die Charakteristika der PHB Komposite und deren klinische Anwendbarkeit wurde bereits in der zugehörigen Publikation Meischel und Eichler et al. [1] diskutiert. Eine klinische Anwendung wurde wegen fehlender Bildung von stabilen Knochen interfaces und zu langer Degradation nicht empfohlen. ZrO_2, welches ursprünglich als radiologisches Kontrastmittel hinzugefügt werden sollte, zeigte in Kombination mit Herafill einen erhöhten Knochenabau am Implantat. Die in dieser Arbeit erwähten Eisenlegierungen wurden in Kraus et al. [2] diskutiert und es wurden das Fehlen von ausreichend Sauerstoff im umliegenden Gewebe oder die Bildung einer protektiven Oxydschicht als mögliche Gründe für die langsame Korrosion angegeben. Die metallischen Artefakte während der μCT Untersuchung konnten durch entsprechende Filter deutlich reduziert werden, die Genauigkeit der Methode

im bereich der Übergänge von Implantat zu Knochen muss jedoch weiterhin kritisch betrachtet werden. Es erfolgte jedoch keine Messung eines Knochen-Implantat Interface. Die gemessene erhöhte Osteoblasten Aktivität für Mg10Gd kann möglicherweise mit einem Reparaturvorgang des Knochens nach schneller Degradation und lokaler Deformierung durch hohen Gasdruck erklärt werden. Zugehörige μCT Ergebnisse stützen diese Theorie. Die Evaluierung der ESIN Verriegelungssysteme konnte unterschiedliche Dislozierung der Verriegelungsschrauben festsstellen. Im Fall des Ender Nail ist die Genauigkeit der Quantifizierung durch metallische Artefakte möglicherweise etwas vermindert. Die human CT Untersuchungen von Mg-Zn-Ca ESIN Implantaten im Großtier konnten für die numerische Auswertung von Degradation, Gas Produktion und Reaktionen des umliegenden Gewebes herangezogen werden. Die Beschaffenheit der Oberfläche der Implantate, sowie der Einfluss der Implantation scheint deutliche Auswirkungen auf den späteren Degradationsprozess und die Gasentwicklung zu haben. Zur Stabilisierung von Frakturen wird eine Erhöhung des Nageldurchmessers empfohlen, um die nötige mechanische Stabilität zu gewährleisten. Die chemische Politur der BRI.Mag Schrauben führte zu einem weniger dicht anliegenden Knochen Interface. Als mögliche Ursache könnten ein Volumensverlust durch den chemischen Ätzprozess gesehen werden. Die ebenfalls beobachtete höhrere Gasentwicklung könnte durch Überätzung und die Bildung von Ätzporen in der Oberfläche ausgelöst worden sein.

1 Introduction

1.1 Biodegradable implants for osteosynthesis purpose

In the last years, intensive research work has been performed on the development of novel materials for orthopedic load bearing applications. Especially considering pediatric fracture treatment, there are commonly used osteosynthesis materials like stainless steel and titanium, which will definitely require a second surgical intervention for implant removal. Leaving the implant in the growing skeleton may lead to mild osteoporosis and growth disturbances by stress shielding [3, 4, 5]. This necessary second intervention results in additional stress and pain for the patient, as well as another hospitalisation and therefore absence from school. Osteosynthesis material, which will totally degrade within the child's body and make removal operations obsolete, will be highly beneficial for the patients. A crucial requirement of these new implant materials is at first a well tailored degradation behaviour. The biodegradable orthopaedic load bearing devices should be completely stable at least until a bearing callus formation. Once the bone is able to maintain stability, the implants have to relieve during a controlled timespan. A second very important point is the reaction of immune cells, osteoblast and osteoclast activities near the

implant and the overall process of bone healing and maintenance at the implant site. To gain knowledge about the degradation behaviour and also the bone quality and cell reactions on biodegradable polymers and Iron- or Magnesium alloys used within this work, animal studies have to be carried out. With the combination of suitable surgical implantation methods and the use of powerful imaging techniques, highly valuable results can be achieved for further development of biodegradable implants.

1.2 Radiological examination of fracture healing in clinics

Clinical treatment of trauma cases is performed by either a fracture reduction without an additional intervention, or, if there is a suitable indication, a surgical treatment with the aid of several load bearing implants for fracture stabilization. However, every single method for the treatment of bone fractures requires a distinct overview of the fracture type and composition, to ensure a best effort and minimum invasive procedure. The most common and effective clinical observation methods for trauma imaging are X-ray observations or furthermore computed tomography (CT) imaging. Preferably, X-ray imaging is performed during standard diagnostics because the radiation exposure for the patient is very low, compared to a full CT scan. In contrast to radiation based imaging methods, ultra sound observations and MRI imaging allow exact diagnostics of soft tissue injuries and internal injuries during a trauma case.

1.2.1 Patient exposure to radiation during imaging

Clinical radiological observation always faces a trade-off between maximum diagnostic information by highest possible image quality and the actual dose of radiation acting on the patients body. Distinct representation of detailed structures is often not important for a clinical evaluation and may not justify a higher radiation exposure. The most frequently used technique for the diagnosis of single skeletal injuries is therefore X-ray imaging with a patient dose of 0.2 to 5 milli Sievert (mSv) [6]. This rather small radiation dose enables a suitable spacial resolution and allows a diagnostic assessment for traumatological issues and degenerative or inflammatory bone alterations. Due to the limitation to one single imaging plane of the conventional X-ray technology (2D), an effective and exact observation of complex or multiple fractures may require the use of computer tomography (CT) imaging. Single slices of the designated body area are produced during the scanning procedure and allow images with highly differentiable densities without overlapping of different slices, e.g. costal arch overlapping pleura and lung. A 3D reconstruction of CT slices may ease the spacial imagination and enables an exact treatment. However, the radiation dose of a CT scan is estimated to be around 20x to 70x of the dose emitted by X-ray imaging, depending on the localization [6]. Soft tissue contrast imaging of vascular structures or organs like kidney intestine is possible with the support of radiological contrast agents. However, CT imaging actually lacks in accuracy in the soft tissue domain and requires the use of ultrasound imaging (UI) or magnet resonance imaging (MRI). Both methods for soft tissue examination do not emit any harmful radiation to the patient.

1.2.2 X-ray Imaging

Traumatological observations often require quick diagnosis of skeletal injuries. Fracture gaps of bony structures can be perfectly recognized on the two plane radiographs in anteror-posterior (a.p.) side projection. Various different X-ray imaging systems are existing. On the one hand based on classical X-ray films, which directly show different contrast values based on the energy of the arriving photons, and on the other hand the digital versions, which are able to detect photon energy and display a digital image projection. Nowadays, mostly digital systems are used in routine and images are directly saved in clinical image storage systems like the Picture Archiving and Communication System PACS. However, the basic structure of an X-ray imaging device is still constructed of a generator device with one or more X-ray tubes, a table for patient or specimen, a secondary radiation grid, a dose measuring device and X-ray film or digital CCD (charged-coupled device) sensor based X-ray detector, as described in figure 1.1.

1.2.3 Physical working principle of X-ray imaging

The X-Ray tube(s) inside the generator device contains an evacuated glass cylinder with a cathode coil (Wolfram coil) and an anode (Wolfram plate). The cathode coil is pre-heated by application of a heating current to enable the travel of electrons to the anode side. High voltage potential within a hundred kilovolts range is applied between cathode (-) and anode (+) side and is necessary to accelerate cathode electrons. After their impact on the anode, the electron's energy is converted to X-Ray energized X-Ray photons (braking radiation).

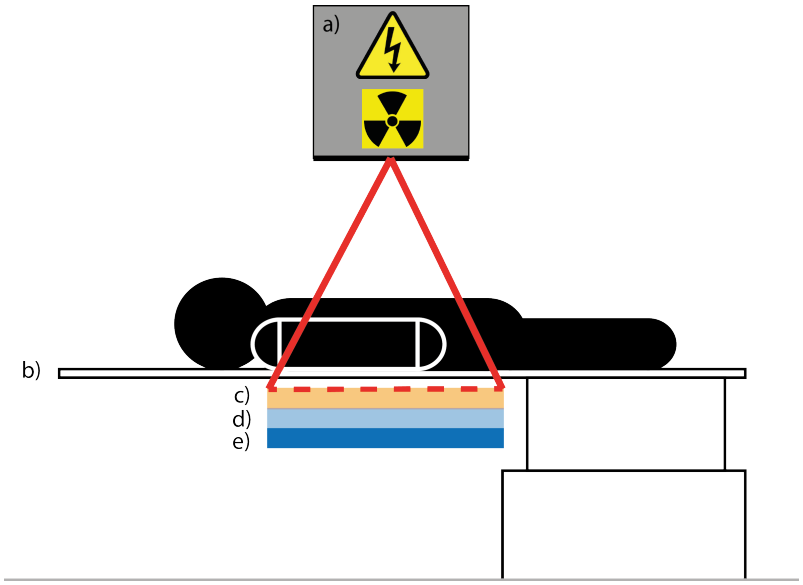

Figure 1.1: Simple setup of clinical X-ray device. a) shows the generator module which is equipped with one or more X-ray tubes and supplied with high voltage b) is the X-ray translucent patient bed c) secondary radiation grid for improved contrast values d) measurement device for radiation dose e) CCD X-ray detector or X-Ray film device

1.2.4 Computed tomography imaging

Computed tomography imaging is based on the working principle of X-ray photon generation described in section 1.2.3. Tomography imaging is based on an X-ray source and X-ray detector, mounted on a rotating gantry in opposite direction facing each other. In the centre of the rotating gantry, the patient is placed on a table which may be moved in horizontal and vertical direction. In contrast to planar X-ray radiography, CT imaging will capture 360 or more images during a full gantry rotation around the patient. Projections at all positions during the scans are saved and reconstructed by special algorithms, in order to create a three dimensional view out of corresponding slices along the axial pane.

1.2.5 Pre-clinical imaging for the characterization of degradable implant materials

The principles of X-ray and CT imaging, known from clinical devices were adapted to achieve higher resolution with a smaller field of view (FOV) for small animal imaging in a sub micrometer region, like described in Li et al. and Feldkamp et al. [7, 8]. High resolution and high amount of details in the resulting images are closely connected to a mentionable dose of radiation, which is actually around 500-1000 times higher than in clinical imaging. Another method for pre-clinical imaging uses the spectrum of infrared light, which easily travels through tissue to create a tomographic view of molecular processes at an implant site.

1.2.6 Metallic implants and beam hardening artifacts

One major disadvantage of imaging metallic implants with polychromatic x-ray based devices like the Siemens Inveon μCT is the appearance of metallic artifacts during the scan. While magnesium alloys do not produce beam hardening artifacts, implants made of iron, stainless steel or titanium cannot be imaged adequately without special dispositions. Polychromatic x-rays can be roughly categorized into hard (high-energy), medium and soft (low-energy) photons. Low-energy x-rays will be scattered easily by dense metallic implants, which causes artifacts. Very low energy x-rays also won't be able to pass through tissue and will be absorbed at site, which increases the risk of tissue irritation and cancer. Low-energy x-ray photons are therefore filtered by different setups with various thicknesses of metal plates like aluminum or copper. Those filter plates are placed directly after the x-ray tube's outlet and significantly reduce artefact forming soft photons with the consequence of a lowered signal to noise ratio, depending on the filter thickness [9]. The only way to reduce metal artifacts to a minimum, is using an adjustable monochromatic x-ray source, which is provided by synchrotron μCT (SRμCT) devices and allows tomography in nanometre scale and a distinct comparison to histological observation [10, 11]. However, most applications for bone-implant research within this work can be perfectly covered by the used Siemens Inveon μCT device. In addition to first hardware-based artefact reduction steps by filtering, also software based corrections can be applied during data reconstruction. This "beam hardening correction" algorithms are controversially discussed in literature and may be not useful in every case [12].

To decrease the value of low energy photons, the Siemens Inveon μCT device offers aluminium filters with a thickness setting of 0 mm, 0.5 mm, 1 mm and 1.5 mm. The standard setting is 0.5 mm to avoid very low energy photons, especially for in

vivo scans. Depending on the upcoming artifacts, filter thickness has to be increases to 1 mm or 1.5 mm when scanning metallic implants. Artefacts, which could not be avoided during the scan, can be corrected using the according option during reconstruction in Inveon Acquisition Workplace. However, beam hardening correction algorithms do not seem to be useful in every case. This technique is very dependent on the knowledge of x-ray spectrum and tries to linearize end estimate the actual travelling of the x-ray photons through the material. With this information, beam hardening correction gives the possibility to increase image quality, but not definitely the accuracy [12]. In case, the region of interest is at the bone implant interface, beam hardening correction may not be useful.

1.3 Important issues and revision process during implant development

Several implant materials and stages were radiologically observed and characterized within the Laura Bassi centre BRIC, while they underwent a continuous revision process. Few of them will be part of this work and were characterized using state of the art pre-clinical and clinical imaging in laboratory animal models. In the first stage, bioresorbable polymers were examined followed by degradable Iron alloys. Too long degradation behaviour and other non-ideal characteristics led to the development of biodegradable Magnesium alloys for orthopaedic application. Magnesium-Zinc-Calcium systems were produced extra high purified (99.999998 % purity) by the ETH Zurich within Laura Bassi BRIC, in order to achieve a controlled degradation rate without the alloying of rare earth elements, which may be noxious for the human body and not applicable for a growing skeleton.

1.4 Aims of this thesis

Within this work, several studies were conducted on different metallic materials like Magnesium alloys, Iron (Fe) alloys, Titanium and also non-metallic materials like Polyhydroxybutyrate (PHB) composites. In consequence to a progressive materials development during the whole study period, different animal models like rat or sheep model with various implant shapes and sizes have been processed to address all the full spectrum of the more and more sophisticated material. To finally achieve the main goal within the project Laura Bassi BRIC, a clinically safe and certified bioresorbable screw, in vivo and ex vivo imaging was conducted to characterize every materials properties.

1.4.1 Aim 1: Radiological observation of degradation and interface characteristics of Polyhydroxybutyrate (PHB) composite materials

Clinically used polymers like PLGA, PGA and PLA are a widespread standard material e.g. as degradable suture, scaffolds or drug delivery systems. The degradation behaviour of those materials is known to be acidic, which may induce tissue irritations and is not considered to be desirable. PHB degrades by hydrolysis and does not change the local pH milieu during this process. It seems to be a highly promising material, which can be produced from renewable resources [13] and endotoxine-free [1] from the cytoplasm of Escherichia coli bacteria. To evaluate the degradation behaviour of PHB materials, a bone-pin in vivo model was established and observed via medium and high resolution micro computed tomography (μCT) imaging. As shown by Meischel, Eichler et. al. in [1], radiological observation of native PHB is challenging due to poor contrast and visibility in longitudinal in vivo scans. To

increase accuracy of μCT imaging, Zirconium dioxide (ZrO_2) was added to the composite material to act as a radiological contrast agent. Scanning parameters were adapted to gain maximum information on radiological contrasts between bone, implant and the corresponding interface areas. A successfully optimized radiological characterization of the implant parameters with respect to a possible application as orthopaedic load bearing should be achieved.

1.4.2 Aim 2: Characterization of degradation behaviour of biodegradable iron (Fe) alloys under assessment of μCT based volume and surface data in vivo

Another promising candidate for orthopaedic implants was degradable Fe, which was proven to be non toxic and does not cause inflammatory reactions in pre-clinical animal trials, which were published in [14, 15]. Toxicological results in coronary stent application suggest that the material may be also suitable for orthopaedic load bearing devices. However, stent experiments show a very low degradation rate with the presence of the material after one year. Additionally, pure Fe might not show enough strength for orthopaedic application and can be reinforced by the alloying elements Manganese (Mn) and Palladium (Pd) [16, 17]. A small animal study was conducted and already published in Kraus et al. [18], in order to evaluate the in-vivo degradation behaviour of Fe-Mn-Pd alloys, which showed superior mechanical performance and suitable degradation rates during in vitro experiments in Hermawan et al. [16]. Radiological characterization was done by in vivo and ex vivo μCT scans, with special attention to a suitable radiological contrast and a best effort reduction of beam hardening artifacts caused by dense metallic implants. The mentioned corrections and protocol settings should result in mostly artefact free results for distinct evaluation of the material parameters.

1.4.3 Aim 3: Fluorescence Molecular Tomography (FMT) in transcortical rat model with osteoclast and osteoblast activity labelling fluorescent imaging agents in combination with micro CT imaging

The pre-clinically used imaging technique μCT is considered to be an exact and mighty tool for the assessment of longitudinal in vivo studies [8]. By the use of medium- and high-resolution imaging, the characterization of degradable implant materials in an in vivo or ex vivo animal model is possible during earlier stages of material degradation. However, observing degradable Mg implants within a long-term rat model over a period of 18 months and longer will be challenging due to the formation of a Magnesium hydroxide $Mg(OH)_2$ layer during degradation and the increased formation of new bone at the same site [19]. In order to give a clear statement about the local content of new bone in comparison to implant residuals, histological observation of sacrificed and harvested bones is necessary. See also fig. 1.2. To solve this problem, the method of fluorescence molecular tomography (FMT) imaging was evaluated in a pilot study with two groups of biodegradable materials, in order to quantify the local activity of osteoblasts and osteoclasts. Special imaging target agents were injected and scans were performed in μCT and also FMT at the same timepoints. The combined usage of both technologies should be able achieve information on the amount of new bone formation from molecular processes in combination with the spacial information from μCT.

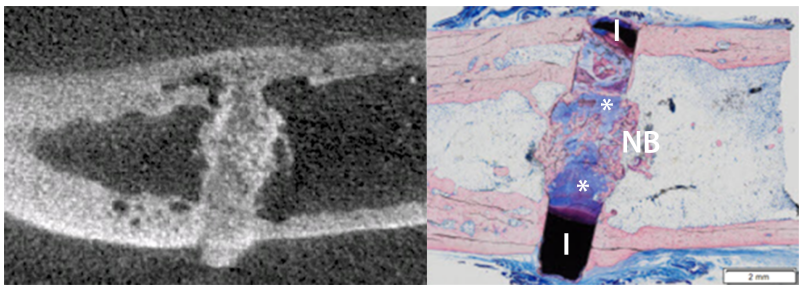

Figure 1.2: In vivo long term evaluation of biodegradable Mg implant WZ21 after 15 months in comparison to the corresponding histological slice. Histology shows a clear bone formation (NB) around the Mg implant residuals in the medullary cavity (*). Remaining implant parts in the cortex are marked with I. At this stage of degradation, a quantitative analysis of implant volume and surface via in vivo μCT data may not give correct values.

1.4.4 Aim 4: Micro CT supported biomechanical evaluation of ESIN interlocking systems in cadaveric sheep tibiae

ESIN (Elsastic Stable Intramedullary Nailing) osteosynthesis represents a common gold-standard method in paediatric traumatology. For a minimal invasive treatment of diaphyseal tibia or femur fractures, the ESIN method is highly beneficial in comparison to rigid plate osteosynthesis or external fixation. Compression plate osteosynthesis is known to induce direct bone healing by stiff fixation and compression of fracture ends [20]. It is also known that a too rigid fixation will retard bone healing because almost all load bearing is provided by the implant itself, which prevents the bone of being reinforced accordingly. This phenomenon is called stress shielding [3] and can be avoided by choosing a system with lower rigidity. Due to the fact external fixation offers the possibility to adjust its rigidity, they offer various possibilities to apply customized fixation. Bone reunion behaviour will be a

combination of direct and secondary healing, while the direct phase was shown to be dominant [20]. However, external fixation devices are invasive and their effectiveness is highly dependent on the surgeons expertise. The ESIN method offers a suitable stabilization without a too rigid fixation by inserting two or three pre-bent nails into the medullary cavity via two small incisions. Applied load is passed partly to the fracture ends which results in secondary bone healing and faster time of reunion [20, 21, 22, 23]. After ESIN treatment, fracture healing is initiated and callus formation starts, following different stages in size and mineralization. To achieve a reliable characterisation of callus healing stages with the Ti ESIN gold standard, distinct observation of radiological density was necessary. However, density values do not correlate with the overall callus loading capacity in every case [24, 25].

Paediatric long bone fracture treatment with elastic stable intramedullary nailing (ESIN) osteosynthesis leads to a very high reunion rate of 99.5 % [26]. However, irritation by prominent nail ends and also nail migration are an issue and may lead to complications and early implant removal [26]. The risk of possible mechanical load bearing complications increases significantly with a body weight of the paediatric patient above 40 to 45 kg [27]. To improve load bearing capacity and concurrently avoid prominent tissue irritating nail ends, locked ESIN may be used. Several different interlocking systems are available on the market, featuring multiple sizes, shapes and screw types. To actually quantify the mechanical load bearing capacity and further the superiority of different interlocking systems, radiological evaluation was considered. In addition to biomechanical data, screw migration and displacement should give insights into structural changes inside the bone by heavy overload.

1.4.5 Aim 5: Clinical CT imaging of degradable Magnesium ESIN Implants in the growing sheep model

Besides excellent results in reunion rate [26] and a good compensation of stress shielding [3] by fixation with Ti ESIN nails, one major problem can not be avoided. While a secondary implant removal operation is not definitely recommended without clear indication in mature patients [28], it is widely supported by paediatric surgeons [29]. Nevertheless, a relatively high risk of re-fracture during implant removal, irritation of healed soft tissue [30, 29] and also a high burden for hospital capacity is caused by metal removal operations. However, an introduction of biodegradable ESIN implants would render those second operations for implant removal and also make those controversially discussed topic obsolete. A major drawback of biodegradable Mg implants was their too rapid degradation and led to the frequent addition of rare-earth (RE) elements, which are considered to be noxious and highly inappropriate for a growing skeleton [31]. Desired RE-free biodegradable Mg implants which are also usable in paediatric fracture treatment led to the development of Magnesium-Zinc-Calcium (Mg-Zn-Ca) alloys. The first generation was named ZX50, which contains 5 wt.% of Zinc. ZX50 showed way too high degradation rates in Kraus et.al. [18] and was not considered for further implant application. The next generation of Mg-Zn-Ca materials was developed containing a lower amount of 1 wt.% Zn and was referred to ZX10 [32]. Another purification step was added to the material processing chain, to ensure a maximum of homogeneity and a further lowered degradation speed [33], which led to the engaged biodegradable ESIN materials ZX10 and ZX00 or BRI.Mag®. To ensure a clinical applicability after promising results during small animal studies, full size ESIN implants had to be tested and characterized in vivo to examine implant performance. Radiological assessment of degradation characteristics, gas evolution and bone or tissue reactions was conducted continuously in human CT, further distinct evaluation was done after euthanasia and explantation

in μCT.

1.4.6 Aim 6: Micro CT ex vivo characterization of BRI.Mag® screws in ovine metaphyseal, epiphyseal and diaphyseal tibia

Additionally to common ESIN osteosynthesis for (especially paediatric) long bone fractures, also other indications may benefit from bioresorbable material instead of stainless steel or Ti implants. Screw osteosynthesis in non-heavy load-bearing applications makes a possibly indicated second operation for implant removal obsolete. Also possible tissue irritations and palpable screw heads, which may be irritating at some locations like cubital joint, ankle joint or finger will be a thing of the past. First bioresorbable screws were produced from polymers and are available on the market. Poly-Lactic-Acid (PLA), Poly-Lactic-Glycolic-Acid (PLGA) and Poly-Glycolic-Acid (PGA) are well known screw materials and are used in clinical treatment of non load bearing fractures or ligaments. As an unwanted side effect, their hydrolytic degradation induces an acidic pH value and causes mild inflammatory reactions [34, 35]. Biodegradable Mg implants offer suitable alternatives to polymer screws due to their faster degradation performance and the fact they do not cause local inflammations. Also radiological observability in CT and μCT devices of polymer implants is really poor [36]. Actually, there is one bioresorbable Mg screw on the market for operational treatment of hallux valgus [4]. In contrast to this non RE-free screw MAGNEZIX®, which is produced by the company Syntellix, the observed BRI.Mag® screws within this study were alloyed RE-free. In respect to size and shape of Mg screws, clinical CT scans offered a too low resolution for the distinct qualification of the bone interface and the implant's degradation behaviour. Explanted sheep tibiae were scanned in μCT and screw characteristics were

quantified accordingly. Additional biomechanical testing was conducted by the TU Wien (Vienna, Austria) in comparison to non-resorbabale Ti screws. This study was conducted, in order to assess the BRI.Mag® materials' capability regarding implantation and handling, as well as degradation behaviour, gas evolution and strength with regard to clinical application.

2 Materials and Methods

2.1 Implants

The implant shapes and materials used within this thesis are divided into two main groups: Implants for large animal studies in the growing sheep model (see 2.4) and implants for small animals (see 2.3) in the growing rat model. Small animal implants are further devided into subgroup 1, which contains biodegradable polymers, while subgroup 2 consists of biodegradable metal implants. In case of large animal implants, two other material groups were defined. Subgroup 3 once more contains degradable metals, while subgroup 4 shows a set of non-degradable metals.

2.1.1 Pins used in small animal experiments

The PHB composite implants in Fig. 2.1 a) were developed and manufactured by the Applied Physiology research group at the Institute of Biotechnology and Biochemical Engineering and the Institute for Chemistry and Technology of Materials at Graz University of Technology. Five different composites were examined during this work. Native PHB (P), PHB with 3% zinc content (P3Z), PHB with 30% Herafill® (P30H), PHB with 3% Zinc plus 10% Herafill® (P3Z10H) and PHB with 3% Zinc and 30% Herafill® (P3Z30H), like described in [1] and [37]. All used metal-

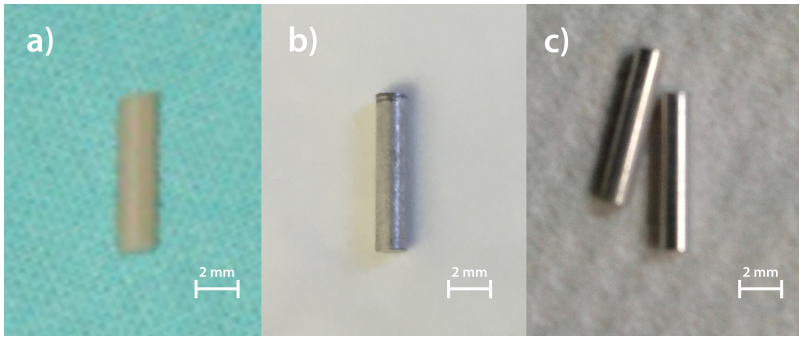

Figure 2.1: Cylindrical pins were manufactured with 1.6 mm diameter and 8 mm length for the implantation into a rat femur. a) shows a PHB composite pin, b) was manufactured from a pure Mg alloy and c) shows a pin made from an Fe alloy. The Mg pin on picture b) shows slight corrosion attacks, caused by storing at standard air environment.

lic small animal implants 2.1 b) and c) were delivered by the Laura Bassi BRIC project partner organisation ETH Zurich and were, like the polymer composites, machined to cylindric shape with 1.6 mm in diameter and 8 mm in length. Three different Mg alloys (Fig. 2.1 b)) were used for small animal experiments in vivo: XHP BRI.Mag® (MgZn0,3Ca0,4 also known as ZX00), XHP ZX10 (MgZn1Ca0,3) with a higher content of Zinc and a lower content of Calcium (both alloys developed and supplied by Laura Bassi BRIC project partner ETH Zurich) and the Magnesium alloy Mg10Gd, which contains 10 percent Gadolinium and was provided by the Marie Skwodowska Curie fellowship program Magnim (Geesthacht, Germany) [38]. Another three different Fe alloys (Fig. 2.1 c)) were used with a composition of pure Fe, Fe-10Mn-1Pd and Fe-21Mn-0.7C-1Pd, like described in Kraus et al. [2].

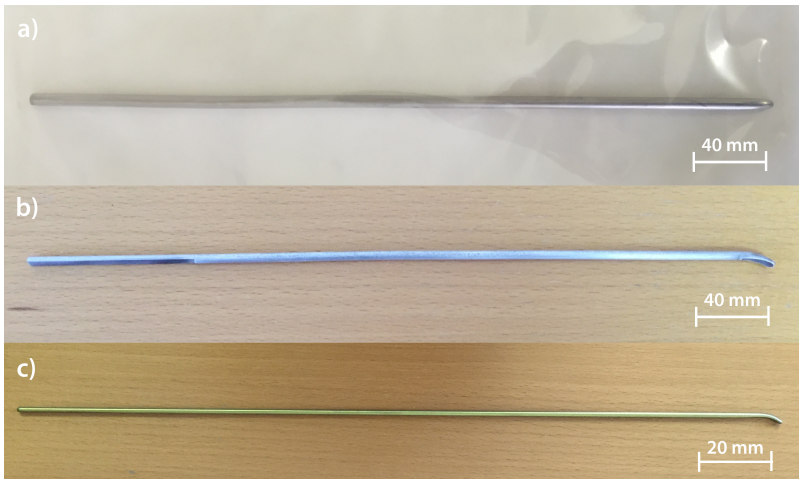

Figure 2.2: Three different ESIN implant shapes were used during the study. a) shows an implant manufactured out of XHP BRI.Mag with 4.5 mm in diameter an 200 mm in length. This implant has a rounded tip to ease the implantation procedure and ensure easy sliding into the medullary cavity via a small incision into soft tissue and bone. b) shows an ESIN nail made of XHP ZX10 with 3 mm in diameter and a length of 200 mm. The implant has a shovel tip, like the gold-standard Ti ESIN in picture c), which shows a standard ESIN Ti implant with a diameter of 3 mm and a lenth of 400 mm.

MODEL	Small Animal				
MATERIAL	Degradable Metal (Mg Alloy)			Degradable Polymer	
SHAPE	Pin 1.6 mm x 8 mm			Pin 1.6 mm x 8 mm	
IMAGING	*In Vivo* continuous µCT	*Ex Vivo* Highres. µCT	FMT	*In Vivo* continuous µCT	*Ex Vivo* Highres. µCT

Figure 2.3: The small animal model was used with a transcortical implantation of cylindrical pins, made of biodegradable metal and biodegradable polymers. In vivo and ex vivo imaging methods were performed at different levels of resolutions and details.

MODEL	Large Animal									
MATERIAL	Degradable Metal (Mg Alloy)						Non Degradable Metal (Ti)			
SHAPE	ESIN 3 mm		ESIN 4.5 mm		Screw		ESIN 3 mm + Interlocking		Screw	
IMAGING	*In Vivo* Continuous Human CT	*Ex Vivo* µCT	*In Vivo* Continuous Human CT	*Ex Vivo* µCT	*In Vivo* Continuous Human CT	*Ex Vivo* µCT	*Ex Vivo* Radiograph	*Ex vivo* µCT	*Ex Vivo* Radiograph	*Ex Vivo* µCT

Figure 2.4: A growing sheep model was used to conduct experiments with degradable metal implants made of Mg alloys and the non degradable gold-standard metal Titanium. Degradable ESIN implants in sizes 3 mm and 4.5 mm were used, as well as screw and interlocking systems.

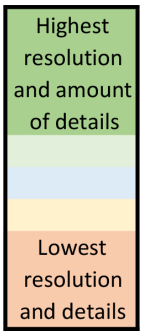

Figure 2.5: The most accurate and detail-rich method used was the ex vivo high resolution μCT imaging. Followed by medium resolution in vivo online monitoring and ex vivo imaging of larger samples like explantet sheep bones. The lowest contrast and resolution method was the standard clinical radiograph.

2.1.2 Biodegradable ESIN implants used in ovine large animal experiments

Besides the primary testing of Mg alloy's behaviour in the growing Sprague Dawley® rat model, implant materials with superior characteristics in degradation rate, hydrogen gas evolution and also mechanical characteristics were selected for further tests in a more clinically relevant large animal model [31]. ESIN nails with 3 mm, as well as 4.5 mm in diameter and 200 mm in length were produced by extrusion of the raw materials. 3 mm nails were extruded from the materials BRI.Mag® and ZX10, 4.5 mm ESIN nails were produced from BRI.Mag® only. The 4.5 mm nails were designed with an alternative tip, which was rounded (see fig. 2.2 b)) and should provide an easy implantation by a "slippery" tip within the medullary cavity. The 3 mm implants were designed to follow the well known Ti ESIN design with a shovel-formed tip (see fig. 2.2 b) and c)) for an easy insertion and sliding inside the medullary cavity [27]. The conventional Ti ESIN rods with a diameter of 3 mm and a length of 40 mm (see fig. 2.2 c)) were used as gold-standard control in comparison to degradable ESIN rods.

Mg ESIN surface treatment

It is already known that the content of impurities within Mg alloys is essential for the later degradation behaviour, due to its influence by micro galvanic corrosion. Hofstetter et al [33, 39] showed exactly this influence through the example of the fast degrading material ZX50. Ultra high purified Mg materials were used for the manufacturing of ESIN nails for this study, however, also the condition of the implants' surface may play a major role for the initial degradation behaviour. Unwanted residuals may lead to a local microgalvanic corrosion and influence the degradation rate

and furthermore the implants stability in vivo. The used Mg ESIN implants were used as-extruded and also surface treated. ESIN surface treatment was performed manually by grinding with abrasive paper SiC (Silicium-Carbid) 4000, to remove unwanted residuals of extrusion tools or other impurities on the Mg implant surface. After extrusion or grinding procedures, all implants were finally cleaned in pure ethanol.

Implant packaging and sterilization

All implants were double-packaged, suitable for sterile surgery, in gamma sterilizable peel bags by the company Biegler GmbH. Packaged implants were sent to Mediscan GmbH & Co AG for gamma sterilization with a dose of 25 kGy. Conventional Ti implants were cleaned and steam sterilized within the unit for conditioning of medical products directly at the Medical Universtiy of Graz.

2.1.3 Biodegradable screws usesd in ovine large animal experiments

Furthermore, extruded 4.5 mm and 6 mm rods were used for dry-machining of BRI.Mag® screws (BRI.Screw) with a diameter of 3.5 mm and a length of 16 mm (see 2.6 a)). The manufacturing process of the screws was conducted by the partner organisation Ernst Wittner GmbH. Special attention was paid to a neat manufacturing process with clean tools. The first generation of 16 mm BRI.Screws (fig. 2.6 a)) was manufactured with a standard steel thread cutting tool. For the most recent generation with a length of 24 mm and 29 mm (see 2.6 b) and c)), a special diamond thread cutting tool was used, in order to ensure an exceedingly perfect surface without any further surface treatment. Mg10Gd screws were provided by the

partner project MetBioMat - Virtual Institute, which is located at the Helmholtz Zentrum Geesthacht (Geesthacht, Germany). The screws were manufactured by the company AAP with a length of 30 mm and a diameter of 3.5 mm. In contrast to all used BRI.Screws, the Mg10Gd charge (see fig. 2.6 d)) was designed self-tapping and uses a similar thread like the conventional 30 mm Ti screw (see fig. 2.6 e), left).

Surface treatment of Mg screws

The outline of biodegradable fixation and compression screws is extremely complex in comparison with an simple ESIN rod. Manual polishing with SiC 4000 sandpaper is not possible inside the small structures of the threads. However, the decision to perform surface treatment for the removal of manufacturing residuals and other impurities was made with regard to an optimum surface quality for a later clinical application. A special method for chemical polishing was developed at the ETH Zurich and performed with BRI.Screws with a length of 16 mm.

2.1.4 Non-biodegradable ESINs, screws and interlocking systems used in ovine large animal experiments

Besides biodegradable Mg implants, conventional Ti ESIN rods (see fig. 2.2 c)), screws (see fig. 2.6 e) and f)) and interlocking systems (plugs), which are used in clinical routine, were implanted in large animal studies.

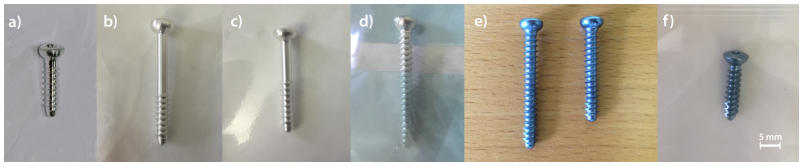

Figure 2.6: a) XHP Mg BRI.Screw 16 mm thread length, 3.5 mm diameter b) XHP Mg BRI.Screw 29 mm thread length and 3.5 mm diameter. Non self cutting design. c) XHP Mg BRI.Screw 24 mm thread length and 3.5 mm diameter. Non self cutting design. d) shows an Mg10Gd (Helmholtz Zentrum Geesthacht, manufactured by AAP) screw with a thread length of 30 mm and self cutting design. Images e) - f) show standard titanium bone screws with 3.5 mm in diameter and thread lengths of 30 mm, 24 mm and 16 mm.

2.2 X-ray Micro Tomography

Micro CT is a highly valuable method for performing non-invasive and non-destructive imaging in living organisms [8, 40], but also offers a high accuracy for the analysis of explanted bone samples and other materials. During a full micro CT scan with the used Siemens Inveon scanner (see fig. 2.7) the animal or sample will be placed on a movable bed. In case of a living animal, inhalation anaesthesia with volatile Isoflurane will be applied during the whole procedure using an adequate inhalation mask for small animals. Also a bore tunnel with an inner diameter of 12 cm will fixated inside the scanner and used to avoid the animal falling into the device in case of too slight anaesthesia. Actually, only low and med-low magnification settings can be used with the installed bore tunnel to avoid damage of the gantry.

The micro CT scanner uses a combination of the techniques of clinical X-ray and the spiral CT devices. While the patient is not moved during a standard clinical radiograph, a clinical CT device will perform continuous rotation of the scanners

Figure 2.7: The Siemens Inveon micro CT scanner with the team of Laura Bassi BRIC.

gantry and move the patient bed during the scan. This procedure results in a spiral scanning pattern. The Siemens Inveon micro CT device uses a fixed position of the sample during a full rotation of the gantry, creating 360 or more projections of the same site.

Figure 2.8 shows a scheme of the used Siemens Inveon micro CT device where the left side represents an side view of the device and the right side shows an axial view from the device front. The rotatable gantry a) can freely move around the sample over 360° with an adjustable step size, up to 3600 steps which equals a minimum rotation step size of 0.1°. The animal or sample b) is placed on a movable bed e), which can be moved in horizontal and vertical direction inside the gantry with an accuracy of 0.1 mm, which allows an exact placement. The X-ray source d), which is a standard Tungsten anode with a focal spot size < 50 µm [41], is mounted directly on the rotating gantry and is movable towards and away from the centre. The detector on the opposite side of the X-ray source is constructed of an 125 mm

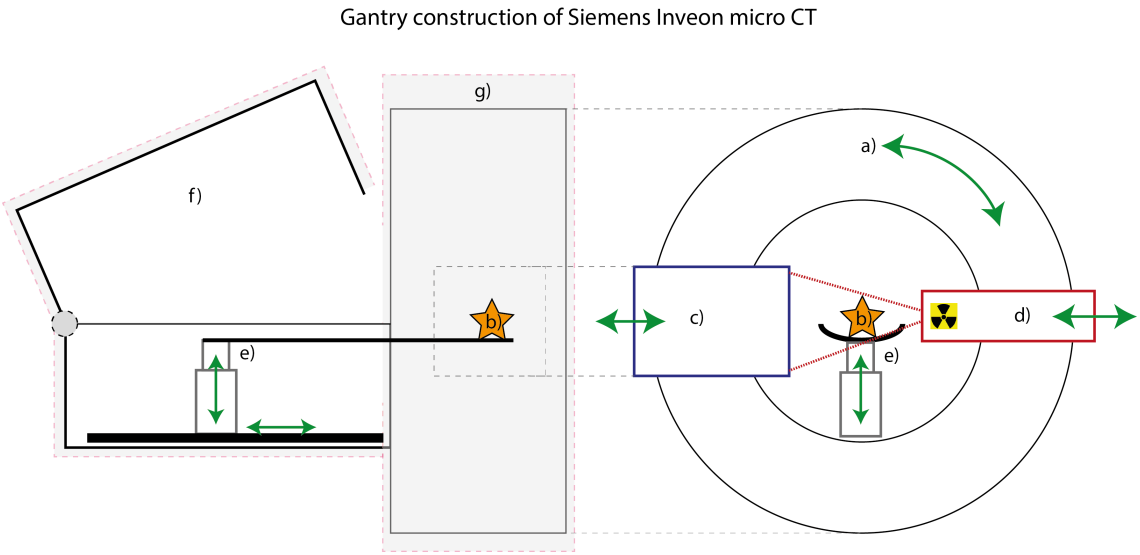

Figure 2.8: The Siemens Invon micro CT device consists of a rotatable gantry (a), a movable bed (e) where the animal or sample (b) is placed during the scan, a movable X-ray source (d) and a movable detector (c). The device is fully shielded (g) to prevent any radiation outside the gantry and has one shielded door (f) to allow sample placement.

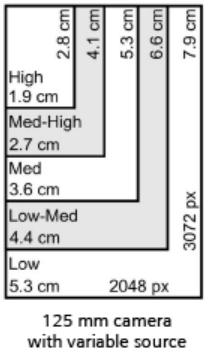

Figure 2.9: Five different magnification steps may be set by using the movable detector and source combination. The different stages of magnification have influence on the imaging accuracy, due to the constant detector pixel range of 2048 px x 3072 px. Image from Siemens Inveon User Manual [41].

X-ray camera with a pixel spacing of 32 microns [41] and moves on the same axis like the source. In combination, this source-detector system allows the setting of five different magnifications which are: low, med-low, medium, med-high and high magnification. The corresponding field of view (FOV) size for the resulting μCT scan is displayed in fig. 2.9. The resulting optical resolution will therefore be calculated regarding to eq. 2.1, for example a magnification setting of "high" will result in a resolution of 9.277 μm per voxel.

$$Size_{voxel} = \frac{length_{FOV-horizontal}}{2048px} = \frac{length_{FOV-vertical}}{3072px} \tag{2.1}$$

2.2.1 X-ray filtration setup

To ensure an optimal scanning result, the Siemens Inveon μCT X-ray source is equipped with a variable aluminium filter plate, which is known to be an optimal

material for filtering soft X-rays [42], at the source outlet. Filter thicknesses of 0.5 mm, 1.0 mm and 1.5 mm allow the selection of an ideal spectrum of photon energy for the current scanning protocol and type of sample. Also a setting with no filter applied is available and leads to the occurrence of the full x-ray spectrum (see fig. 2.12).

Hardness of radiation, biological effects and beam hardening

To achieve the maximum imaging quality available with the Siemens Inveon device, using a high value for X-ray acceleration voltage is mostly beneficial. A setting of 80 kV will ensure the maximum of photon acceleration and provide a broad spectrum of soft radiation (low-energy photons) to hard radiation (high energy photons), like described in fig. 2.12. Due to the fact that low energy photons will be absorbed easily in the specimens tissue and do not contribute to contrast in the final image, at least a filter setting of 0.5 mm aluminium must be chosen, in order to reduce the biologically effective radiation dose and also the total dose. Actually a filtration setting of 1.5 mm aluminium is recommended for clinical application with a tube voltage between 50 kV to 70 kV. 80 kV and above will require 2.5 mm to reduce a skin dose up to 80 percent [43, 7]. When using very dense metal implants like stainless steel or titanium, high-energy photons are mandatory to ensure suitable imaging quality. Soft radiation is scattered by the metallic implant and leads to the appearance of beam hardening artifacts within the image. Figure 2.10 shows an example of an iron implant in a femoral rat bone after 1 month. The effects of too low filtration and beam hardening artifacts, which annihilate necessary contrast values of the achieved projections in the bone implant interface area, can be clearly noticed. Huge black areas around the implant were marked with yellow arrows in fig. 2.10. In consequence, the maximum filter setting of 1.5 mm was applied and the same scan protocol setting of 80 kV and 500 µA) was used in fig. 2.11, which

also displays a femoral rat bone with a similar iron implant after 1 month.

However, filtration always leads to an absorption of photons and furthermore to lower differences in contrast [9], which is also noticeable in fig. 2.11. Due to the characteristics of the X-ray spectrum of a polychromatic source in the Siemens Inveon scanner, beam hardening artifacts cannot be avoided completely by filtration. The remaining amount of low-energy photons will still produce artifacts, which are actually reducible with different reconstruction and software post processing approaches [44, 40]. Within this work, all μCT scans were reconstructed using filtered backprojection and Feldkamp algorithm in Siemens Inveon Acquisition Workplace, ver. 2.0.

2.3 Surgical implantation procedure and housing for small animal experiments

The surgical implantation process in the growing Sprague Dawley® rat was performed by following a standard implantation protocol according to Meischel and Eichler et al. [1] and Kraus et al. [2].

Pre-medication and anaesthesia was started with inhalation narcosis by volatile Isolflurane (Forane®, Abbot AG, Baar, Switzerland) and was followed by the introduction of a general anaesthesia by a mixture of 1 part Fentanyl as painkiller, 1 part Midazolam as muscle relaxant and 0.5 parts Domitor as narcotic. 0.1 ml per 100 g bodyweight (BW) were injected subcutaneously in the animal's neck. Body temperature was constantly monitored and maintained at 37 °C to avoid hypothermia during and after the surgical intervention.

A surgical approach was conducted from the lateral side at the middle diaphysis of

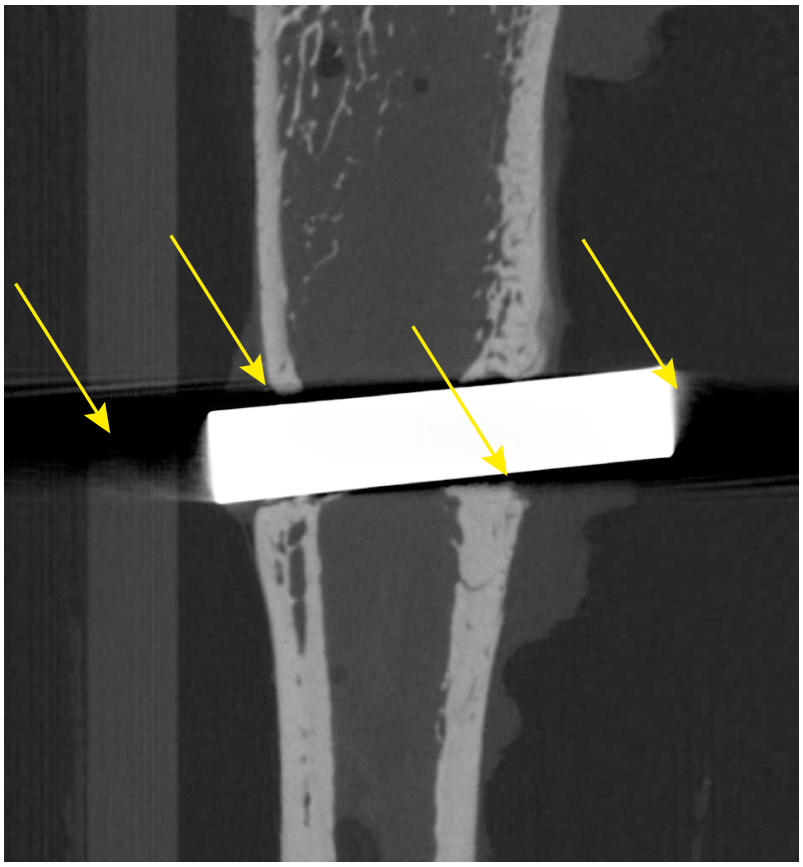

Figure 2.10: The image of a femoral bone of a Sprague Dawley rat contains a common cylindrical implant (iron, 8 mm length, 1.6 mm diameter) and was images after 1 month after the operation. A high resolution imaging protocol was used with a voltage setting of 80 kV and 0.5 mm aluminium filtration on the Siemens Inveon *mu*CT scanner. The yellow arrows mark beam hardening artifacts, which appear as black marge around the intensively glowing implant. The bone-implant interface can not be characterized in a appropriate way with this setting.

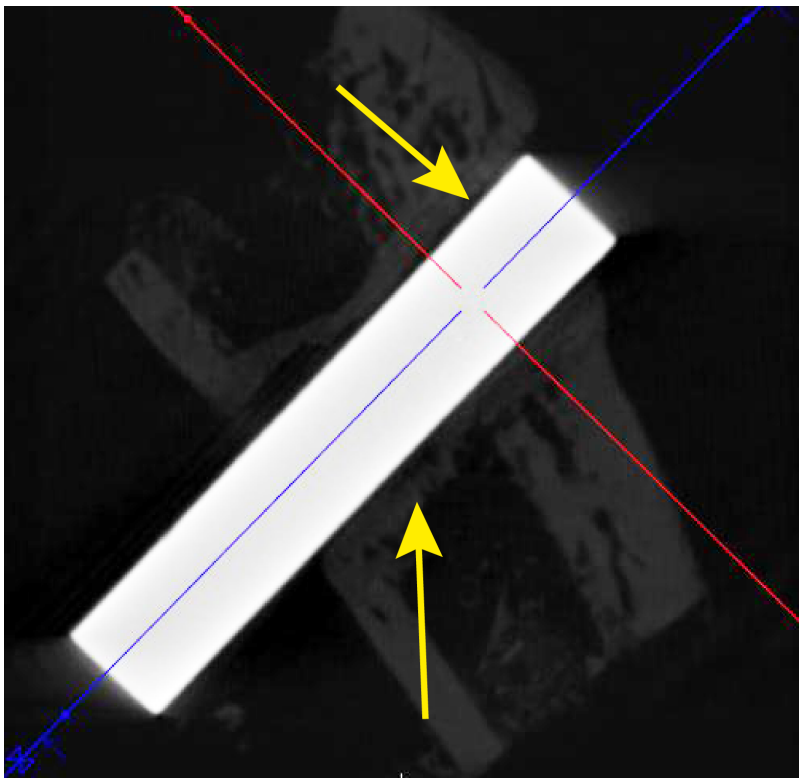

Figure 2.11: 1.5 mm aluminium filtration was applied and the femoral rat bone with iron implant was scanned at high magnification and 80 kV protocol setting. The yellow arrows mark a clearly defined interface, which can be evaluated without huge dark areas around the implant.

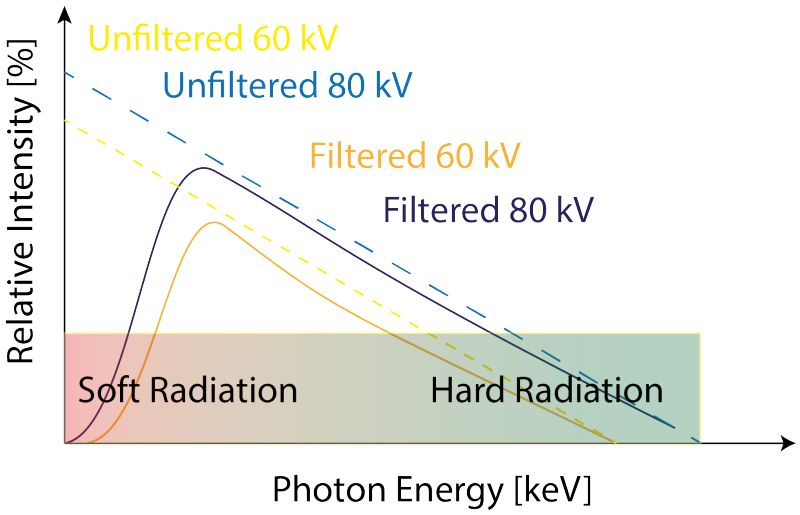

Figure 2.12: X-ray photon spectrum is composed out of low-energy and high energy photons. The low-energy part or soft radiation is known to be absorbed in tissue and may cause irritations and cancer. The high energy part or hard radiation will pass through the sample without absorption. The emission of soft radiation can be controlled using a filter setup at the outlet of the X-ray source, which will cut the highest intensity parts of low-energy photons at all available voltage settings.

the shaved leg. Muscles were mobilized carefully and kept from the implantation side with a spreader tool. A drill was made using a 1.5 or 1.55 mm drill and the implant was inserted by applying gentle pressure (press-fit). After correct bi-cortical placement, the wounds were closed in layers with bioresorbable suture Vicryl 4.0. The contralateral leg was operated in an identical procedure.

Anaesthesia was antagonized by a mixture of 4 parts Annexate (Roche, Austria, Vienna) and 0.5 parts Antisedane (Pfizer, Vienna, Austria). Injection was applied intraperitoneal with a dose of 0.1 ml per 100 g BW. Animals were monitored until full consciousness and provided with post-operative analgesia in drinking water (40 ml Dipidolor, Janssen-Cilag, Neuss, Germany dissolved in 5% glucose sirup per 500 ml water).

2.4 Aim 1: Radiological observation of PHB composite materials

Five different, pin shaped PHB composite materials (see fig. 2.1) were characterized radiologically for this aim. Special focus had to be put on the used scanning protocols to achieve a suitable contrast of those low-density materials. All materials (see tab. 2.1) were produced and shaped to pin implants by the Graz University of Technology, at the Institute for Chemistry and Technology of Materials.

2.4.1 Study design

72 male Sprague Dawley® rats were used during the study and implanted according to section 2.3. Longitudinal in vivo μCT with medium magnification setting were scheduled at 4W, 12W and 24W. Animals were sacrificed at timepoints 12W, 24W

Composite	PHB	Herafill®	ZrO_2
	weight %	weight %	weight %
P	100	0	0
P3Z	97	0	3
P30H	70	30	0
P3Z10H	87	10	3
P3Z30H	67	30	3

Table 2.1: PHB composite materials used within this aim [1].

and 36W and the femoral bones were harvested and deep frozen. High resolution μCT scans were performed with explanted samples to enable an improved contrast and more distinct quantification of degradation characteristics, volume and surface development and also bone incorporation of the material.

2.4.2 Adapted μCT observation in vivo and ex vivo

In vivo and ex vivo scans were conducted using different protocol settings according to table 2.2. The in vivo protocol enabled a longitudinal observation of the same animal during the whole study period of 36W. The used combination of voltage, current and low exposure time setting was developed to apply a minimum of radiation exposure to the animal, in order to avoid pathological impact in any way. However, the low exposure time and also the decreased rotation steps combined with only half rotation result in a decreased image quality and increased noise level. Due to the very low radiological density of polymeric implants, ex vivo scans were conducted using a lower acceleration voltage and a higher exposure time to achieve suitable contrast values. Beam filtration was not applied to enable the full spectrum of X-ray photons and reach higher contrast values. Rotation steps were increased to 270 with

Type	Mag	Voltage	Current	ET	RS	RD	Filter	Bin
		kV	μA	ms	#	°	mm	
In Vivo	medium	70	500	800	180	210	0.5	2
Ex Vivo	high	60	500	2000	270	360	-	2

Table 2.2: μCT protocol settings of magnification level (Mag), voltage and current, exposure time (ET), rotation steps (RS), rotation degrees (RD), filter setting and binning level (Bin) for in vivo and ex vivo scans of PHB implanted rat femoral bones.

a full rotation of 360 degrees.

2.4.3 Implants

Additionally to the adapted scanning protocols, radiologically hardly visible PHB composites were designed with addition of ZrO_2 which is known to act as a radiological contrast medium within methyl metacrylate (MMA) monomer bone cements [45] and is chemically inert and non-toxic [46]. ZrO_2 will ease the later quantification of the materials' characteristics (see table 2.1). The three composites P3Z, P3Z10H and P3Z30H were manufactured with the addition of 3 % ZrO_2, respectively. Herafill® (Heraeus, Wehrheim, Germany) was added to the composites to increase the materials' degradation rate. The special composition of Herafill as a composite of calcium sulfate ($CaSO_4$), calcium carbonate ($CaCO_3$) and glycerol tripalmitate is used as bone substitute material in clinics and was also proven to provide good osteoconductivity [47, 1].

2.4.4 Post processing of μCT data and quantifying the degradation and bone incorporation

Gathered μCT data was exported to DICOM format using Siemens Inveon Research Workplace ver. 1.2.2.2 and post-processed in Materialise MIMICS® ver. 15. Segmentation of bone tissue from implant material was done by setting implant threshold levels between -750 and +1000 Hounsfield units (HU). Manual corrections of resulting regions of interest (ROI) were applied, in order to compensate a possible temperature and environmental factors dependent drift of the detectors HU output. 3D rendered models allowed a numerical quantification of changes in implant volume and surface area. To evaluate the bone incorporation of the materials, a special method for a distinct measurement of the bone implant interface was conducted.

ROIs were defined in Materialise MIMICS® according to fig. 2.13. A cylindrical ROI, $\mathrm{TC}_{Implant}$ was set at the original implant dimensions in order to cover the segmented composite materials. Another ROI was used with an increased diameter by six-fold voxel size of the used magnification of 35.55 μm resulting in an absolute diameter of 2.02 mm. This decision was inspired by Liu et al. [48], where a correlation between ROI size and mechanical pull-out tests was shown. The actual amount of bone incorporation was calculated as bone-volume fraction $\frac{BV}{TV}$, according to equation 2.2. $\mathrm{BV}_{measured}$ equals the amount of bone tissue within the ring-shaped ROI after the subtraction of $\mathrm{TC}_{Implant}$ from TC_{ROI}, TV is the total size of this ring-shaped ROI. The sample image in fig. 2.14 shows the placement of corresponding ROI regions.

$$\frac{BV}{TV} = \frac{BV_{measured}}{((r_{TC_{ROI}})^2 \cdot \pi \cdot h_{TC_{ROI}}) - ((r_{TC_{Implant}})^2 \cdot \pi \cdot h_{TC_{ROI}})} \tag{2.2}$$

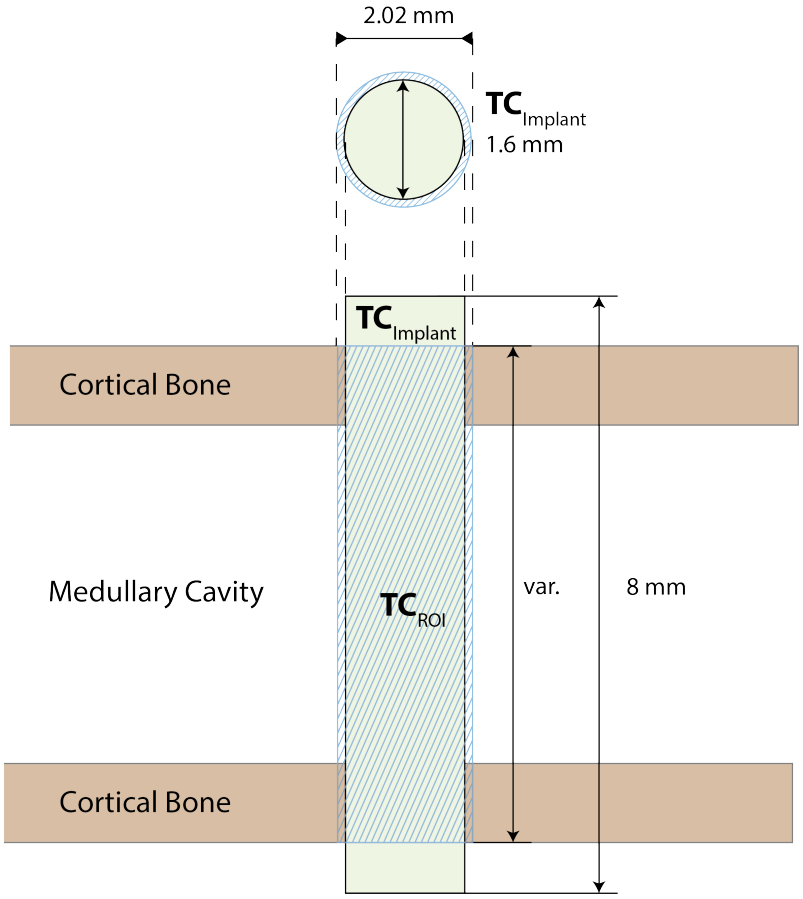

Figure 2.13: The bone incorporation on the implant site was quantified using two ROIs in Materialise MIMICS. Implant Tissue Cylinder ($TC_{Implant}$) was placed at the implant site with the dimensions of 1.6 mm diameter and 8 mm in length. TC_{ROI} was set to a diameter of 2.02 mm and a variable height, ending at the cortical periosteum.

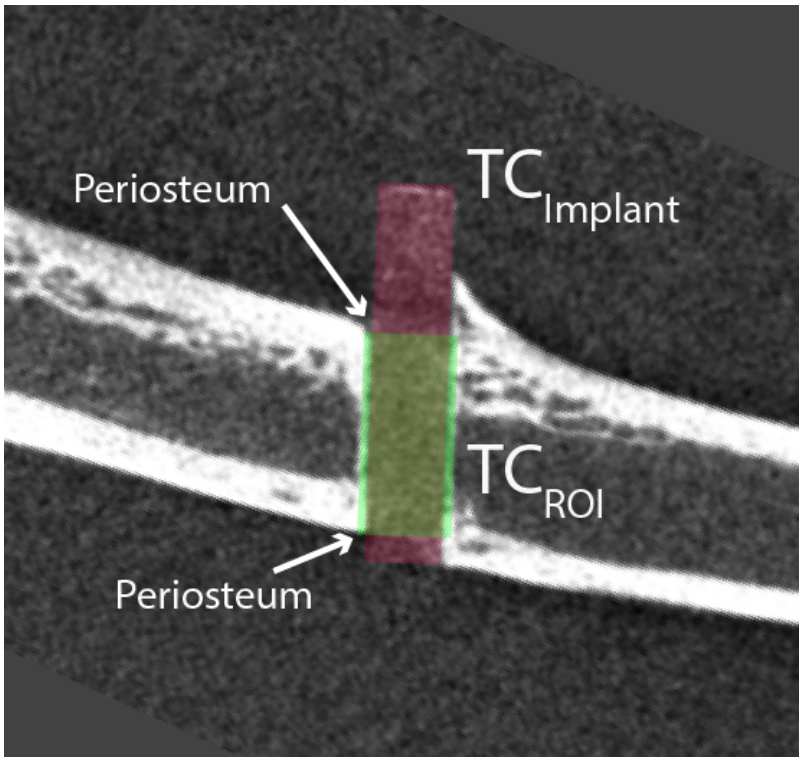

Figure 2.14: In the exemplary image, $TC_{Implant}$ was placed over the whole PHB composite implant. TC_{ROI} was placed ending at the cortical periosteum. The subtraction of the cylindrical ROIs results in a ring-shaped ROI for the quantification of bone ingrowth.

Alloy	Fe	Mn	C	Pd
	weight %	weight %	weight %	weight %
Fe pure	100	0	0	0
Fe-10Mn-1Pd	89	10	0	1
Fe-21Mn-0.7C-1Pd	77.3	21	0.7	1

Table 2.3: Fe alloys used for in vivo studies published in Kraus et al. [2]

.

2.5 Aim 2: Characterization of degradation behaviour of biodegradable iron (Fe) alloys under assessment of μCT based volume and surface data in vivo

Three different Fe alloys were used within this study and implanted into femoral bones of male Sprague Dawley® rats. Longitudinal μCT scans were performed in vivo over a study period of 52 weeks. Implant volume and surface development was examined by data post processing and also ex vivo high resolution scans were made after explantation of the tibiae at 4 weeks and 52 weeks.

2.5.1 Implants

Cylindrical pins with a diameter of 1.6 mm and 8 mm in length were manufactured from the alloys listed in table 2.3, see also fig. 2.1 c). All alloys were heat-treated to achieve an artificial ageing process [2] and were tested by in vitro experiments in

[17, 49]. The manufacturing process was performed with clean tools and the cleaning was done in pure ethanol followed by gamma sterilization with a dose of 25 kGy (Mediscan GmbH, Seibersdorf, Austria).

2.5.2 Study design

Thirty-eight male Sprague Dawley® rats were used within this study over a period of 52 weeks. Surgical implantation procedure was performed according to Kraus et al [2] and is described in section 2.3. Animals were sacrificed at 4, 12, 24 and 52 weeks and femoral bones were harvested. All samples were freed from residual soft tissue and deep frozen at -80 °C.

2.5.3 Macroscopic photography of explanted bone-pin samples

Detailed photographs of explanted rat femora with iron alloy pins were created at the Department of Cell Biology, Histology and Embryology at the Medical University of Graz, in order ensure a distinct macroscopic view on the implant surface condition. Timepoints for macroscopic images were 4, 12, 24 and 52 weeks.

2.5.4 In vivo and ex vivo μCT scans

In vivo micro CT scans were performed using the standard in vivo imaging protocol for rats as displayed in table 2.4. Filtration setting was kept at a minimum level of 0.5 mm at this stage of the study, to avoid any loss in contrast. The ex vivo imaging protocol was set to the maximum voltage in combination with maximum filtration

Type	Mag	Voltage	Current	ET	RS	RD	Filter	Bin
		kV	μA	ms	#	°	mm	
In Vivo	medium	70	500	800	180	210	0.5	2
Ex Vivo	high	80	500	2000	270	360	1.5	2

Table 2.4: μCT protocol settings of magnification level (Mag), voltage and current, exposure time (ET), rotation steps (RS), rotation degrees (RD), filter setting and binning level (Bin) for in vivo and ex vivo scans of Fe alloys implanted in rat femoral bones.

of 1.5 mm, to reduce beam hardening artifacts by dense, metallic implants (see also section 1.2.6).

2.5.5 Implants

2.5.6 Post processing of μCT data

Gathered μCT data was evaluated regarding volume and surface alterations by creating ROIs and setting threshold levels for the implant materials between 3256 and 8064 HU [2]. For this purpose, the software Siemens Inveon Research Workplace ver. 3.0 could be used, because of the very high contrast differences between cortical bone and the different iron alloys.

2.6 Aim 3: Fluorescence Molecular Tomography (FMT) in transcortical rat model with osteoclast and osteoblast activity labelling fluorescent imaging agents in combination with micro CT imaging

FMT based quantification of osteoblast and osteoclast activity in growing Sprague Dawley® rats was performed with the two alloys BRI.Mag® and Mg10Gd. The experimental groups for the FMT study were composed of the following animals:

- BR: Transcortical implantation of BRI.Mag® Pins (3 animals, n=6 femoral bone samples)
- GD: Transcortical implantation of Mg10Gd Pins (n=6)
- KM: Untreated control (n=2)
- SM: Sham animals with transcortical drill (n=2)

2.6.1 Implants

6 pins made of the alloy BRI.Mag® and 6 pins made of Mg10Gd were implanted into femoral rat bones. The implantation of those 8 mm long pins with 1.6 mm diameter (see fig. 2.1 b)) was performed according to the transcortical implantation model, described in section 2.3.

2.6.2 Fluorescence Molecular Tomography (FMT) Imaging

For FMT examination, the demo device Perkin Elmer FMT 2500 was provided directly by the manufacturer over a timespan of 4 months. The FMT 2500 system contains four different lasers for the simultaneous excitation of fluorescent probes with the wavelengths 635 nm, 680 nm, 750 nm and 790 nm. At these wavelengths, light is known to travel through soft tissue and even bone tissue with very low absorbance. The FMT system is capable to create quantitative fluorescence images of the scanned animal and includes, besides the 2D fluorescent information known from systems like Maestro® (former CRI, now Perkin Elmer), also a Z-axis for three dimensional quantification of the signal. In contrary to the Maestro® System, images are not created by taking one single picture. The laser beam is constantly moving to defined points across the animal and the resulting fluorescent signals are reconstructed to the final 3D fluorescence image. The FMT field of view is limited to 8 cm x 8 cm which is observed by 12.3 mm x 12.3 mm CCD with 512 x 512 pixels. The resulting pixel size is 24 x 24 microns. Combining the optical integrity and reconstruction performance with multiple source/detector projections delivers a spatial resolution in the sub-millimeter region.

FMT and micro CT observations were scheduled at 2W, 4W, 6W, 8W and 12W after implantation.

2.6.3 Injection of fluerescent tracer probes

Two different fluorescent probes were used in this study: Perkinelmer Osteosense 750 EX, which is based on a bisphosphonate carrier for the fluorescent dye. This bisphosphonate binds to newly created hydroxyapatite during its circulation in the bloodstream and therefore labels the amount of new bone constructed by osteoblasts

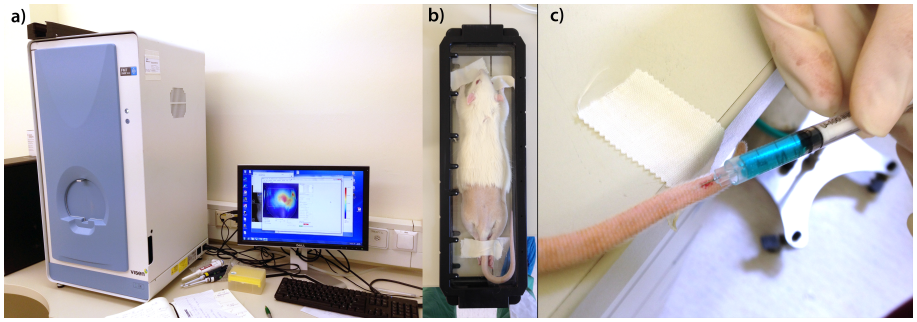

Figure 2.15: The scanning setup of the Perkin Elmer FMT 2500 device is shown in a). The imaging device has a chamber where the imaging cassette (rat cassette) in b) will be placed. c) shows the injection of a flueorescent tracer liquid via the rat's tail vein.

with a fluorescent tracer. Bisphosphonates are clinically used to inhibit bone resorption in osteoporosis treatment [50]. The applied dosage within this study is very small compared to a clinical treatment and an effect on bone remodelling is not expected. Perkinelmer Cathepsin K 680 Fast is based on the cathepsin K protease, which is found in osteoclasts. The fluorescent dye is activated by cleavage by the cathepsine K protease produced during osteoclast activity [51, 52].

The tail vein injection of Osteosense 750EX was done 24 h before the actual FMT scan to ensure the complete incorporation of the fluorescent tracer into new bone structures. The injection dose was calculated regarding the animals' bodyweights and the recommended dose for mice in the Perkin Elmers Datasheet was adapted to the used rat model. One vial of Osteosense 750EX was diluted with 1.2 ml sterile PBS which resulted in an injection dose of 0.048 nmol/g BW and an injection volume of 0.025 ml/nmol.

The second tracer Cathepsine K 680 Fast was used at a concentration 0.05 nmol/g BW and was injected 6 h before starting the imaging process via intraperitoneal injection, following the Perkin Elmer application protocol. For every FMT scan

Type	Mag	Voltage	Current	ET	RS	RD	Filter	Bin
		kV	μA	ms	#	°	mm	
μCT In Vivo	low	70	500	1200	360	360	0.5	2

Table 2.5: μCT and protocol settings of magnification level (Mag), voltage and current, exposure time (ET), rotation steps (RS), rotation degrees (RD), filter setting and binning level (Bin) for in vivo scans of the FMT imaging cassette with the fixated rat.

procedure, the Rat was anaesthetized and fixated inside a specific rat cassette. This cassette also contains optical markers, which are visible one the produced FMT or micro CT image and are important for co-registration of both imaging methods.

2.6.4 In vivo μCT imaging of the animal within the FMT cassette

Directly after the FMT analysis, the whole cassette with the animal inside was scanned in Siemens Inveon μCT without changing the position. To achieve the maximum field of view (FOV) of 5.3 cm x 7.9 cm, the CT protocol was set to low magnification resulting in a resolution of 51.75 μm per voxel at binning setting 2 (see also table 2.5). Due to the reason, the animal was scanned under general anaesthesia and fixed in the imaging cassette, the bore tunnel for in vivo scans was not used in this procedure.

2.6.5 Data post processing and multimodal co-registration of μCT and FMT imaging

Generated FMT data was observed and quantified regarding fluorescent intensity and location in Perkin Elmer TrueQuant. ROIs were defined at the femoral regions of the rats and fluorescence intensity was normalized and compared between all groups. Gathered micro CT data was exported to DICOM format and processed in Materialise MIMICS ver. 17. To enable a co-registration with FMT, rats were scanned inside with the FMT imaging cassette, which contains CT traceable markers (see 2.15 b)). Co-registration and data merging of fluorescence and micro CT imaging results was performed in Perkin Elmer TrueQuant and imageJ.

2.7 Aim 4: Micro CT supported biomechanical evaluation of ESIN interlocking systems in cadaveric sheep tibiae

The following study was conducted ex vivo, in order to evaluate the mechanical behaviour of different interlocking plug-screw systems without the influence of bone healing.

2.7.1 Study design

For this ex-vivo study, 38 cadaveric lamb tibiae (12-16 weeks of age) were used. Implantation of 3 mm Titanium ESIN nails was performed at the Vienna Technical University according to clinical standards. Five different interlocking systems were

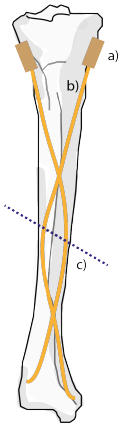

Figure 2.16: At point c), a ring-shaped piece of bone were cut and removed, in order to create a gap, which is closed by applying pressure on the ends. 3 mm Ti ESIN implants b) were used to stabilize the fracture and locked with different plug systems a) and interlocking screws.

examined within this study to achieve a sample size of n=7-9 per group. For a suitable test setup, the bones were cut in the middle of the diaphysis and the distal part was removed (see fig. 2.16)). Mechanical loading was applied (Vienna Technical University) on the protruding distal ends of the ESIN implants. Biomechanical testing was examined until system failure. Afterwards all samples were observed in medium resolution micro CT to analyse and quantify occurring failure modes. To allow a distinct insight into the internal bone damage and a further comparison regarding different interlocking systems, μCT scans were performed.

2.7.2 Interlocking systems

The following interlocking systems were compared regarding their mechanical behaviour within this study:

- Ender nail: ESIN nail with a flattened end and an oval "eye" for screw mounting. Contrary to all other described interlocking systems, this nail has to be cut to the right length before insertion into the medullary cavity.

- Plug 3.5 mm: Standard Ti ESIN rods with a diameter of 3 mm can be locked using this system after cutting protruding ends of the nail. Interlocking screw dimensions are 3.5 mm diameter and 26 mm length.

- Fixplug: Besides the interlocking screw with the same dimensions as for the Fixplug system, it consists of another fixation screw to additionally lock the nail inside the plug.

- Plug 3 mm: This system uses smaller plugs and also a lower diameter of interlocking screws with 3 mm.

- TwinPlug: The Twinplug system uses two similar interlocking screws with 3.5 mm diameter and 26 mm length.

2.7.3 Ex vivo μCT scans

Samples were scanned using a micro CT protocol with 70 kV and 500 mA. Exposure time was set to 2200 ms, using a 270° rotation with 180 steps. Magnification was set to medium, resulting in a resolution of 35.55 μm per voxel. Beam hardening artifacts were reduced applying a 1.5 mm aluminium filter to remove soft radiation. Images were reconstructed, exported to DICOM format and analysed in Materialise MIMICS® ver. 17.

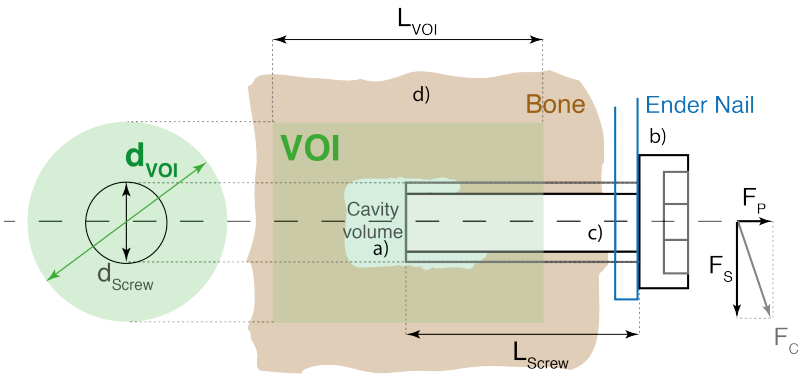

Figure 2.17: This scheme shows the used quantification method for the assessment of internal bone damage after mechanical loading of the screw-plug system or ender nail b). The volume of interest (VOI) was placed at the lower half of the screw with a length according to the screw c) thread length. Damage was quantified by calculating the volume of the risen cavity a) inside the bone d) by screw displacement.

2.7.4 Post processing of μCT data

An innovative evaluation method was developed to quantify internal bone damage after screw migration caused by acting forces. The VOI cylinder was placed at the second half of the measured screw's length, see fig. 2.17. The threshold of an air filled cavity was defined as common air threshold between -1024 and -1000 HU. The cavity volume (CV) inside the VOI was used to quantify the internal bone damage caused by the screw migration during mechanical loading. A displacement ratio was computed using the cavity volume (CV) and total volume of VOI (TV) fraction (see fig. 2.17) in equation 2.3.

$$R_{Disp} = \frac{CV}{TV} \tag{2.3}$$

2.8 Aim 5: Clinical CT imaging of degradable Magnesium ESIN Implants in the growing sheep model

ESIN nails with 3 mm (BR3) and 4.5 mm (BR45) in diameter were manufactured of the material BRI.Mag® by extrusion. The material ZX10 was used for 3 mm ESIN and a commonly used Titanium version was implanted for control purposes. Chemical surface polishing was performed on BR3, BR45 and ZX10 implants, resulting in the abbreviation BR3-pol, BR45-pol and ZX10-pol.

2.8.1 Study design

30 lambs (Tiroler Bergschaf) were used within this large animal study and divided into the following groups:

- G1: degradation behaviour of BR3 (two 3 mm implants), no fracture (n=3)
- G2: degradation behaviour of ZX10 (two 3 mm implants), no fracture (n=2)
- G3: untreated control group, CTRL (n=3)
- G4: transcortical implantation in epiphysis, diaphysis, distal metaphysis of BR3 (cut to the right length), degradation, simulation of a screw, no fracture (n=2)
- G5: transcortical implantation of conventional Titanium in epiphysis, diaphysis and distal metaphysis, control (cut to the right length), (n=1)

- G6: degradation behaviour of polished BR3-pol (two implants) and ZX10-pol (two implants), (n=2)
- G7: degradation behaviour of polished BR45-pol and unpolished BR45 (1 implant), no fracture (n=2)
- G8: fracture model, 90° fracture at middle diaphysis, BR3 implants (2 implants), fixateur externe for 6 weeks (n=1)
- G9: fracture model, 30° oblique fracture at middle diaphysis, BR45-pol implants (1 implant), cast only, (n=7)
- G10: fracture model, 30° oblique fracture at middle diaphysis, BR45-pol implants (1 implant), fixateur externe, (n=6)

All animals were prepared for the surgical operation by sterile covering. For ESIN implantation, two incisions were made lateral and medial of the tibial tuberosity. The medullar cavity was opened with a pricker in an angle of 30°. For fracture models in G8-10, another incision was made at the mid-diaphyseal region of the tibia. The inserted ESIN was removed again and the osteotomy was performed using an oscillating saw. The tibial cortex was cut, performing an oblique fracture with 30° in G9 and G10, or an horizontal fracture with 90° for G8. After this procedure, the fracture was stabilized, using two 3 mm Mg nails or one single 4.5 mm nail. After cutting the implants to the right length and radiological control (image converter), the wound was closed in layers and a cast was applied to the animals' leg. For the external fixation group in G8 and G10, an additional fixation device (Orthofix, LRS) was applied by drilling of four bicortical holes from the lateral side. Four long fixation pins were screwed into the bone and a stabilization rail was mounted on the screws, in order to stabilize the fracture. Distinct fracture reduction can be applied by fine-tuning the rail fixation screws.

Implantation types of study groups G1, G2 with unpolished 3 mm BR3 and ZX10 material and G6 with polished BR3 and ZX10 is shown in fig. 2.18 I), where a) describes the channel of the 3 mm Mg implant. Untreated control group G3 was drawn in II), as well as the transcortical groups G4 and G5 in III). Transcortical implants were inserted into the proximal epiphyseal area a), middle diaphysis b) and distal epiphysis/metaphysis c). IV) and V) show groups G7 without fracture and G9 with oblique fracture b) and 4.5 mm BRI.Mag® material a). The groups G8 and G10 with fixateur externe supported osteosynthesis until week 6 post operationem is shown in fig. 2.19, I) and II). Osteosynthesis with fixateur externe is the second most used method for the treatment of paediatric fractures. Complex and unstable fractures are the most common indication for external fixation. The method itself is usually well tolerated and the device can be removed after recognizable callus formation [53, 54].

2.8.2 Clinical CT scan

All study groups were scheduled for clinical CT scans at defined time points in fig. 2.20. CT scans were performed at the Department of Radiology at the Medical University of Graz, using a Siemens Sensation Cardiac 64 CT device. The examination protocol for the sheep study was developed with a spatial resolution of 0.6 mm per voxel with 0.6 mm pitch. The operating voltage was set to 120 kV and 35 mA, which results in a combined dose of 13.42 mGy at a scanning time of 44.63 s. This dose is around 90 % higher compared to clinical every day use and was chosen to achieve a very detailed scan suitable to judge implants degradation and tissue reaction in the surrounding. Four different views were measured or reconstructed:

- Axial, bone window, 70f, very sharp, FOV 153 mm x 153 mm, 525 images
- Coronal, bone window, 70f, very sharp, FOV 121 mm x 281 mm, 101 images

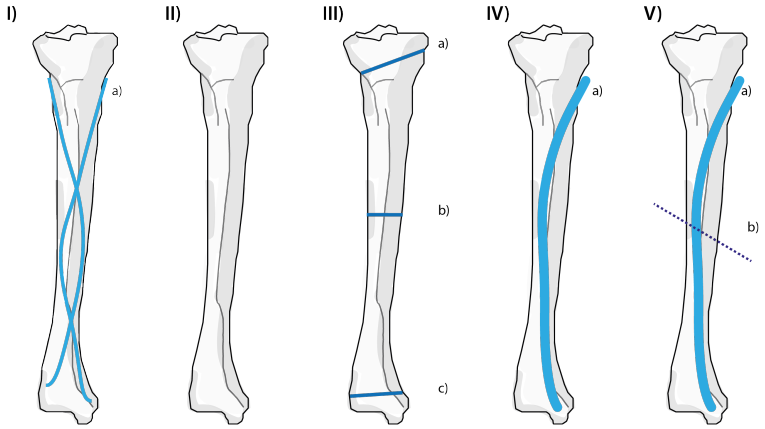

Figure 2.18: Study groups used within the biodegradable ESIN sheep study. Two 3 mm Mg ESIN rods were used according to Ti gold-standard in I). II) shows an untreated control bone. Transcortical implantation of cut 3 mm Mg ESIN rods was performed in III), IV) shows the implantation of 4.5 mm BRI.Mag material without fracture. A 30° oblique fracture was performed in V) and stabilized by 4.5 mm BRI.Mag ESIN.

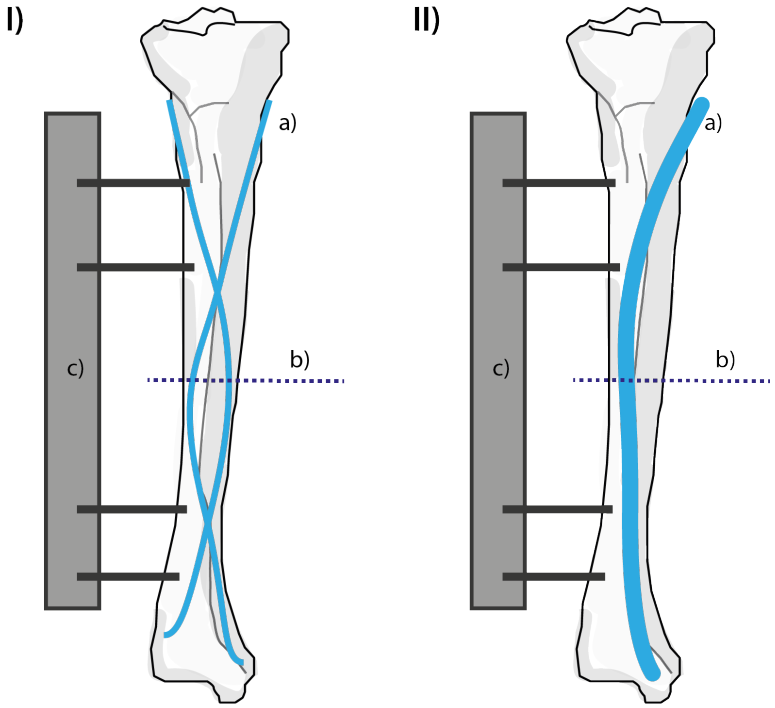

Figure 2.19: Osteosynthesis of a 90° fracture was performed with 3 mm BRI.Mag ESIN in I) and with 4.5 mm BRI.Mag ESIN in II). Both are supported by an external fixation device until week 6 post op.

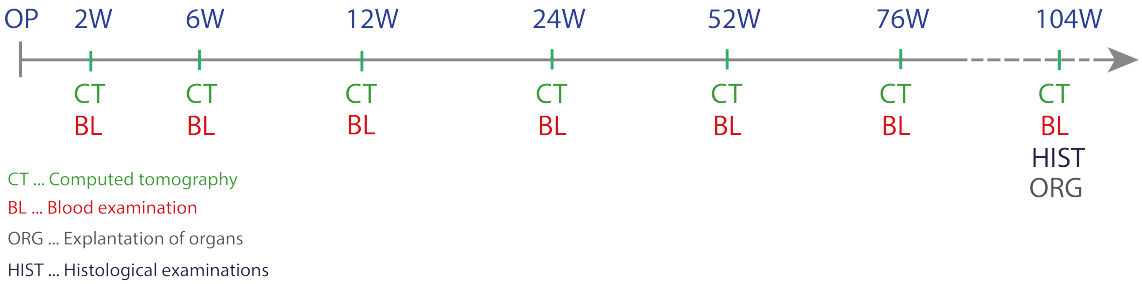

Figure 2.20: Time points for clinical CT imaging and blood sampling were scheduled closely in the first 6 months of the study. A long term observation was planned over a period of two years. Blood sampling was performed at each CT time point. Organ sampling and histological evaluation will be performed at the end of the study.

- Sagittal, bone window, 70f, very sharp, FOV 121 mm x 280 mm, 107 images
- 3D reconstruction

2.8.3 Post processing of clinical CT imaging data

Clinical CT data was directly exported in DICOM format and no additional conversion was applied. To achieve the maximum image information, the axial bone window with 525 images (see section 2.8.2) was opened in Materialise MIMICS® ver. 18. Implant materials were segmented by applying Region Growing, Lasso and Boolean operations after setting a suitable threshold for gas cavities from -1024 to -547 HU and Mg materials from 500 to 2300 HU. 3D models were calculated from segmented ROIs and volume, surface and hydrogen gas cavities in the implant surrounding were measured.

2.9 Aim 6: Micro CT ex vivo characterization of BRI.Mag® screws in ovine metaphyseal, epiphyseal and diaphyseal tibia

For the next stage in implant development, the Mg alloy BRI.Mag® was used to produce screws for the surgical fixation of non load bearing fractures, common in human patients for example at the inner ankle.

2.9.1 Implants

The first generation of biodegradable screws were designed with a diameter of 3.5 mm and a length of 16 mm (see fig. 2.6 a)). The screws were dry machined to avoid contaminations by cooling liquids. Screws for experimental group G1 (n=6) were left untreated while screws for group G2 (n=6) were chemically polished at the ETH Zurich. All implants were packed separately into peel bags (Biegler GmbH, Mauerbach, Austria) and gamma sterilized with a dose of 25 kGy (Mediscan, Seibersdorf, Austria).

2.9.2 Study design

Two female lambs were used for this feasibility study and divided into the two experimental groups G1 and G2. The surgical operation was performed under general anaesthesia and sterile clinical conditions. The complete operation procedure is shown in fig. 2.21. Two small incisions were made medial and lateral from the tibial tuberosity. After pre-drilling with a 3.5 mm drill, tapping of a thread was performed using a standard self-cutting 3.5 mm titanium screw. Tapping site was rinsed

with physiological saline solution to remove tapping residuals from the thread. Two BRI.Screws were inserted, leaving a 1 mm gap between the screw head and bone, which was necessary to perform pull-out tests after 6 weeks.

Four more incisions were made on the medial side of the diaphysis and a similar procedure for insertion was conducted, resulting in the following screw positions in the bone, also shown in the scheme in fig. 2.22.

- G1.1 Proximal epi-/metaphysis, medial
- G1.2 Proximal epi-/metaphysis, lateral
- G1.3 Proximal diaphysis 1
- G1.4 Proximal diaphysis 2
- G1.5 Distal diaphysis 2
- G1.6 Distal diaphysis 1

Group G2 with polished BRI.Screw was performed almost similar, except the most distal screw was inserted into the distal epiphysis.

- G2.1 Proximal trabecular bone, medial
- G2.2 Proximal trabecular bone, lateral
- G2.3 Proximal diaphysis 1
- G2.4 Proximal diaphysis 2
- G2.5 Distal diaphysis
- G2.6 Distal epi-/metaphysis

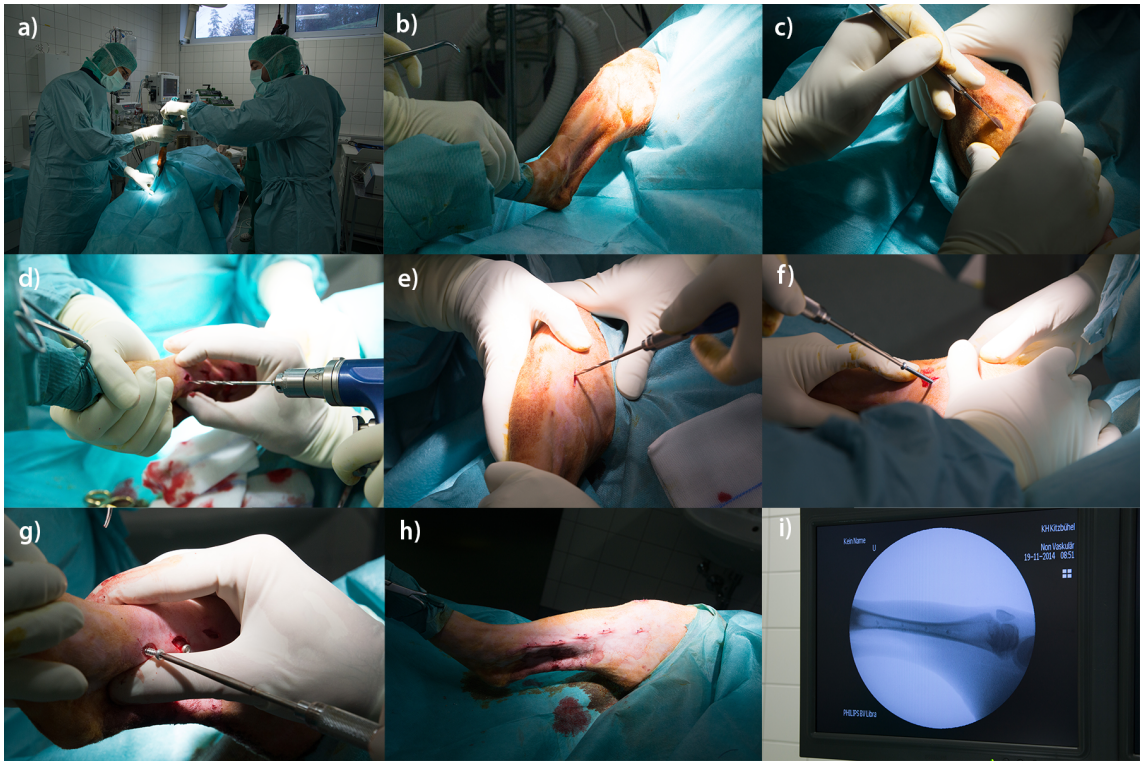

Figure 2.21: The surgical implantation of BRI.Mag screws (diameter 3.5 mm and 16 mm length) was performed under sterile clinical conditions in the large animal operation theater of the Department of Biomedical Research, Medical Universtiy of Graz. The right leg was shaved b) and small incisions were made in c). A machine drill was made at the diaphyseal region in d), the epiphsyseal/metaphyseal location was drilled manually in e). Pre-tapping of the screw thread was applied by a self-cutting Ti screw with the same diameter. Mg screws were inserted in g) and the wounds were closed using Prolene 2.0 and Vicryl 4.0 sutures in h). Radiographs were taken using an X-ray image converter intra-operatively and after the surgical intervention in i).

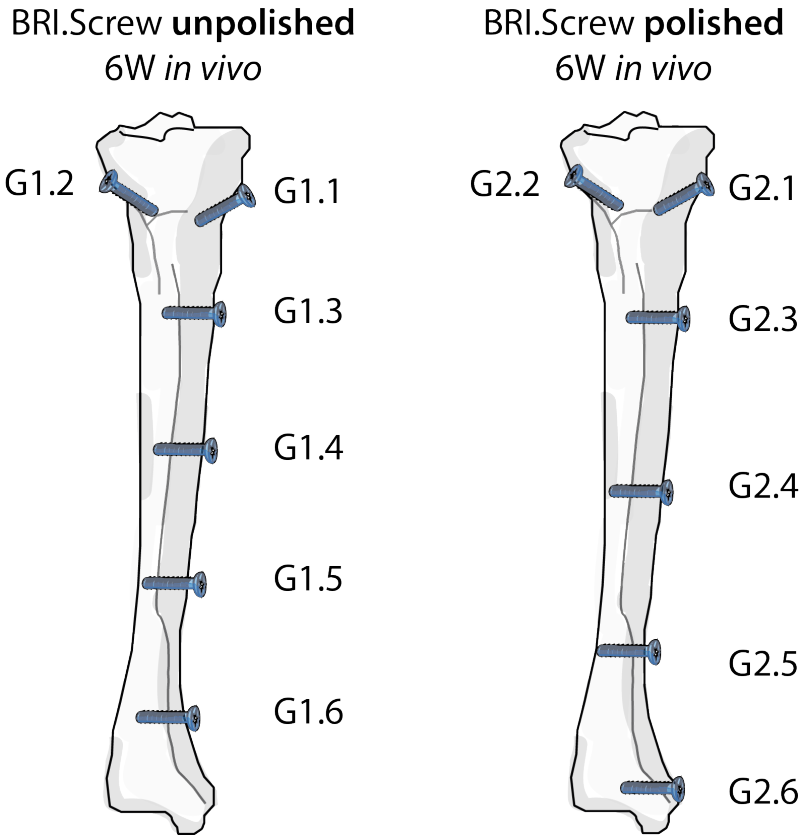

Figure 2.22: Unpolished BRI.Screws were implanted in proximal epi-/metaphysis (G1.1 and G1.2), proximal diaphysis (G1.3 and G1.4) and distal diaphysis (G1.5 and G1.6). The polished 16 mm BRI.Screw was implanted almost similar. The most distal screw G2.6 was inserted into the distal epi-/metaphysis.

Type	Mag	Voltage	Current	ET	RS	RD	Filter	Bin
		kV	μA	ms	#	°	mm	
μCT Ex Vivo	low	50	500	1200	720	360	0.5	2

Table 2.6: μCT and protocol settings of magnification level (Mag), voltage and current, exposure time (ET), rotation steps (RS), rotation degrees (RD), filter setting and binning level (Bin) for ex vivo scans BRI.Screws in polished and unpolished version. A 5x multibed setting was applied to enhance the axial field of view to the full bone length.

2.9.3 Clinical CT and μCT imaging

Both animals were scanned in clinical CT after 2W and 6W post op. The scanning parameters were set according to section 2.8.2. After 6W, the animals were sacrificed and both tibiae were harvested, wrapped into saline soaked gauze and deep frozen at -20°. A low magnification (51.75 μm voxel size with binning setting 2) micro CT scan was performed with the explanted tibiae to determine the bone implant interface quality, screw degradation and gas production with a distinctly higher accuracy than with in vivo human CT. A protocol for explanted sheep tibiae was created using low magnification to extend the transaxial field of view to the maximum value of 5.3 cm. The axial field of view was extended from 7.9 cm to 33.18 cm by using the 5x multibed setting with 10% overlapping. Further scanning parameters were set according to table 2.6. After micro CT observations, the implanted right tibiae and the untreated left tibiae were sent to Vienna Technical University for biomechanical pull- out testing. The untreated tibiae were implanted with similar screws and used as control samples without degradation.

2.9.4 Post processing of imaging data

Gathered μCT data was converted to DICOM format using Siemens Inveon Research Workplace v.2.2.2. Clinical CT data was also delivered in DICOM format, no further conversion was necessary. Post processing was done using Materialise MIMICS® ver. 18. Volume loss, surface area and size of gas cavities was evaluated by applying threshold values for gas cavities from -1024 to -547 HU and Mg materials from 500 to 2300 HU.

2.10 Ethical approval for small and large animal experiments

All animal experiments were conducted under animal ethical respect and were authorised by the Austrian Ministry of Science and Research with the following accreditation numbers:

- BMWFW-66.010/0110-WF/II/3b/2015
- BMWFW-66.010/0190-WF/II/3b/2014
- BMWFW-66.010/0049-WF/II/3b/2014
- BMWFW-66.010/0073-WF/II/3b/2015
- BMWFW-66.010/0067-WF/II/3b/2012
- BMWFW-66.010/0122-WF/II/3b/2014
- BMWFW-66.010/0017-WF/II/3b/2014

The ethical approvals are attached to the "*Appendices*" section.

Small animal housing was done with four animals per cage and the possibility to straighten up to full body height and care was provided by professional animal caretaking staff and veterinarians, according to FELASA guidelines in Guillen et al. [55].

Large animals were housed in small groups of four at the Department of Biomedical Research at the Medical University of Graz. All animals hat free access to lawn and meadow with water ad libitum.

2.11 Euthanasia

For euthanasia of small animals, volatile isoflurane (Forane®, Abbot AG, Baar, Switzerland) was used for anaesthesia, followed by injection of 25 mg sodium thiopental (Thiopental® Sandoz, Sandoz GmbH, Kundl, Austria) directly into the cardiac ventricle. Immediately after cardiac arrest, femoral bones, organs and soft tissues were harvested and deep frozen at -80°C. Large animals were euthanized by application of sodium thiopental (Thiopental® Sandoz, Sandoz GmbH, Kundl, Austria) and T91, strictly intravenously to avoid irritation of any soft tissue. Tibiae were harvested, wrapped into saline soaked gauze and deep frozen at -20 °C.

3 Results

All surgical interventions conducted during small animal studies were well tolerated and no adverse effects were noticed. Slight reddening appeared post operatively in some animals and decayed already after a few days. Food and water intake was normal and animals did not show any signs of pain like tousled or bent position in the housing.

3.1 Aim 1: Radiological observation of PHB composite materials

The characterization of PHB composites regarding implant volume and implant surface development was performed by high-resolution ex-vivo μCT, in order to ensure a suitable imaging contrast for a distinct measurement. Conducted longitudinal μCT scans could only show minor changes in surface and volume over the whole study period. The numerical results are shown in tables 3.2 for 12W, 3.3 for 24W and 3.4 36W. Implant volume and implant surface were also described graphically in fig. 3.1 and fig. 3.2.

No clear differences in degradation by measurement of volume loss and surface alteration can be shown for the observed materials at all time points in fig. 3.1 and

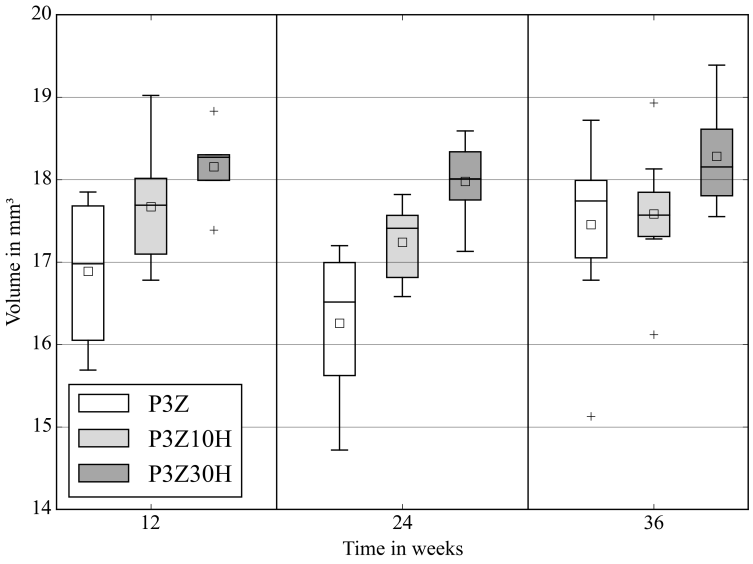

Figure 3.1: Development of PHB implant volume was quantified for P3Z, P3Z10H and P3Z30H, using in vivo μCT scans. A slight increase of implant volumes was noticed between week 24 and week 36. Results were published in Meischel, Eichler et al. in [1].

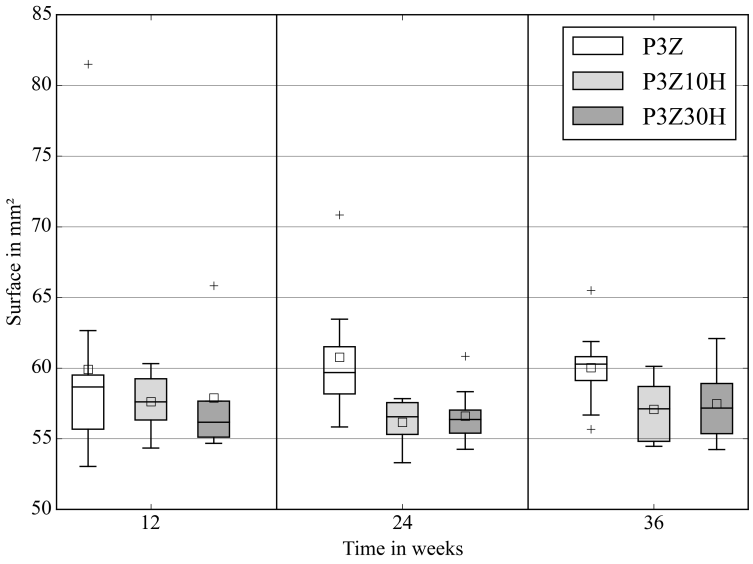

Figure 3.2: PHB implant surface was measured for P3Z, P3Z10H and P3Z30H for the time points of 12, 24 and 36 weeks post op. No significant alteration was measurable by in vivo μCT observation. Results were published in Meischel, Eichler et al. in [1].

Composite	VG 12W	SG 12W	VG 24W	SG 24W	VG 36W	SG 36W
	%	%	%	%	%	%
P3Z	4.9	35.5	1.0	37.4	8.5	35.72
P3Z10H	9.8	30.3	7.1	26.9	9.3	29.1
P3Z30H	12.9	30.9	13.6	28.0	13.6	29.9

Table 3.1: Measured percentage of volume gain (VG) and surface gain (SG) after 12W, 24W and 36W. Published in Meischel, Eichler et al in [1].

3.2. All composites showed an increase in volume and surface above the calculated values in tables 3.2, 3.3 and 3.4, which is known in literature as swelling of polymers like PLGA in [56] and was described as volume gain (VG) and surface gain (SG) in table 3.1.

Bone incorporation of PHB composite materials was compared using longitudinal in vivo μCT scans. After quantification of new bone volume in the close surrounding of the implant, as described in post processing procedure in fig. 2.14 and fig. 2.13. P3Z, P3Z30H and P3Z10H achieved a decreasing value for $\frac{BV}{TV}$, shown in fig. 3.3. The composite with the highest amount of Herafill® of 30 % and additionally 3 % of ZrO_2, P3Z30H exhibited the highest bone incorporation at week 24, almost equal to the Mg alloy WZ21. After the period of 36 weeks, both materials with Herafill® and ZrO_2, P3Z10H and P3Z30H were showing the highest bone incorporation values.

Pictures of in vivo μCT scans were shown in 3.4. Clear callus formation was noticeable after week 4 for all materials. The higher bone incorporation, which was also measured in fig. 3.3, is clearly noticeable for P3Z30H after 12W and 24W. The low radiological contrast of pure PHB was displayed in fig. 3.5 d) and compared to P3Z a), P3Z10H b) and P3Z30H c), where P is hardly visible in comparison to ZrO_2 and Herafill® enriched materials.

12W		Volume mm^3				Surface mm^2		
Composite	M	R		SD	M	R		SD
Calculated	16.09	-		-	44.23	-		-
P3Z	16.89	15.69	-	0.877	59.91	53.04	-	8.866
		17.79				81.51		
P3Z10H	17.67	16.78	-	0.775	57.63	54.34	-	2.204
		19.02				60.31		
P3Z30H	18.16	17.39	-	0.524	57.89	54.67	-	4.586
		18.83				65.83		

Table 3.2: Measured implant volume and surface with mean values (M), measurement range (R) and standard deviation (SD) after 12 weeks in vivo. Original implant volume and surface were calculated from a cylindric shape of 1.6 mm in diameter and a hight of 8 mm. Published in Meischel, Eichler et al in [1].

24W		Volume mm^3				Surface mm^2		
Composite	M	R		SD	M	R		SD
P3Z	16.26	14.72	-	0.914	60.76	55.83	-	4.689
		17.20				63.46		
P3Z10H	17.24	16.58	-	0.517	56.17	53.31	-	1.755
		17.82				57.84		
P3Z30H	17.98	17.13	-	0.490	56.62	54.26	-	2.134
		18.59				60.84		

Table 3.3: Measured implant volume and surface with mean values (M), measurement range (R) and standard deviation (SD) after 24 weeks in vivo. Published in Meischel, Eichler et al in [1].

36W		Volume mm^3				Surface mm^2		
Composite	M	R		SD	M	R		SD
P3Z	17.46	15.13	-	1.073	60.03	55.67	-	2.860
		18.72				65.50		
P3Z10H	17.58	16.12	-	0.700	57.09	54.46	-	2.290
		18.93				60.12		
P3Z30H	18.28	17.55	-	0.681	57.49	54.23	-	2.927
		19.39				62.09		

Table 3.4: Calculated and measured implant volume and surface with mean values (M), measurement range (R) and standard deviation (SD) after 36 weeks in vivo. Published in Meischel, Eichler et al in [1].

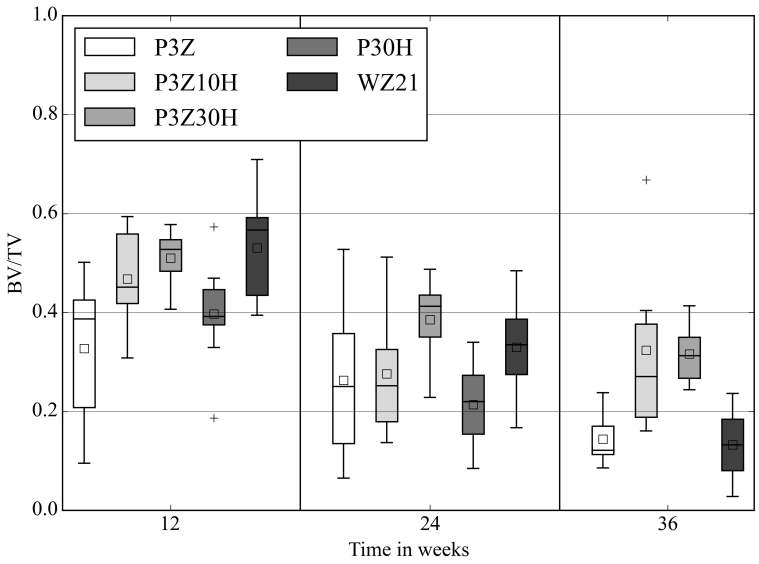

Figure 3.3: Bone incorporation on the materials' surface plays a major role for mechanical stability of an osteosynthesis material and was determined by calculating the bone volume fraction $\frac{BV}{TV}$ for P3Z, P3Z10H, P3Z30H and P30H. Also the slow degrading Mg material WZ21 was taken into account for comparison. This figure was published in Meischel, Eichler et al in [1].

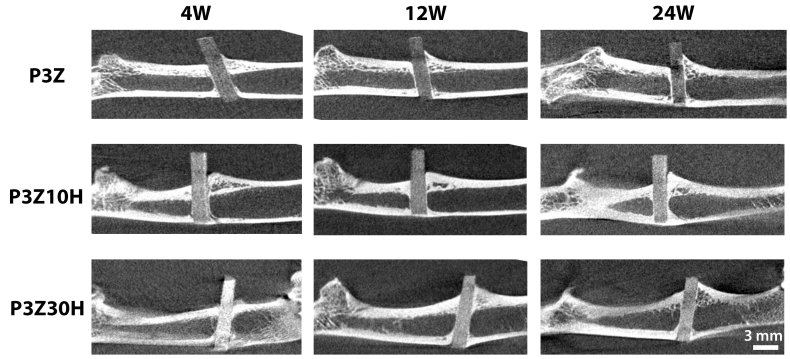

Figure 3.4: Micro CT in vivo scans were created after 4, 12 and 24 weeks in vivo. Due to visibility reasons, only composites containing ZrO_2 are shown [1].

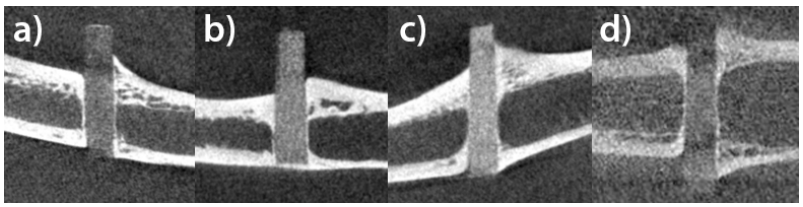

Figure 3.5: All PHB composites were scanned in vivo in μCT. A comparison of radiological contrast was made between the material P3Z in a), P3Z10H in b), P3Z30H in c) and pure PHB (P) in c). All images were created after 12W in vivo.

3.2 Aim 2: Characterization of degradation behaviour of biodegradable iron (Fe) alloys under assessment of μCT based volume and surface data in vivo

The in vivo degradation behaviour of the alloys pure Fe, Fe-10Mn-1Pd and Fe-21Mn-0.7C-1Pd were assessed using high resolution μCT scans, after explantation of operated femoral bones of male Sprague Dawley rats. The whole study was conducted until 52W post op and μCT scans were done after 4W, 12W, 24W and 52W. Beam hardening artifacts were reduced to a minimum by applying aluminium filtration with 1.5 mm thickness (see 2.10 versus 2.11).

High resolution μCT images from the time points 4W and 52W are displayed in fig. 3.6, published by Kraus et al. [2]. No clear differences were noticed between the early time point and the late time point. Visible notches on the implant surface were present after 4W (see 3.6 b)) and also 52W (see 3.6 e)), a possible reason may be the use of a clamp during the implantation process. Numerical evaluation

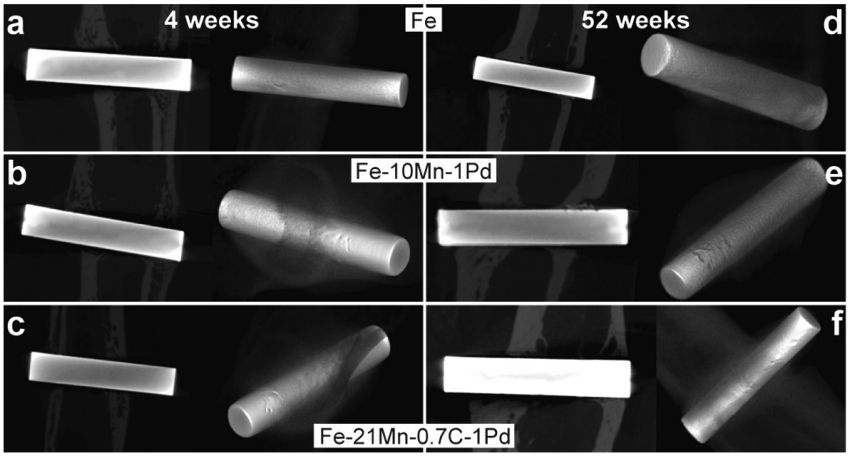

Figure 3.6: Conducted μCT scans of pure Fe, Fe-10Mn-1Pd and Fe-21Mn-0.7C-1Pd are displayed at the early time point 4W and the late time point of 52W. No evidence for visible degradation was found. Published in Kraus et al [2].

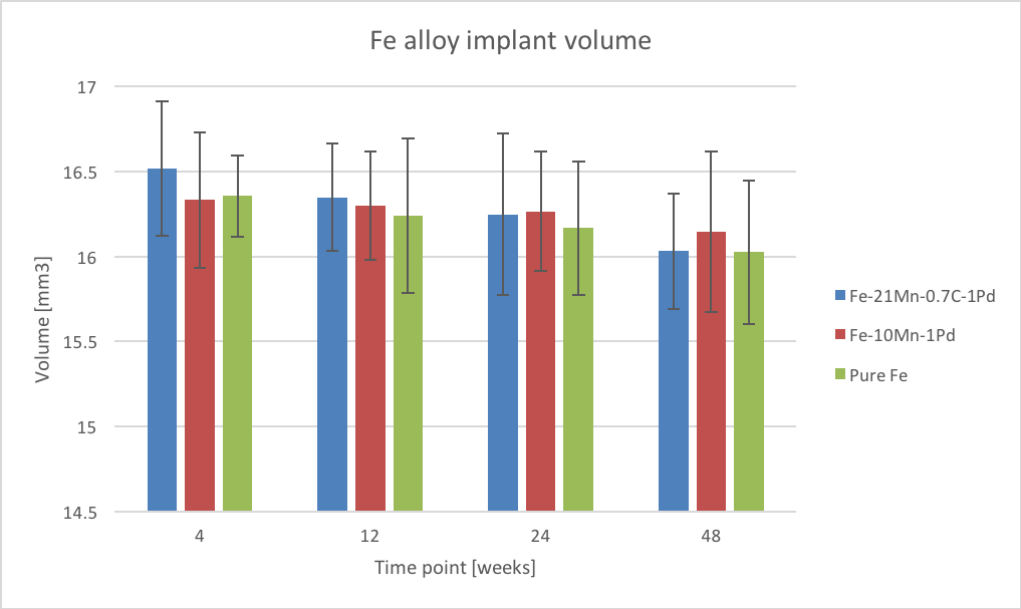

Figure 3.7: The volume loss of the materials Fe-10Mn-1Pd, Fe-21Mn-0.7C-1Pd and pure Fe was evaluated at 4W, 12W, 24W and 48W in vivo. Only minor changes in volume were noticed during the whole study period.

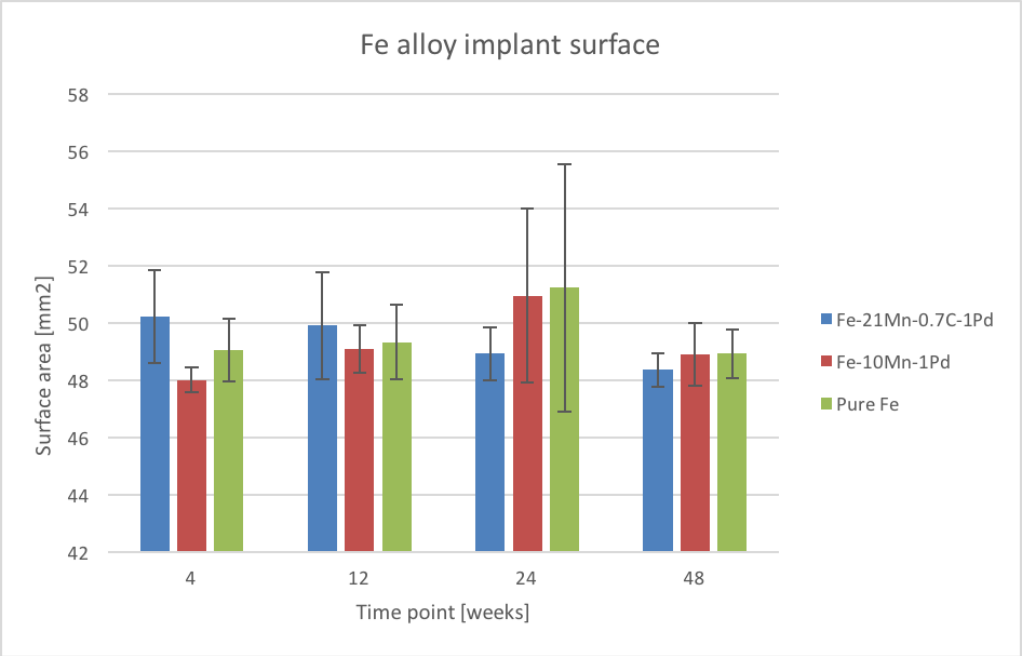

Figure 3.8: The surface alteration of the materials Fe-10Mn-1Pd, Fe-21Mn-0.7C-1Pd and pure Fe was evaluated at 4W, 12W, 24W and 48W in vivo. Only minor changes in surface were noticed during the whole study period.

4W		Volume mm^3			Surface mm^2		
Alloy	M	R	SD	M	R	SD	
Calculated	16.09	-	-	44.23	-	-	
Pure Fe	16.35	16.59 - 16.03	0.23	49.04	50.64 - 47.90	1.09	
Fe-10Mn-1Pd	16.33	17.11 - 16.04	0.39	48.00	48.47 - 47.34	0.42	
Fe-21Mn-0.7C-1Pd	16.48	17.08 - 16.02	0.39	50.23	51.70 - 47.12	1.62	

Table 3.5: Measured implant volume and surface with mean values (M), measurement range (R) and standard deviation (SD) after 4 weeks in vivo. Original implant volume and surface were calculated from a cylindric shape of 1.6 mm in diameter and a height of 8 mm.

12W		Volume mm^3			Surface mm^2		
Alloy	M	R	SD	M	R	SD	
Calculated	16.09	-	-	44.23	-	-	
Pure Fe	16.24	16.83 - 15.64	0.45	49.32	51.36 - 47.38	1.31	
Fe-10Mn-1Pd	16.29	16.77 - 15.82	0.31	49.08	50.53 - 48.15	0.83	
Fe-21Mn-0.7C-1Pd	16.34	16.8 - 15.89	0.32	49.91	53.12 - 48.44	1.86	

Table 3.6: Measured implant volume and surface with mean values (M), measurement range (R) and standard deviation (SD) after 12 weeks in vivo. Original implant volume and surface were calculated from a cylindric shape of 1.6 mm in diameter and a height of 8 mm.

24W		Volume mm^3			Surface mm^2		
Alloy	M	R	SD	M	R	SD	
Calculated	16.09	-	-	44.23	-	-	
Pure Fe	16.17	16.95 - 15.93	0.45	51.22	59.79 - 48	4.33	
Fe-10Mn-1Pd	16.26	16.96 - 16.05	0.35	50.95	56.72 - 48.36	3.04	
Fe-21Mn-0.7C-1Pd	16.25	16.74 - 15.52	0.47	48.92	50.34 - 47.68	0.91	

Table 3.7: Measured implant volume and surface with mean values (M), measurement range (R) and standard deviation (SD) after 24 weeks in vivo. Original implant volume and surface were calculated from a cylindric shape of 1.6 mm in diameter and a height of 8 mm.

48W		Volume mm^3			Surface mm^2		
Alloy	M	R	SD	M	R	SD	
Calculated	16.09	-	-	44.23	-	-	
Pure Fe	16.03	16.62 - 15.38	0.42	48.92	49.52 - 47.28	0.86	
Fe-10Mn-1Pd	16.15	16.71 - 15.35	0.47	48.89	50.69 - 47.43	1.09	
Fe-21Mn-0.7C-1Pd	16.03	16.24 - 15.34	0.34	48.35	49.06 - 47.72	0.59	

Table 3.8: Measured implant volume and surface with mean values (M), measurement range (R) and standard deviation (SD) after 48 weeks in vivo. Original implant volume and surface were calculated from a cylindric shape of 1.6 mm in diameter and a height of 8 mm.

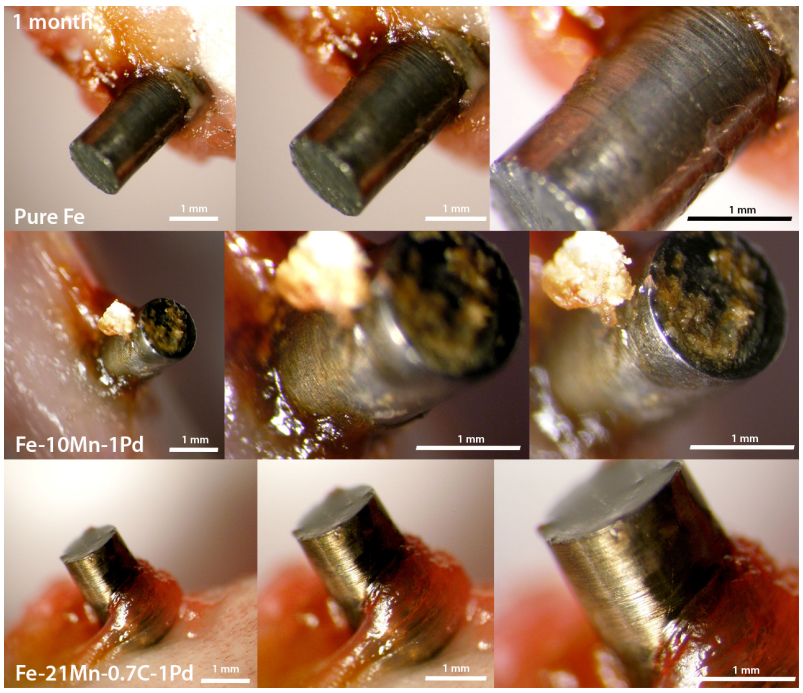

Figure 3.9: Femoral bones with Fe alloys were harvested for high resolution scanning after 4W.

of ex vivo micro CT data was displayed in tables 3.5, 3.6, 3.7 and 3.8. No significant differences in volume and surface were noticed between the implant groups. In vivo micro CT scans were not considered for numerical evaluation, due to the observed very low differences in volume and surface in ex vivo high resolution scans.

Macroscopic images were created at scheduled time points for bone explantation after 4W (see fig. 3.9), 12W (see fig. 3.10), 24W (see fig. 3.11) and 52W (see fig. 3.12). The macroscopic views do not show any influence of the implants surface condition after 52 weeks except some minor superficial changes in colour and tissue ingrowth.

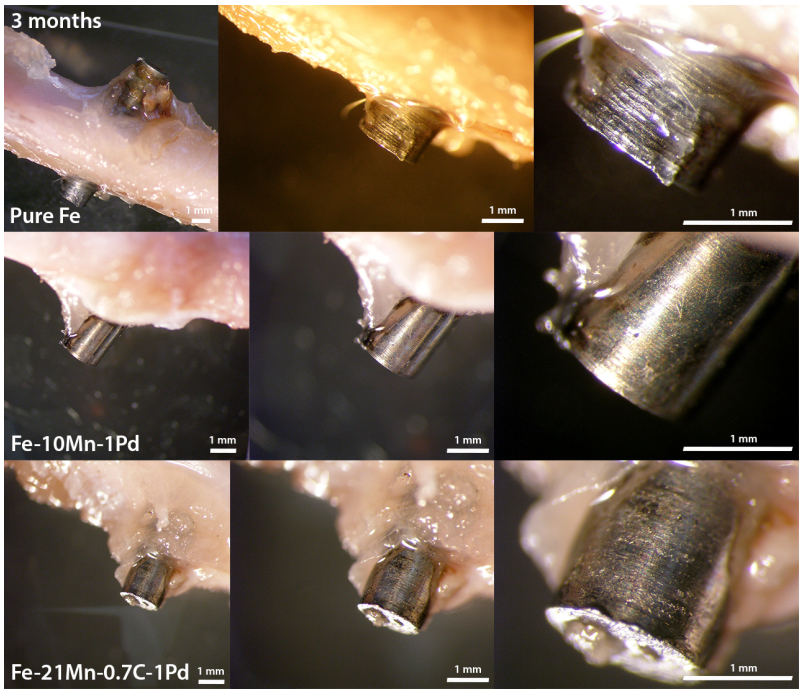

Figure 3.10: Femoral bones with Fe alloys were harvested for high resolution scanning after 12W.

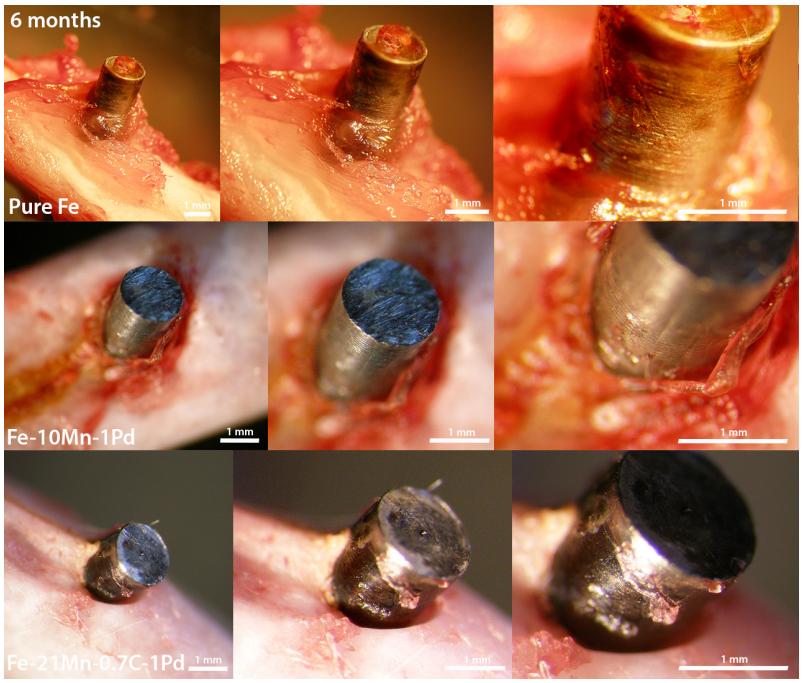

Figure 3.11: Femoral bones with Fe alloys were harvested for high resolution scanning after 24W.

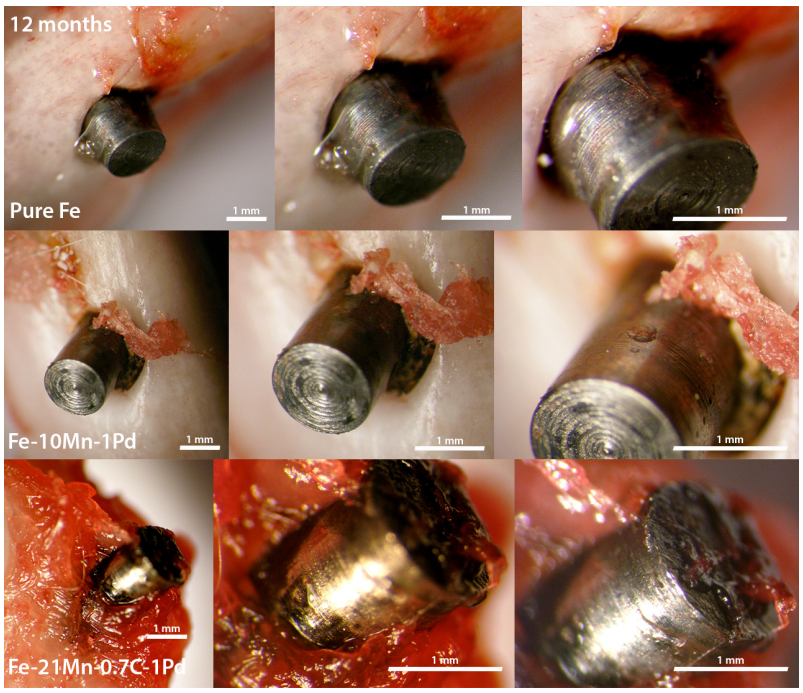

Figure 3.12: Femoral bones with Fe alloys were harvested for high resolution scanning after 52W.

3.3 Aim 3: Fluorescence Molecular Tomography (FMT) in transcortical rat model with osteoclast and osteoblast activity labelling fluorescent imaging agents in combination with micro CT imaging

FMT imaging was performed with the tracer Perkin Elmer Osteosense 750EX within four different study groups during a timespan of 12W for the experimental groups BR and GD, and 10W for the control and sham groups SM and KM. One animal of the BR group and another animal of the Gd group was lost during anaesthesia after week 3 and week 5. For this reason, results from week three are shown with a sample size of n=4 instead of initially n=6 for group BR. Results of GD were made with the corresponding sample size of n=4 after week 5.

Graphical results of the experimental and control/SHAM groups are shown in fig. 3.13 for the time points 2W, 3W, 5W and 8W. Fig. 3.14 shows further results after week 10 and week 12. Image numbering from 1 to 8 equals to the legend in the direction from top to bottom. A slight increase of fluorescence intensity in group GD can be noticed within fig. 3.13 beginning at week 2. A strong increase for the material GD was seen after 8W and also 10W in vivo (see fig. 3.14). The numerical evaluation of fluorescence intensity values shows the corresponding peaks in fig. 3.16.

Figure 3.15 shows a μCT scan of the GD animal's lower limbs, where the right tibia has an almost intact implant inside, while the left tibia was deformed by intense degradation and the consequential gas formation.

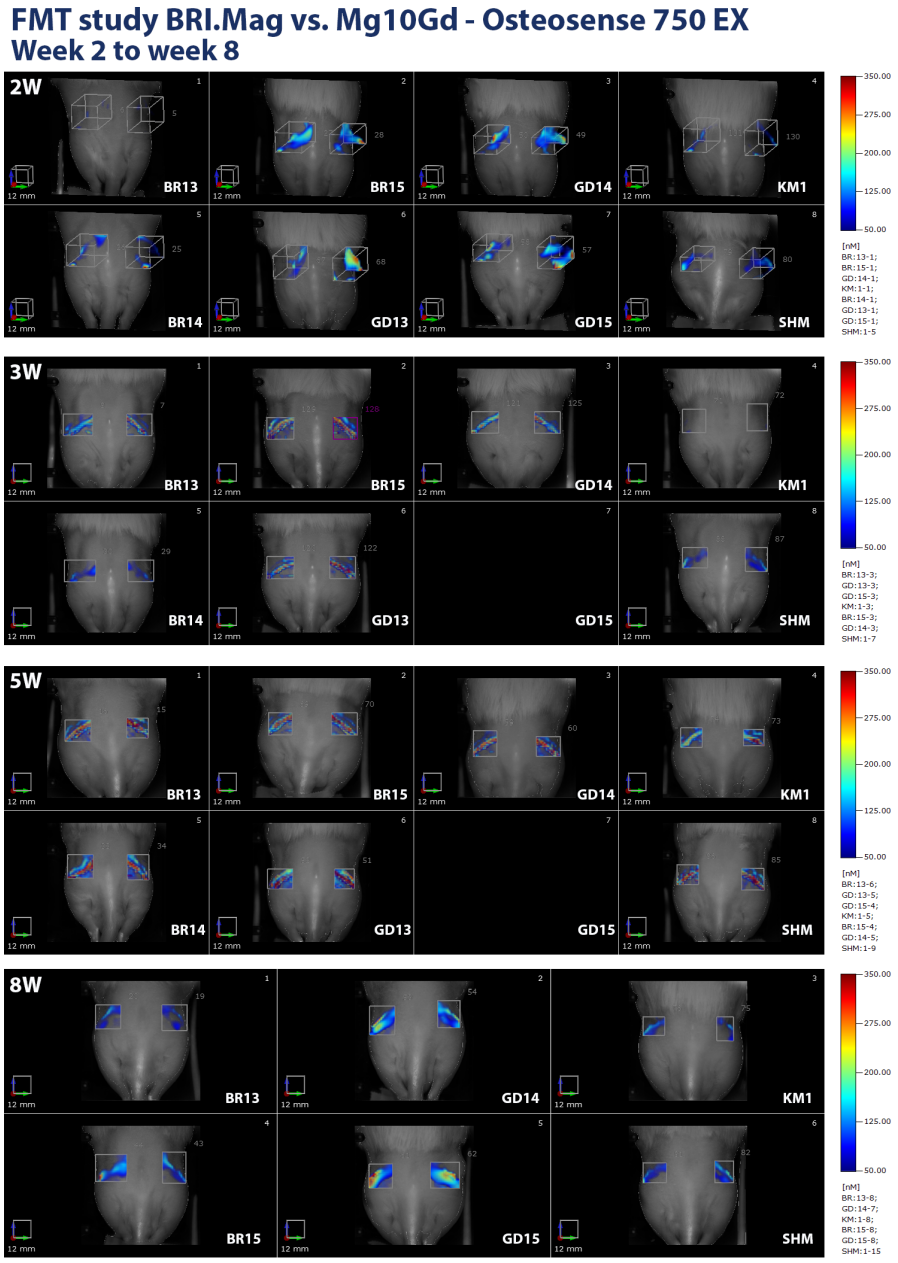

Figure 3.13: FMT imaging was performed with the fluorescent tracer Ostosense 750EX. Graphical results are displayed from week 2 to week 8. A ROI for measurement of fluorescent intensity was placed at the femoral bone site of implantation.

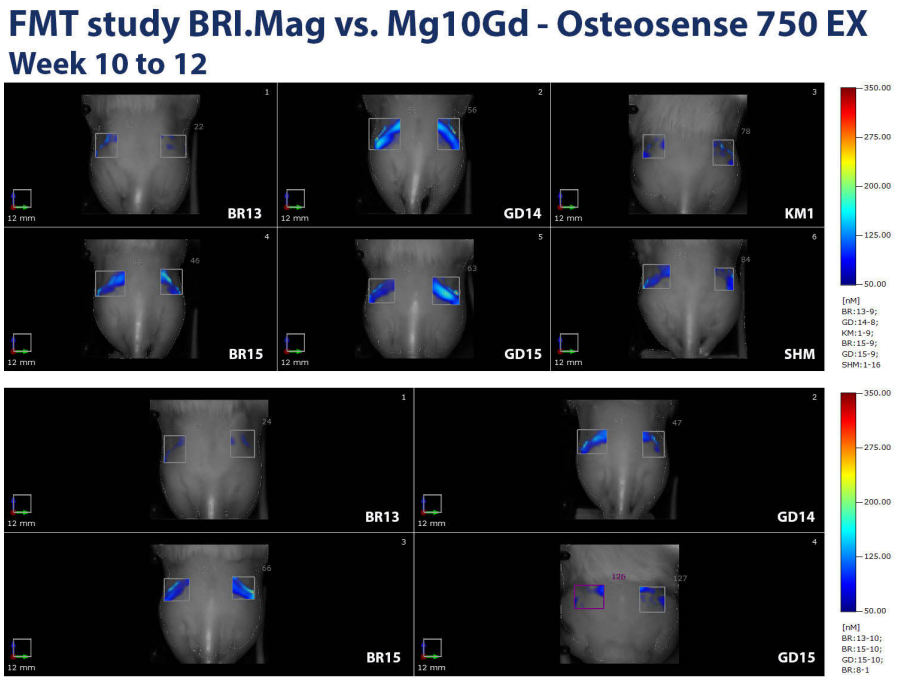

Figure 3.14: Graphical FMT results are displayed from week 10 to week 12. A ROI for measurement of fluorescent intensity was placed at the femoral bone site of implantation.

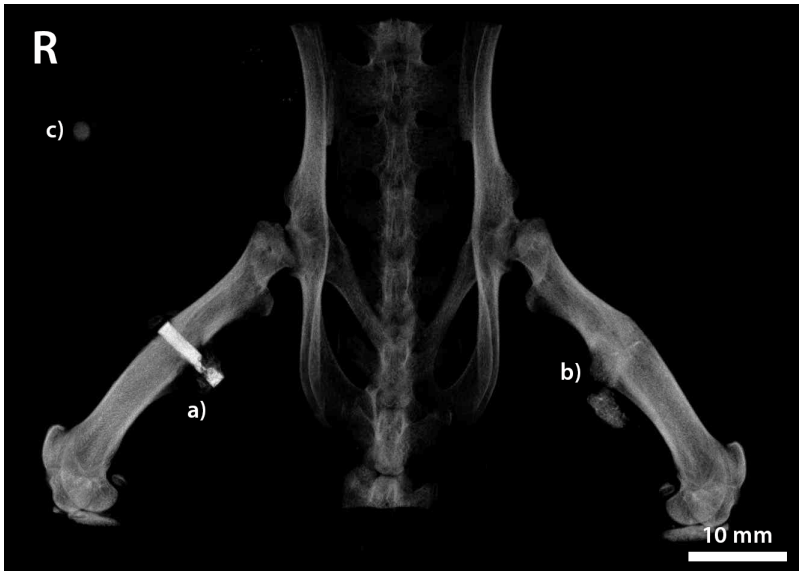

Figure 3.15: The μCT image shows an in vivo scan of the lower extremeties of a GD animal after 8W. The implant in the right leg a) has started corroding within the surrounding soft tissue. In the left tibia b), the GD implant was already dissolved leaving implant residuals inside the soft tissue. The bone shows deformation at the implant site caused by intense gas formation. c) shows one marker of the FMT imaging cassette for fixation of the animal. At least three markers are required for successful co-registration with FMT fluorescence data.

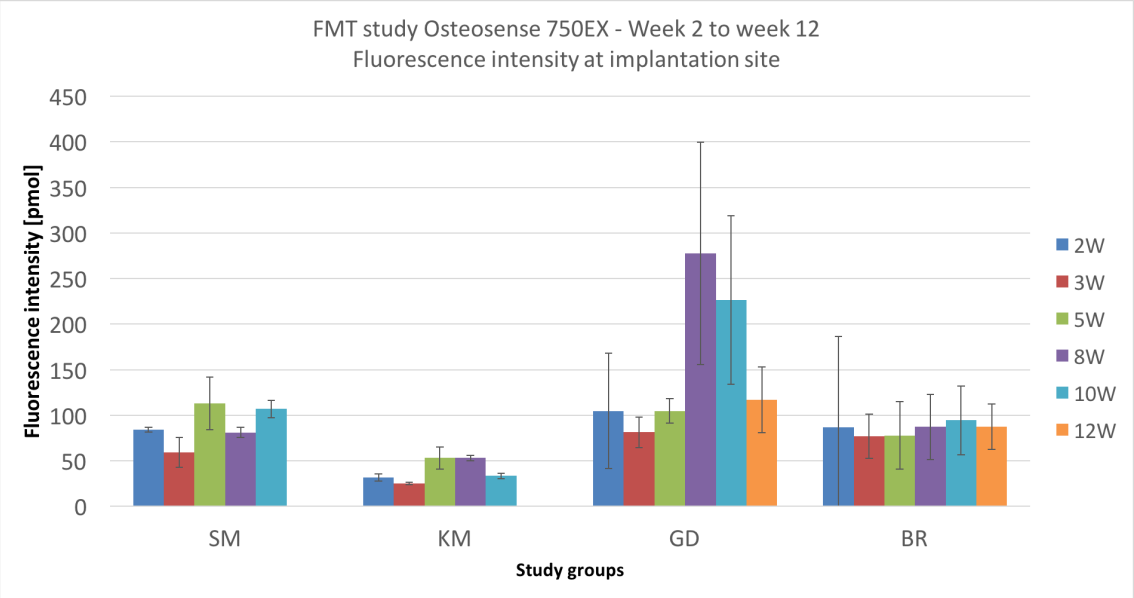

Figure 3.16: FMT imaging was performed with Osteosense 750EX over a study period of 12W. Sham group (SMn n=2) and control group (KM, n=2) were only imaged until week 10. Experimental groups with Mg10Gd implants (GD, n=6) and BRI.Mag implants (BR, n=6) were examined until week 12.

The control group KM exhibits a very low baseline value for fluorescence intensity, while the drilled sham group SM nearly shows the double amount comparable to the experimental group with BRI.Mag implant BR in fig. 3.16. Corresponding numerical results are shown in tables 3.9 and 3.10.

3.4 Aim 4: Micro CT supported biomechanical evaluation of ESIN interlocking systems in cadaveric sheep tibiae

Prepared cadaver bones were scanned in μCT after biomechanical testing at the Vienna Technical University and evaluated regarding internal bone damage load induced migration of interlocking screws. Coronal views and 3D reconstructions of the screw-bone compartment were created with Siemens Inveon Research Workplace v.2.2.2 and displayed in fig. 3.17. Clinical radiographs were made at the Department of Paediatric Radiology at the Medical University of Graz and are also shown in fig. 3.17.

The numerical evaluation of the risen cavities by screw migration was done in Materialise MIMICS® by creating a cylindric VOI around the lower half of the screw. The used VOI is overlapping the screw by 0.5 screw lengths like shown in fig. 3.18 (also compare fig. 2.17). Risen air cavities within the VOI were quantified by thresholding and 3D rendering. The calculation of the Cavity Volume fraction displayed in fig. 3.19 was done by subtracting the segmented screw volume from the VOI volume and calculating the percentage of cavity to total volume like in equation 3.1. Results of this aim were accepted for publication by the journal Materials Science and Engineering: C and are currently under revision.

2W	Intensity *pmol*		
Group	M	R	SD
SM	84.13	235.08 - 47.02	2.83
KM	31.45	217.31 - 43.49	3.99
GD	104.73	395.49 - 79.1	63.31
BR	86.78	375.03 - 24.18	99.81
3W			
SM	59.06	280.00 - 56.01	16.45
KM	25.05	92.10 - 18.44	1.08
GD	81.39	687.00 - 100.29	16.75
BR	76.81	434.55 - 36.99	24.46
5W			
SM	112.88	785.82 - 158.22	29.00
KM	53.09	691.63 - 143.00	12.22
GD	104.66	1579.61 - 114.28	13.55
BR	87.24	837.13 - 145.47	36.95
8W			
SM	81.12	240.82 - 48.13	5.54
KM	53.09	198.64 - 59.73	2.84
GD	277.89	487.83 - 63.57	122.00
BR	87.24	441.67 - 41.34	35.66

Table 3.9: Measured fluorescence intensity with mean values (M), measurement range (R) and standard deviation (SD) during 2 weeks to 8 weeks in vivo. Sample size for BR was reduced from n=6 to n=4 after week 3. Sample size for GD was reduced from n=6 to n=4 after week 8.

10W	Intensity *pmol*		
Group	M	R	SD
SM	106.75	208.45 - 41.69	9.43
KM	33.29	202.23 - 60.73	2.83
GD	226.15	308.51 - 54.11	92.44
BR	94.45	231.71 - 32.26	37.76
12W			
GD	116.67	312.27 - 97.02	35.81
BR	87.52	226.05 - 24.81	24.91

Table 3.10: Measured fluorescence intensity with mean values (M), measurement range (R) and standard deviation (SD) during 10 weeks to 12 weeks in vivo. GD sample size was reduced to n=2 for time point 12W.

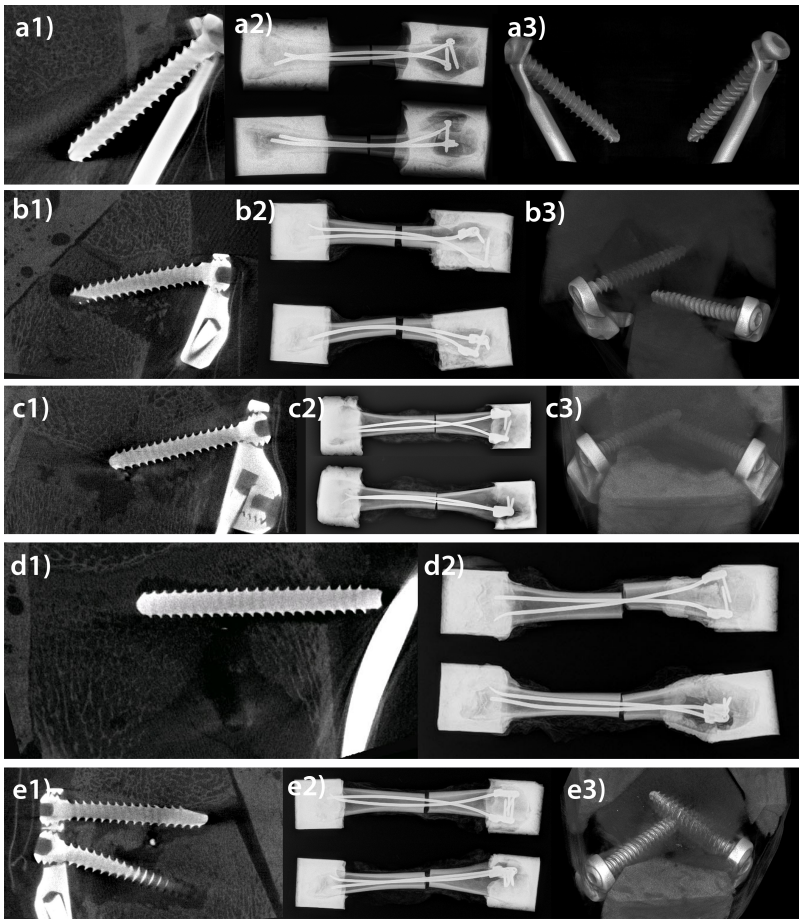

Figure 3.17: Used interlocking systems Ender nail a), Plug 3.5 b), Fixplug c), Plug 3 d) and Twin plug e) are displayed within this figure. μCT coronal views are displayed in a-e 1), a-e 2) show clinical radiographs, performed at the Department of Paediatric Radiology, Medical University of Graz, a-c 3) and e3) show 3D reconstructions of μCT data.

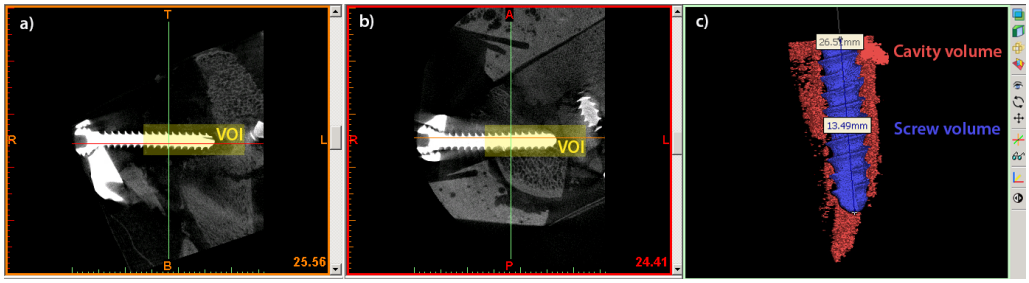

Figure 3.18: Materialise MIMICS® was used to evaluate the risen cavity after biomechanical testing and migration of the used interlocking screws. The VOI was defined surrounding the lower half of the screw (see a) in coronal view and b) in sagittal view). Segmented screw and cavity volumes are shown in c).

$$\frac{CV}{TV} = \frac{Vol_{Cavity}}{Vol_{VOI} - Vol_{Screw}} \tag{3.1}$$

Numerical values, calculated from equation 3.1, are shown in table 3.11.

3.5 Aim 5: Clinical CT imaging of degradable Magnesium ESIN implants in the growing sheep model

All used large animals were longitunially observed with clinical CT imaging to assess the degradation behaviour and reactions of surrounding bone and tissue within the same animals. All CT scans were produced at the Department of Radiology, Medical University of Graz (see fig. 3.20, right). Anaesthesia of animals was conducted at the Department of Experimental Surgery, Medical University of Graz (see fig. 3.20, left).

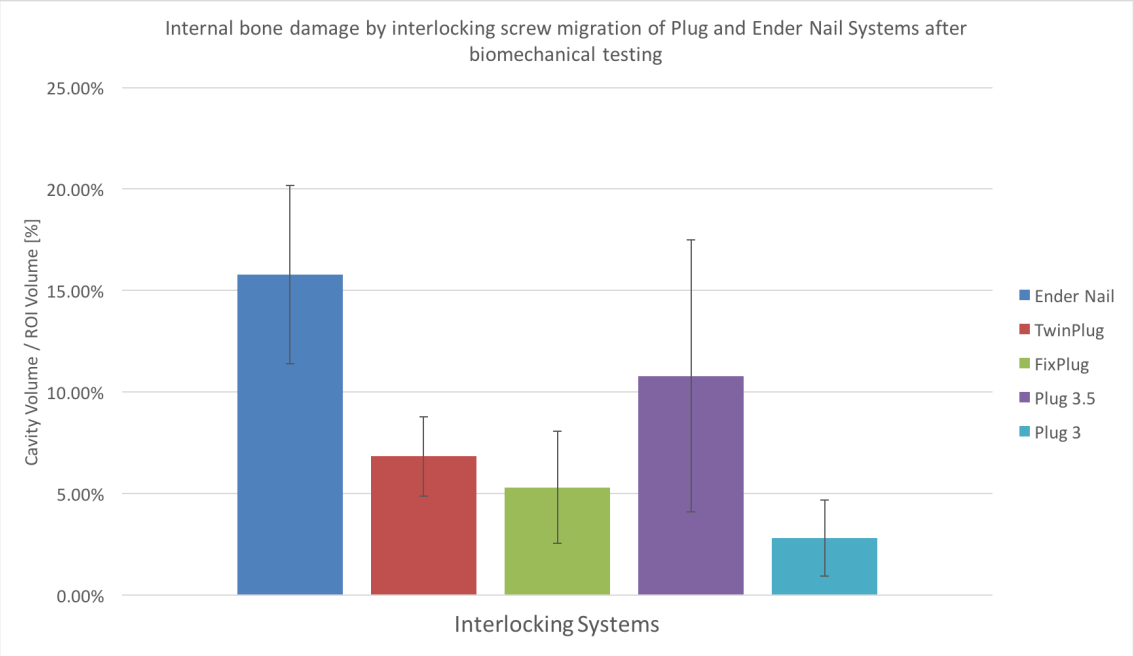

Figure 3.19: The numerical evaluation of the risen cavity volume was calculated in Materialise MIMICS® and evaluated in MS Excel. Ender Nail and Plug 3.5 systems show the highest cavity volumes in relation to measured VOI volumes.

System	$\frac{CV}{TV}$		
	%	%	%
Group	M	R	SD
EnderNail	15.79	20.60 - 7.59	0.04
TwinPlug	6.84	10.17 - 4.80	0.02
FixPlug	5.30	11.32 - 3.09	0.03
Plug 3.5	10.79	28.54 - 5.99	0.07
Plug 3	2.82	6.52 - 0.90	0.02

Table 3.11: Measured internal bone damage by interlocking screw migration with mean values (M), measurement range (R) and standard deviation (SD) after biomechanical testing.

Figure 3.20: General anaesthesia was induced by an intravenous injection of Ketamine and kept up using a circular breathing system with volatile Sevolflurane in combination with Propofol. Anesthetized animals were scanned in clinical CT with mobile ventilation and Propofol infusion attached.

3.5.1 G1 vs. G2: degradation behaviour of BR3 (two 3 mm implants, n=3) vs ZX10 (two 3 mm implants, n=2), no fracture

The alloys BRI.Mag® and ZX10 were extruded to rods of 3 mm in diameter and manufactured to clinically usable ESIN nails. After surgical implantation without fracture, clinical CT time points were scheduled to assess and compare the degradation, gas development and reaction of surrounding bone in vivo.

Figure 3.21 shows sagittal views of clinical CT images from week 2 to week 76. Gas formation was noticed beginning at week 2, followed by an increased production at week 6, which continued until week 24. ZX10 degradation started with the same amount of hydrogen gas formation at week 2 and continued with an almost linear, but slight increase until week 52 which is displayed in fig. 3.25. The 3D rendered implants in fig. 3.23 show the progress of degradation for BRI.Mag®, which shows first clear alterations in shape after week 24. Week 52 shows a heavily corroded implant and week 76 an almost dissolved ESIN nail. In contrast to BRI.Mag®, ZX10 seems to be completely intact after 24 weeks in fig. 3.24 and starts to show visible degradation after week 52. Both materials were implanted crossing the animals proximal epiphyseal plate. However, no indication for growth rest or any differences in bone length was noticed in comparison to the control group (see also fig. 3.26) or also the untreated contralateral legs.

3.5.2 G3: untreated control group, CTRL (n=3)

The control group CTRL was housed together with all other experimental animals and did not receive any surgical treatment. Only anaesthesia for clinical CT imag-

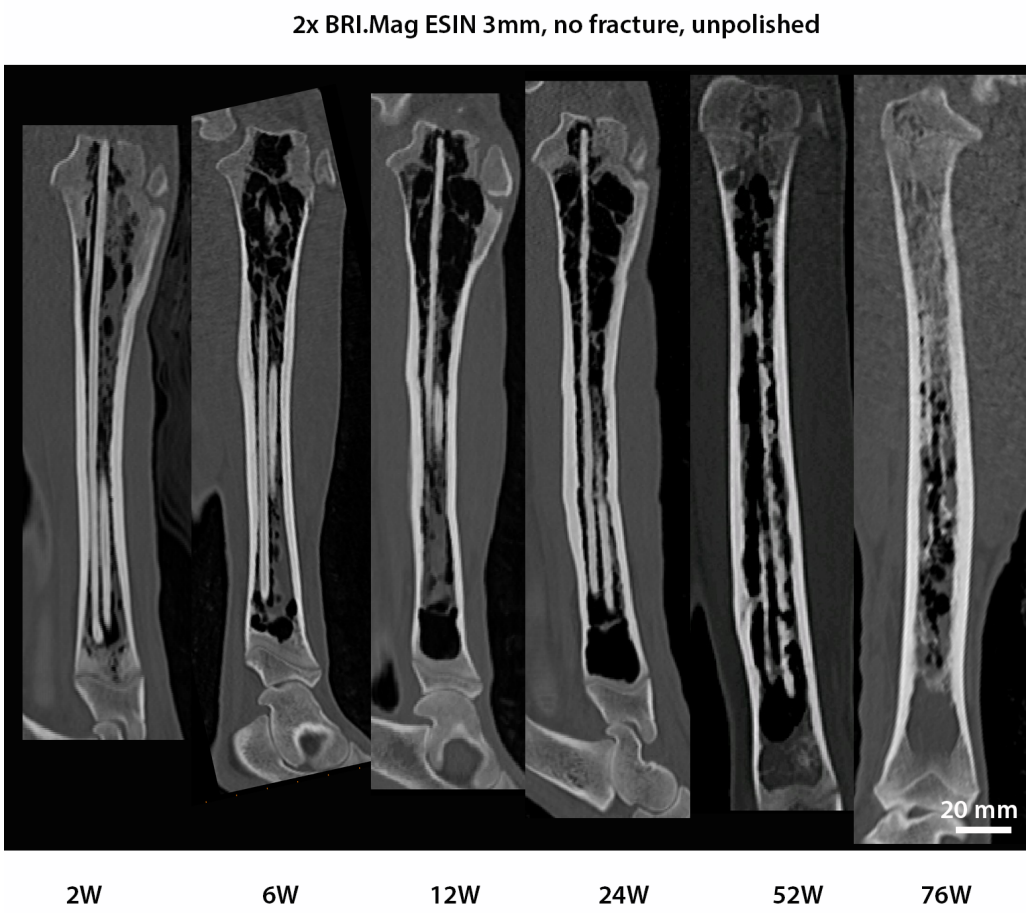

Figure 3.21: Clinical CT scans were performed after 2W, 6W, 12W, 24W, 52W and 76W in vivo at the Department of Radiology, Medical Universtity of Graz.

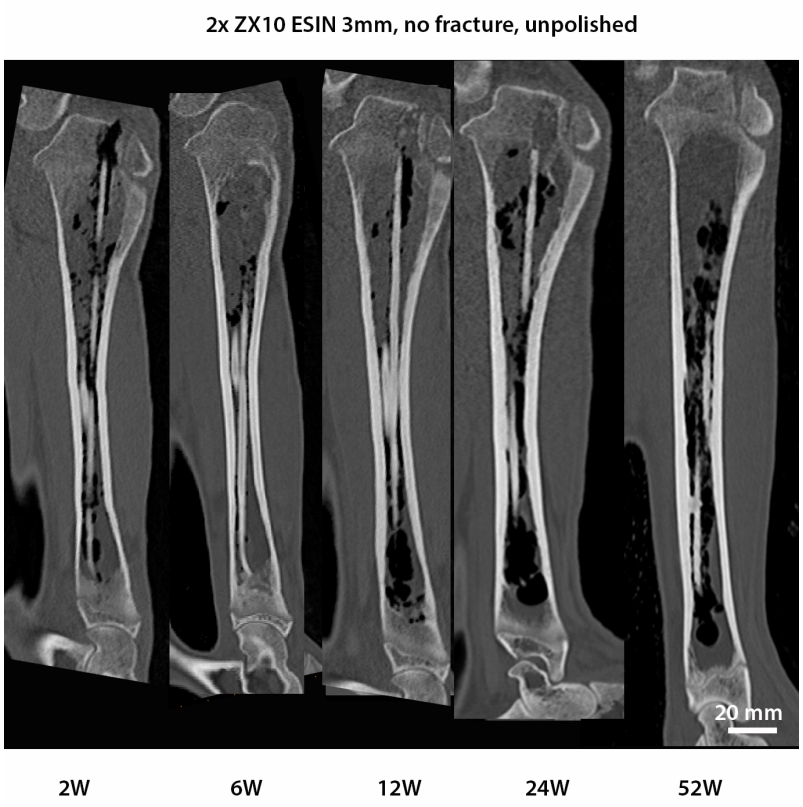

Figure 3.22: Clinical CT scans were performed after 2W, 6W, 12W, 24W, 52W and 76W in vivo at the Department of Radiology, Medical Universtity of Graz.

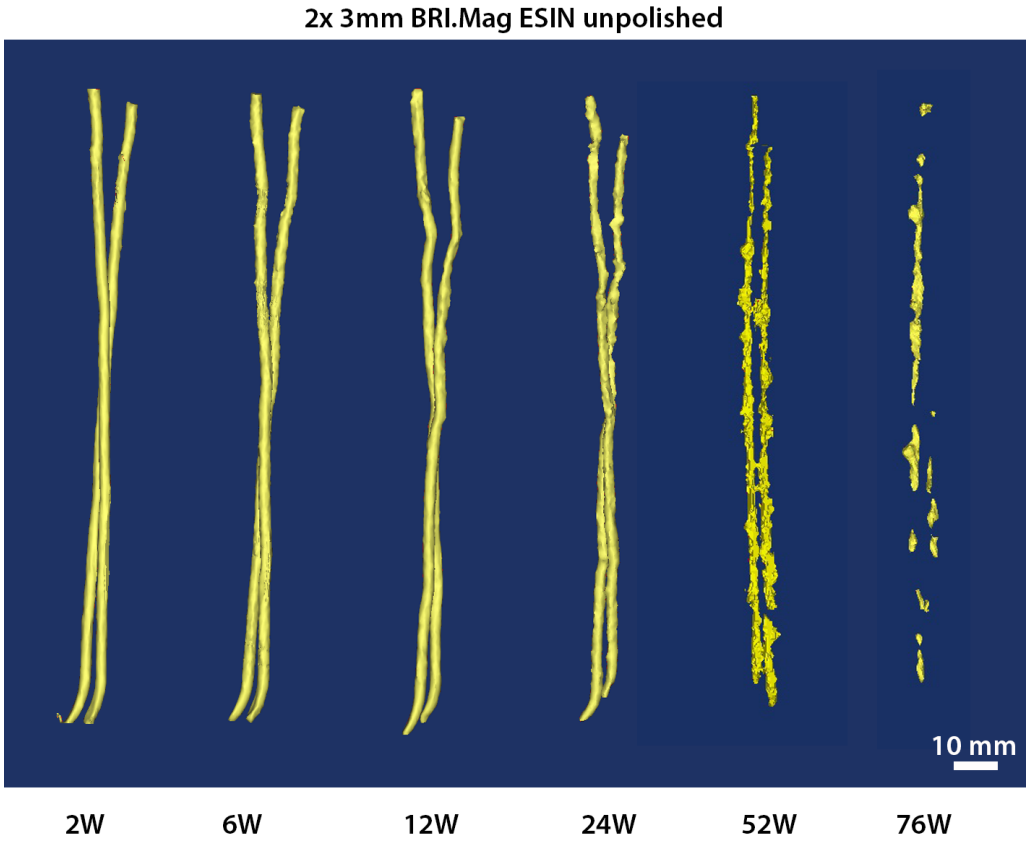

Figure 3.23: Clinical CT data was produced in DICOM format an post processed in Materialise MIMICS®. Segmentation of bone and implant resulted in a 3D reconstruction of all implant stages during week 76. High volumes of gas cavities were found from week 6 to week 24 continued by a decrease after 52 weeks. Clear degradation is starting at week 24, implants are almost dissolved after week 76.

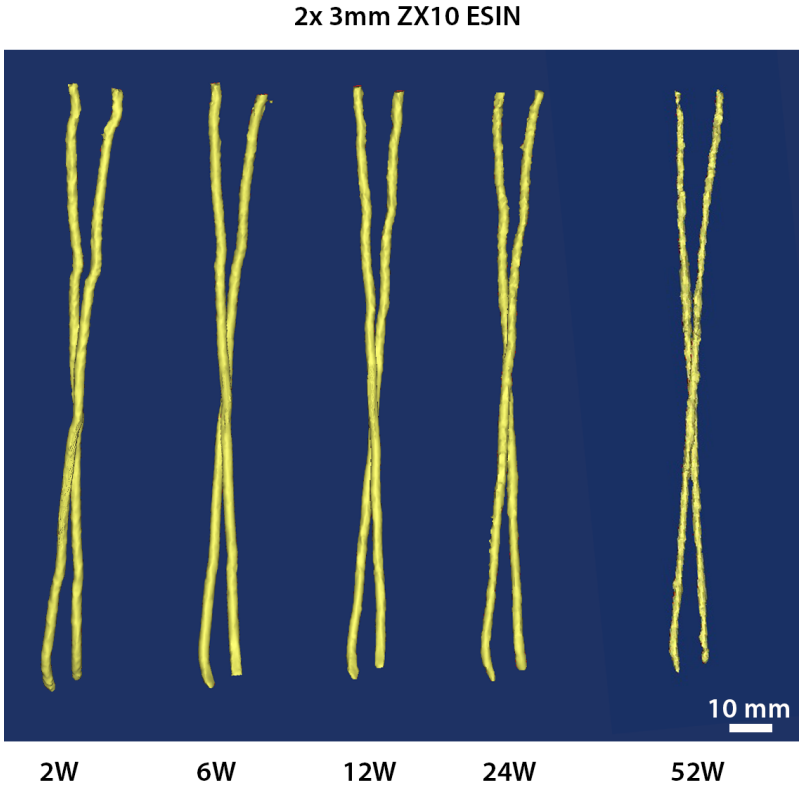

Figure 3.24: Intramedullary ZX10 implants were segmented from bone and reconstructed to 3D images. Clear influence of degradation on the implant shape is visible after week 52, the production of hydrogen gas started increasing after week 24.

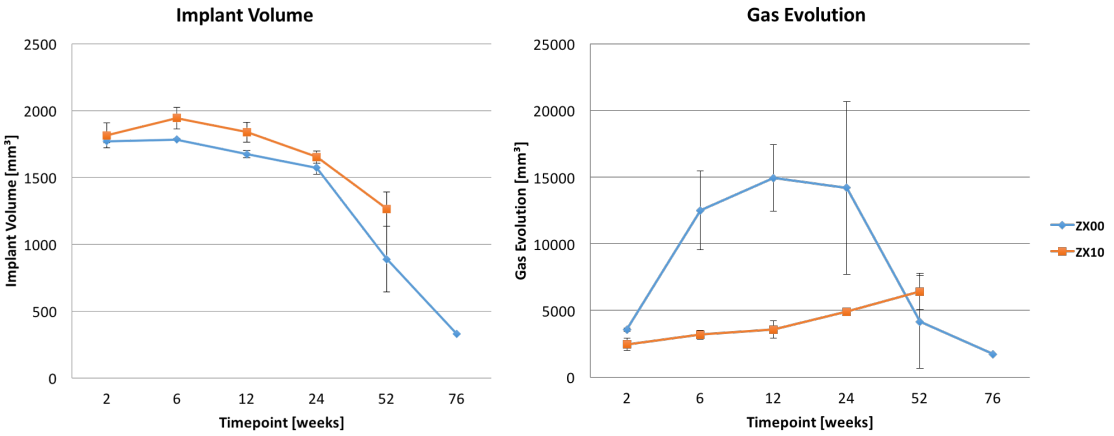

Figure 3.25: Implant degradation and formation of gas cavities was numerically evaluated from CT data for the alloys ZX00 (BRI.Mag®) and ZX10 in vivo. BRI.Mag® shows a high release of hydrogen gas beginning at week 6 and also a faster decrease in volume. ZX10 gas release is quite linear increasing until week 52.

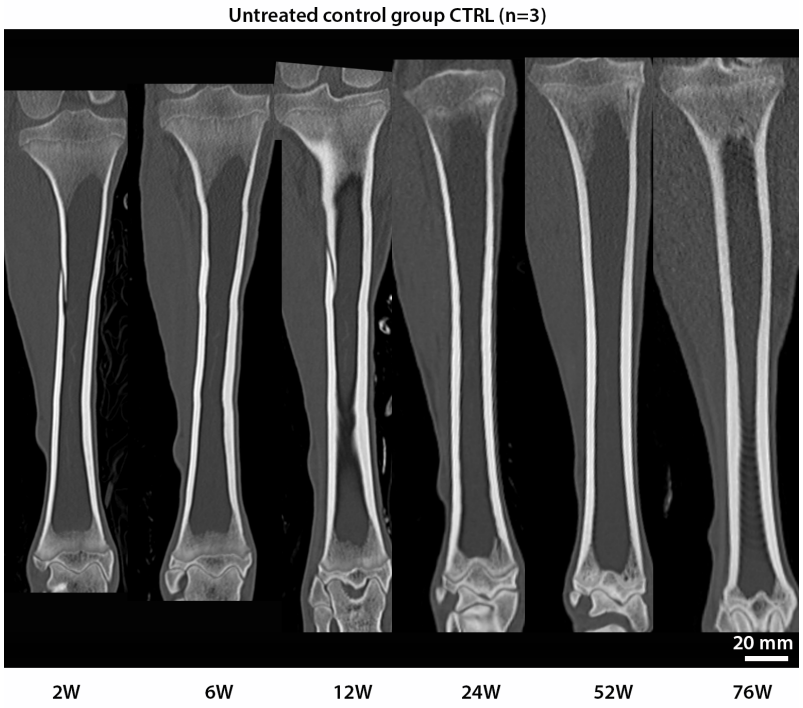

Figure 3.26: Clinical CT imaging of untreated control CTRL from week 2 to week 76.

ing had to be performed. Radiological results of control group in 3.26 were used for comparison regarding bone length and reactions of epiphyseal plates and bone tissue.

3.5.3 G4 vs G5: transcortical BR3 in epiphysis (n=2) , diaphysis, distal metaphysis vs conventional Ti (n=1)

Transcortical implantation of BRI.Mag® ESIN pins was performed at three different locations. Proximal epi-/metaphysis, middle diaphysis and distal epi-/metaphysis were implanted and monitored with in vivo clinical CT. The resulting images show a close bone incorporation, especially for the diaphyseal implant in 3.27, with almost

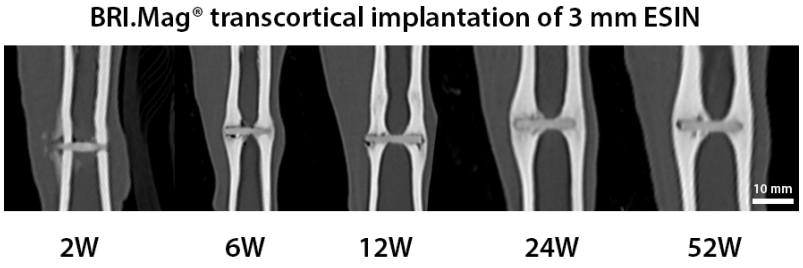

Figure 3.27: Diaphyseal transcortical implantation of 3 mm BRI.Mag ESIN shows strong callus formation during the study and good bone contact after 52W.

no gas formation until week 52. The corresponding implantation of conventional Ti ESIN was removed before imaging in week 6. Callus formation and thickening of cortical bone is clearly increased in comparison to Ti (see fig. 3.27 and 3.28), starting at week 6.

3D reconstructions in Materialise MIMICS® were used to achieve a detailed view on bone formation surrounding the implants and the localisation and amount of hydrogen gas. Fig. 3.29 shows an initially higher release of gas at the proximal epiphysis and the distal epiphysis, which is decreasing during the study. This behaviour is also found in numerical data in fig. 3.31. Both growth plates were crossed during the implantation process. However, 3D reconstructions show a clear bone growth after 24W where the proximal and distal implants were both transported out of the growth plates and a breakage of the proximal implant was notices at week 52. The Ti implant did not show any effects on bone growth in fig. 3.30 after the second removal operation at week 6. Unfortunately this animal could not be monitored after week 12 due to death caused by intestinal obstruction.

Numerical evaluation in fig. 3.31 shows slight differences in implant locations. Proximally implanted BRI.Mag® pins exhibit the highest gas formation at 2 weeks after

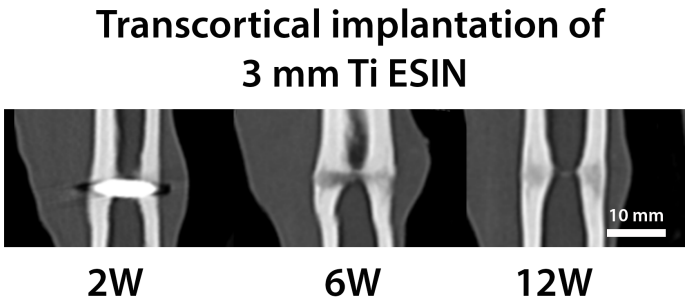

Figure 3.28: Diaphyseal implantation of Ti ESIN pins were monitored until week 12 in vivo. Pins were removed at imaging time point week 6, in order to simulate a clinical implant removal. Imaging results show beam hardening artifacts at week 2 around the Ti pin. No callus formation is visible at this timepoint. The image at week 6 was taken directly after implant removal. Week 12 shows an almost completed bone healing.

implantation, which was decreasing very fast until week 6. This behaviour was also observed for implantation in the distal epiphyseal area. However, all three implant volumes increased after 24 or 52 weeks, which may be an indication for measured degradation products.

3.5.4 G6: fracture model, 90° fracture at middle diaphysis, BR3 implants (2 implants), fixateur externe for 6 weeks (n=1)

The first fracture model was performed with a 90° horizontal osteotomy followed by the stabilization of the two bone ends by ESIN osteosynthesis with two 3 mm BRI.Mag® nails. In consequence to missing stability with cast bandage and a breakage of implants in all pilot animals, a fixateur externe was used to achieve a stable fracture until week 6. Numerical evaluation was performed in fig. 3.33 after week 6,

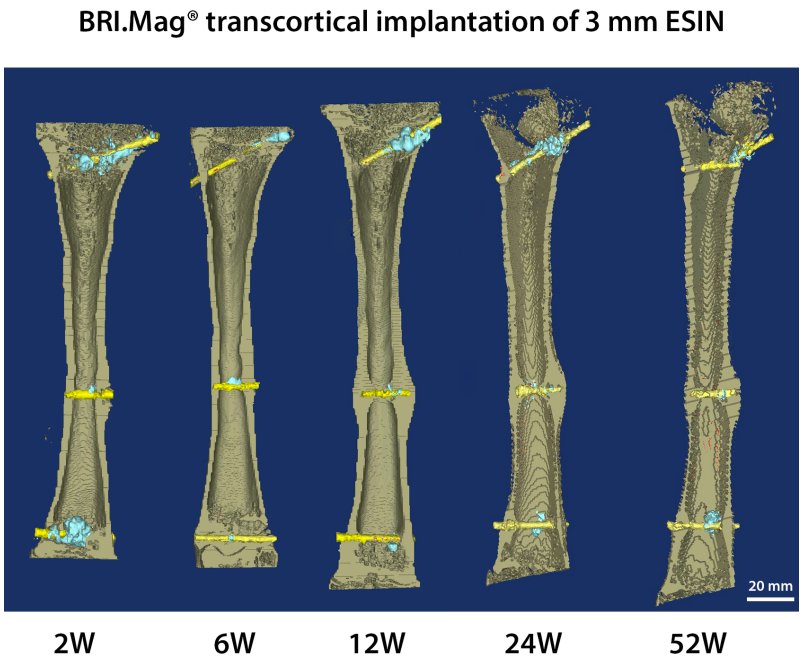

Figure 3.29: The transcortical implantation of 3 mm BRI.Mag shows callus formation at week 12, decreasing until week 52. A close bone implant interface was formed in the diaphyseal area. The implantation into the proximal and distal epiphysis did not lead to growth rest. Both implants were transported to the diaphyseal area during growth.

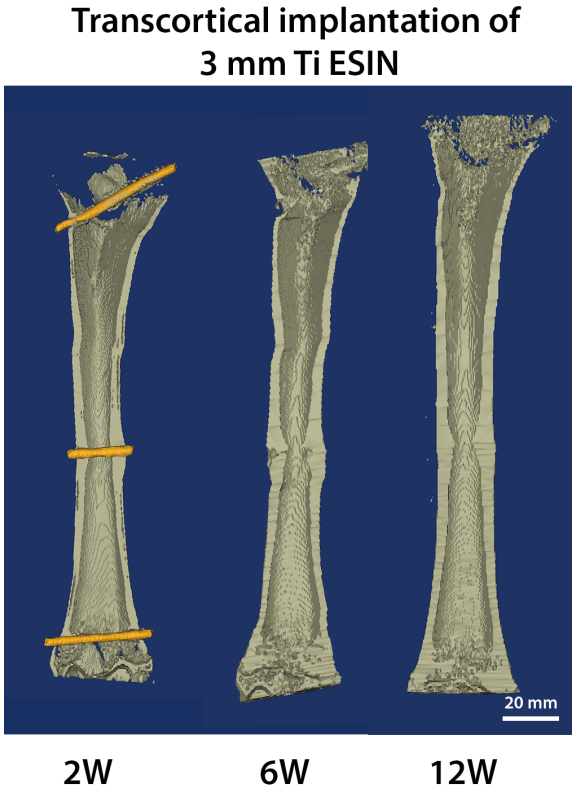

Figure 3.30: Radiological CT data of transcortically implanted Ti ESIN pins was 3D reconstructed in Materialise MIMICS®. The Ti pins were removed before imaging at time point 6W. The 3D reconstruction shows a slight callus residual and empty implantation sites after 6 weeks. After 12 weeks the bone has healed completely, thickening of cortical bone in the diaphyseal area is noticeable.

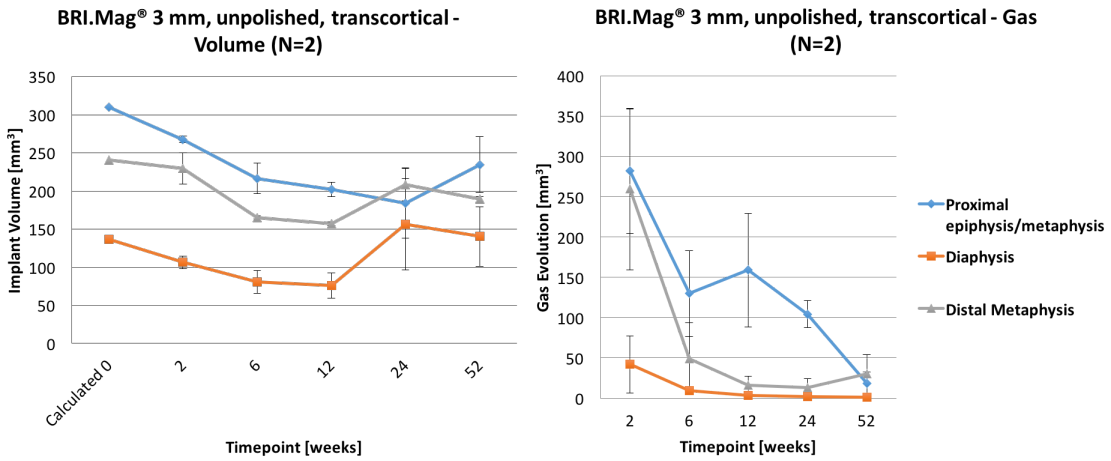

Figure 3.31: Transcortically implanted BRI.Mag was monitored over 52 weeks in vivo and exhibited different behaviour depending on the location. Diaphyseally implanted material was hardly showing gas and had been closely incorporated by surrounding bone. Highest amount of degradation and gas development was noticed for the proximal epiphysis.

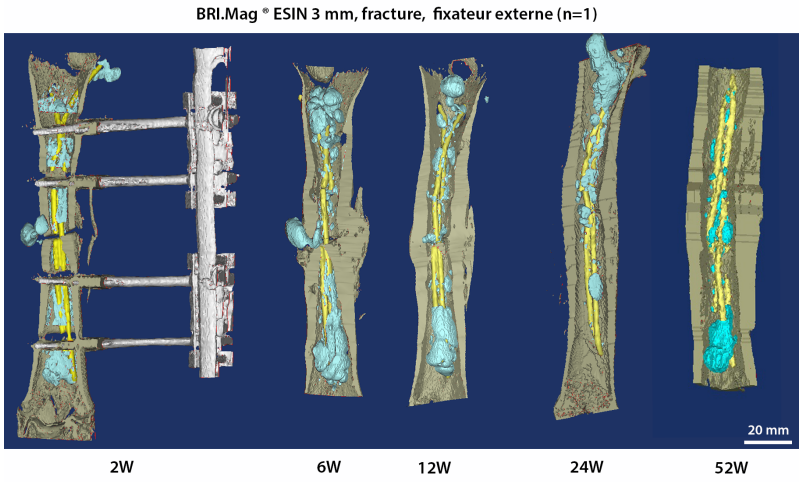

Figure 3.32: The 90° horizontal osteotomy was stabilized with two 3 mm BRI.Mag® ESIN nails. The fixation device was removed after 6 weeks, when an almost fully consolidated callus was formed. Progress over 52 weeks shows a completed bone healing with a noticeable thickening of diaphseal cortex at the fracture site.

because the presence of the external fixation screws was extensively producing artifacts on CT imaging, which is also noticed at the 2W image in fig. 3.32. Summed up, the gas development of externally fixated BRI.Mag® was comparably low and the measured volume showed the highest levels after 24 weeks and 52 weeks in fig. 3.33.

The comparison of all measured 3 mm implants in fig. 3.33 shows only slight differences in volume development between ZX10 and BRI.Mag® in polished and unpolished versions. Polished BRI.Mag® shows an high increase in volume after 12W in vivo, which may be a consequence of unwanted measurement of extensively distributed degradation products around the implant. The gas development of the polished samples of BRI.Mag and ZX10 was considerably lowered. However, polished ZX10 experienced an huge increase after week 24, while the initially highly

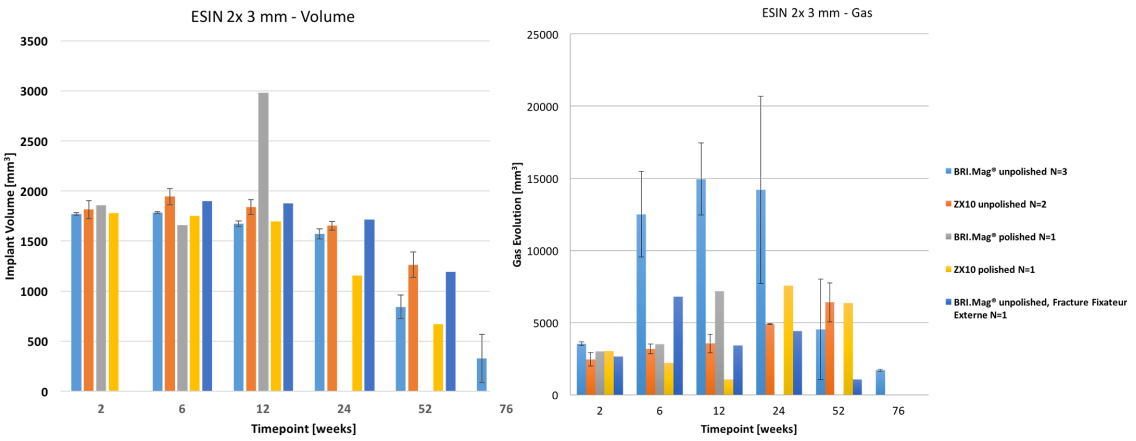

Figure 3.33: The numerical evaluation of all used 3 mm implants was compared over a timespan of 52 weeks (76 for BRI.Mag® without fracture)in vivo.

releasing unpolished BRI.Mag® decreased constantly to a very low value at week 76. At 52 weeks, unpolished BRI.Mag and also the polished ZX10 show half or less than half remaining implant volume.

3.5.5 G7: degradation behaviour of polished BR45-pol and unpolished BR45 (1 implant), no fracture (n=2)

The influence of mechanical polishing was examined in two animals with the implantation of polished and unpolished 4.5 mm diameter BRI.Mag® ESIN. While the unpolished material shows increasing formation of hydrogen gas within the medullary cavity (see fig. 3.34 and fig. 3.36), the influence of a polished surface seems to homogenize the gas development, which can be clearly noticed in fig. 3.35. Increased implant volumes were measured for both implants at week 12, which decreased to a normal level at week 24 in fig. 3.36.

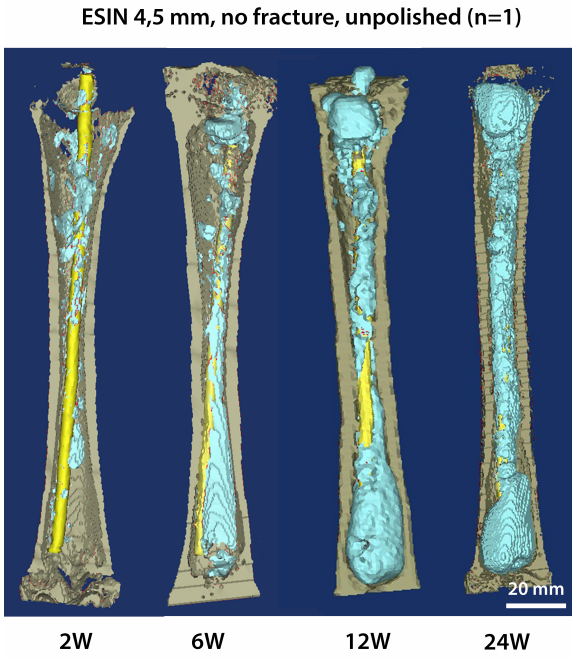

Figure 3.34: One BRI.Mag® ESIN nail was implanted intramedullary and monitored until 24 weeks after implantation. Continous increase in gas development is shown.

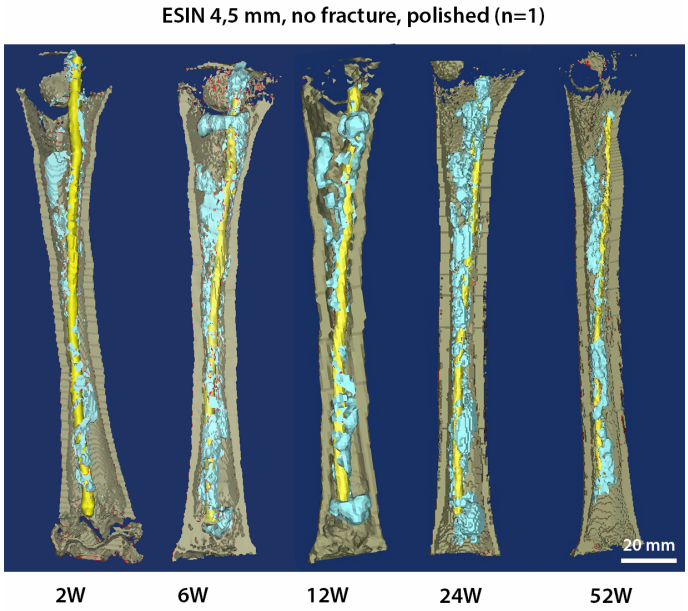

Figure 3.35: Single implantation of 4.5 mm BRI.Mag® implant with polished surface. Gas development caused by corrosion is very moderate during the whole study period.

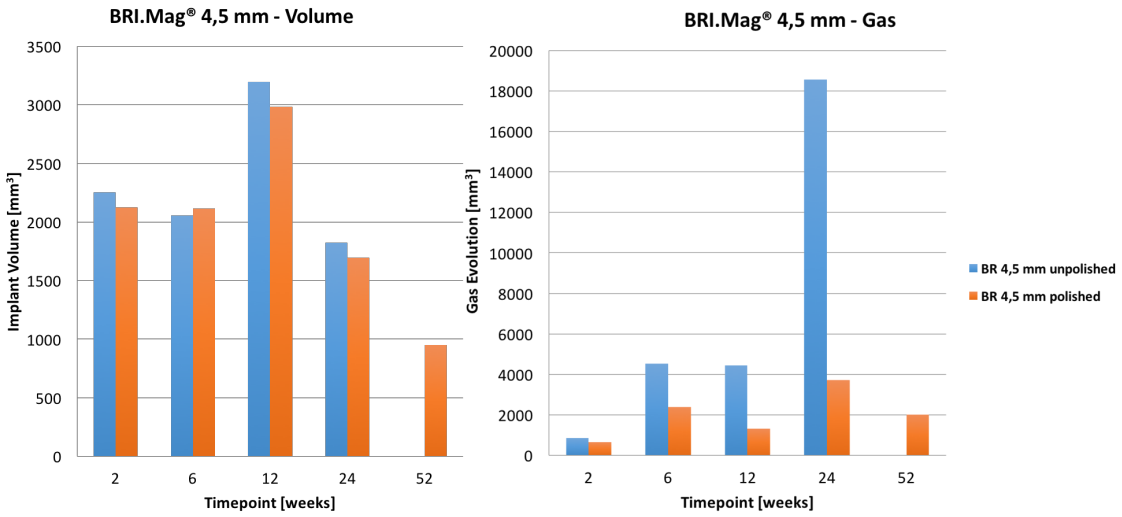

Figure 3.36: Numerical evaluation of 4.5 mm BRI.Mag® ESIN implants was performed for polished and unpolished material. Unpolished BRI.Mag® was only monitored until week 24 due to the loss of the sheep attacked by wild animals.

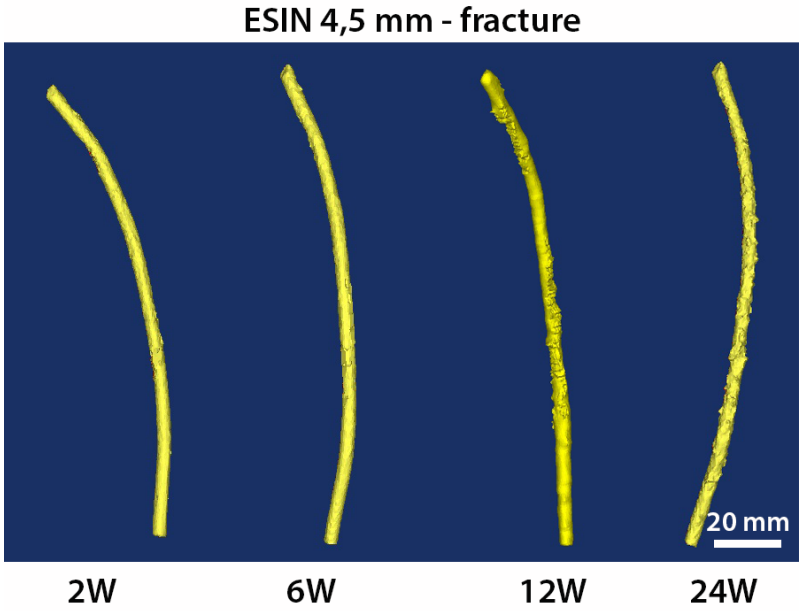

Figure 3.37: 3D rendered implant created in Materialise MIMICS® from human CT data. Visible implant degradation is starting after 24W.

3.5.6 G8 vs. G9: BR45-pol implants, fracture, fixateur externe vs. cast

Fracture treatment with 4.5 mm implants was simulated by surgical osteotomy at right sheep tibiae with 30° oblique fracture. This fracture was treated with ESIN osteosynthesis by polished 4.5 mm BRI.Mag® nails. One pilot group was performed with additional cast bandage after surgical intervention and osteosynthesis. Mechanical stability with cast could only be ensured in n=2 animals. N=5 animals experienced re-fracture of the implant, resulting in a non stable osteosynthesis and were excluded from the study. N=6 further animals were operated in a similar way with an additional external fixation, in order to ensure stability until a stable callus is formed.

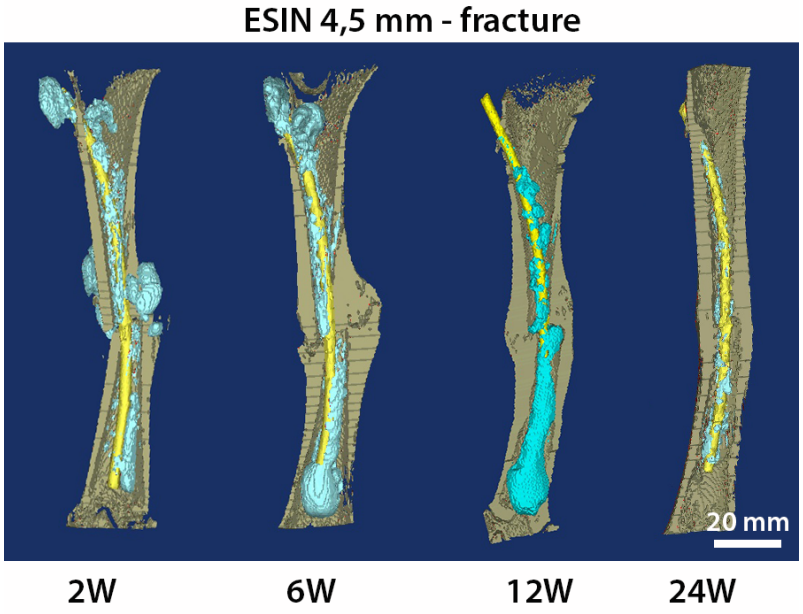

Figure 3.38: 3D rendering of bone, implant and gas shows good callus formation after 6W in vivo. A completely mineralized, decreasing callus is noticed after 12W, which is already resorbed after 24W. Hydrogen gas formation is continuously decreasing for polished 4.5 mm ESIN.

Decreasing gas formation was noticed for the cast stabilized group from a higher initial value at week 2 to a very moderate amount after finished fracture healing at week 24 (see fig. 3.38). Two out of three animals in the external fixation group started with low gas values at week 6 followed by an increase of hydrogen evolution as displayed in fig. 3.40. Fig. 3.39 shows the development of the third animal, which experienced higher gas values at week 6 decreasing until week 24. The other two animals within this group were lost through infections caused by osteomyelitis.

All numerical evaluations of the cast stabilized group in fig. 3.40 were done with a group size of n=2 animals. Data of animals with external fixation was gathered for n=3 animals at time points 6W and 12W. Due to loss of experimental animals caused by osteomyelitis, the 24W time point shows only data from n=1.

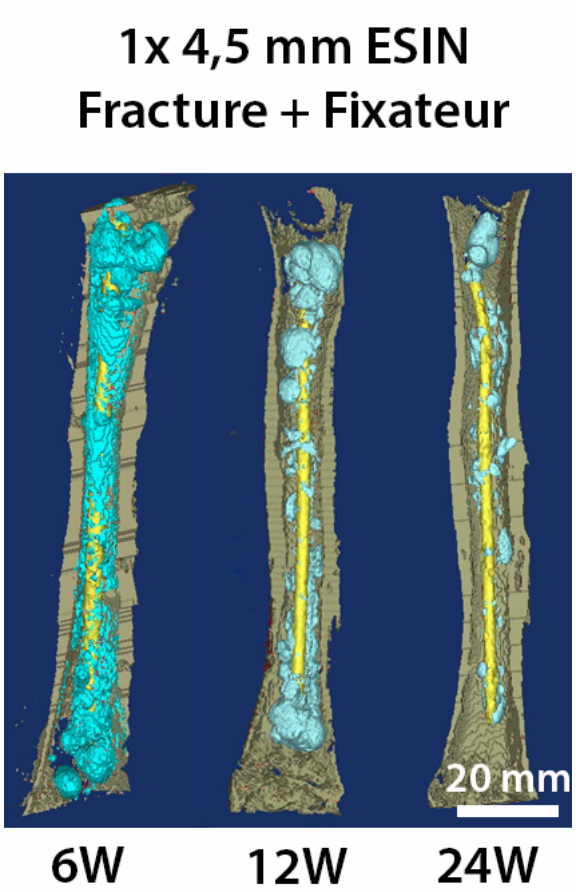

Figure 3.39: Evaluation of CT data with 4.5 mm ESIN, fracture and external fixation was started after the removal of the fixation device at week 6. Initially high gas formation was continously decreasing until 12W and 24W. Fracture healing resulted in a stable reunion already after 6 weeks.

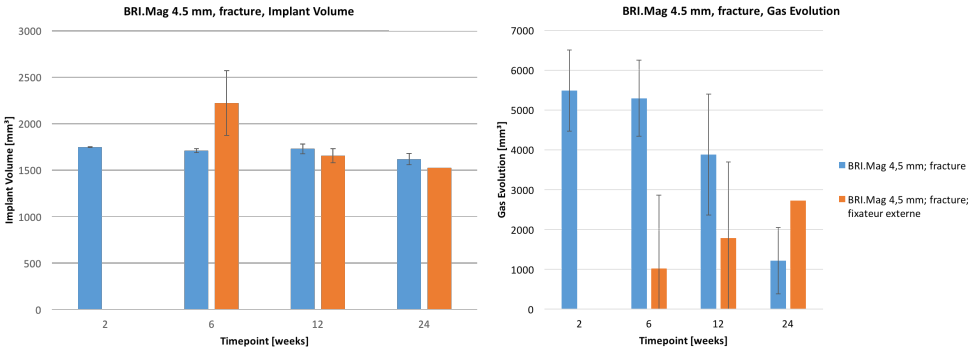

Figure 3.40: Numerical evaluation of clinical CT data was performed from week 2 to week 24 for cast support. Fixateur externe data was evaluated beginning from week 6 to exclude improper measurement caused by metallic artifacts from the fixation device.

3.6 Aim 6: Micro CT ex vivo characterization of BRI.Mag® screws in ovine metaphyseal, epiphyseal and diaphyseal tibia

Unpoished and polished BRI.Mag® screws were implanted into sheep tibiae at different locations in cortical and trabecular bone areas. Four unpolished screws were placed over the whole diaphysis like displayed in fig. 3.41. One screw head in fig. 3.41 b) broke off through too high torque at insertion. Another two screws were inserted into the trabecular bone region of the proximal metaphysis like in fig. 3.42. Three polished screws were inserted into another animals tibia with three diaphyseal screws (see fig. 3.43), two screws in the proximal metaphysis and another screw in the distal epiphysis, like shown in 3.44.

Unpolished screws show a very close bone contact and intense new bone formation

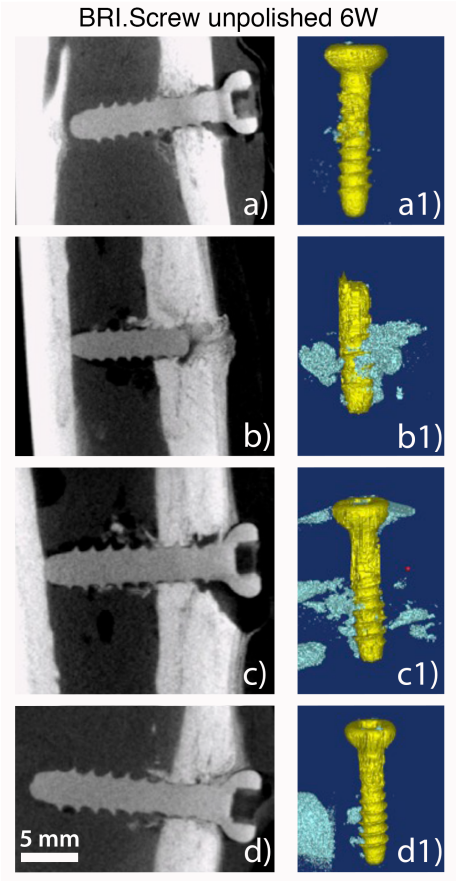

Figure 3.41: Four unpolished BRI.Screws were implanted in the diaphysis of the sheep tibia and explanted and scanned in μCT after 6W. a) shows a very low amount of gas and also a tight implant interface formation which is also seen on d). Screw heads broke off on image b) due to too high torque at insertion. c) shows a gap around the screw head, which may be a result of the drilling procedure. 3D rendering a1)-d1) show the surrounding amount of hydrogen gas.

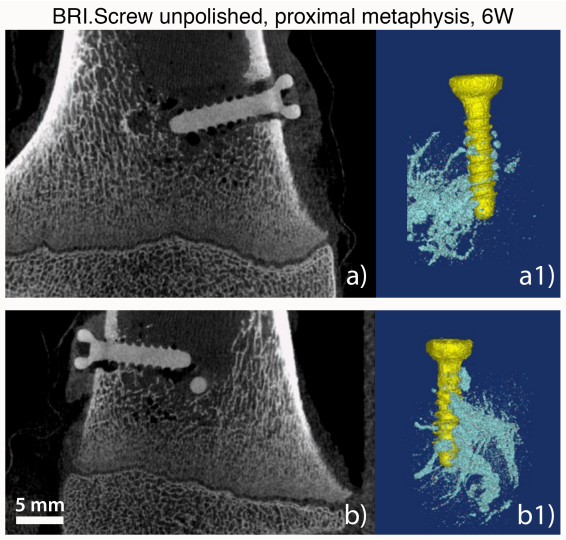

Figure 3.42: Two unpolished screws were implanted into proximal methaphyseal area to simulate an ESIN interlocking screw with plug systems. Slightly higher amounts of gas were noticed within this area in a1) and b1). Lower bone contact can be seen in a), an increasing interface is visible in b).

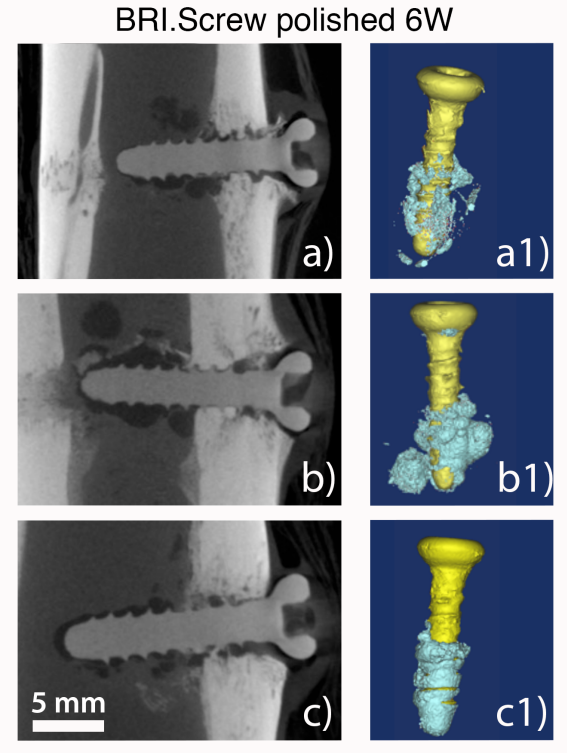

Figure 3.43: Three polished screws were implanted to the diaphyseal region showing a lower bone contact in pictures a) and b), together with a higher hydrogen amount on a1)-c1). An overlay of the screw head by the periosteum can be noticed in a).

around the implants in fig. 3.41. Only slight gas formation was noticed within the diaphyseal area, while the screws within the trabecular regions showed slightly higher amounts in fig. 3.42.

Polished screws exhibited a higher gas production after 6W in vivo on diaphyseal and meta-/epiphyseal images in fig. 3.43 and fig. 3.44. Also less tight bone contact was noticed on μCT images 3.43 a) and c).

The numerical evaluation of μCT data in fig. 3.45 shows slightly higher screw volumes for the unpolished versions in trabecular and cortical bone. The surface area

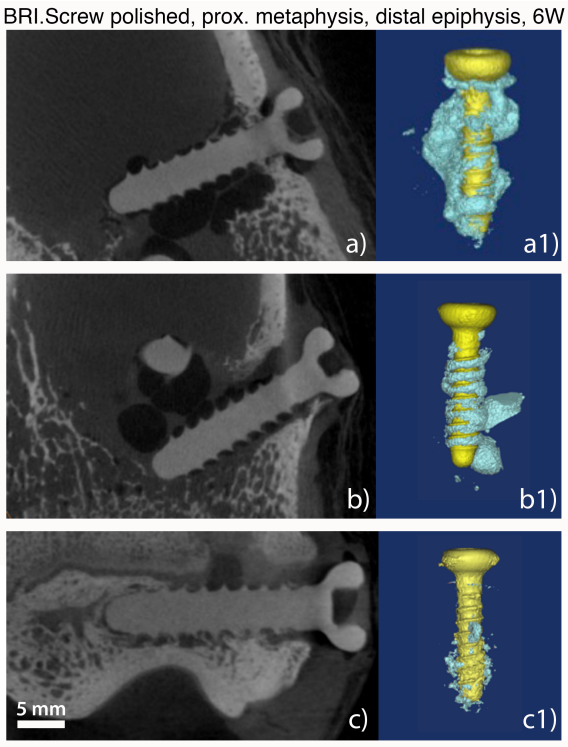

Figure 3.44: Two polished screws were inserted proximally in the same way as already performed for the unpolished versions. Additionally, one screw was implanted at the distal epiphysis, which shows a close bone incorporation with low gas amount in c) and c1). Greater hydrogen cavities were seen in a1) and b1).

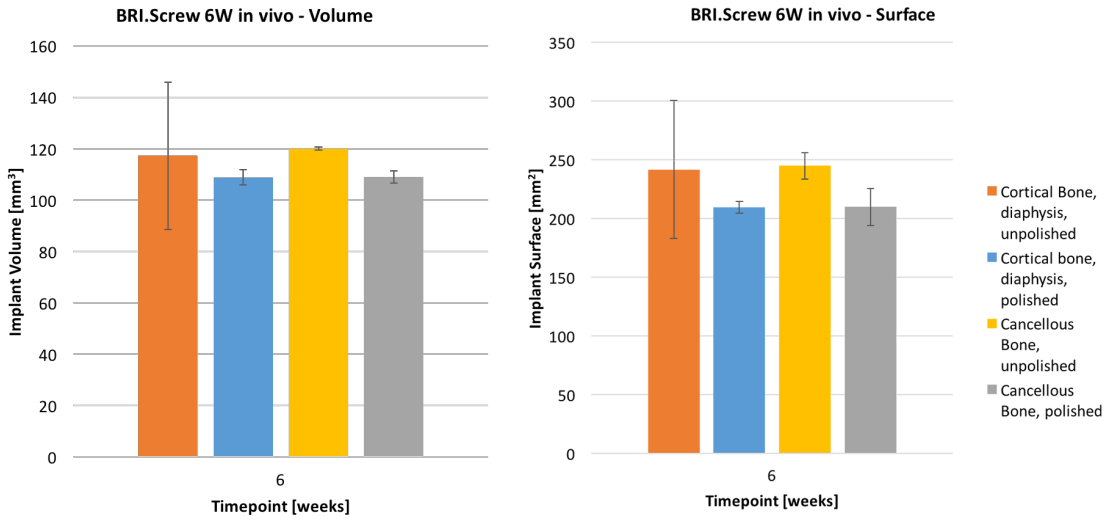

Figure 3.45: Numerical data from μCT evaluation shows slightly lower surface areas and implant volumes for the polished versions.

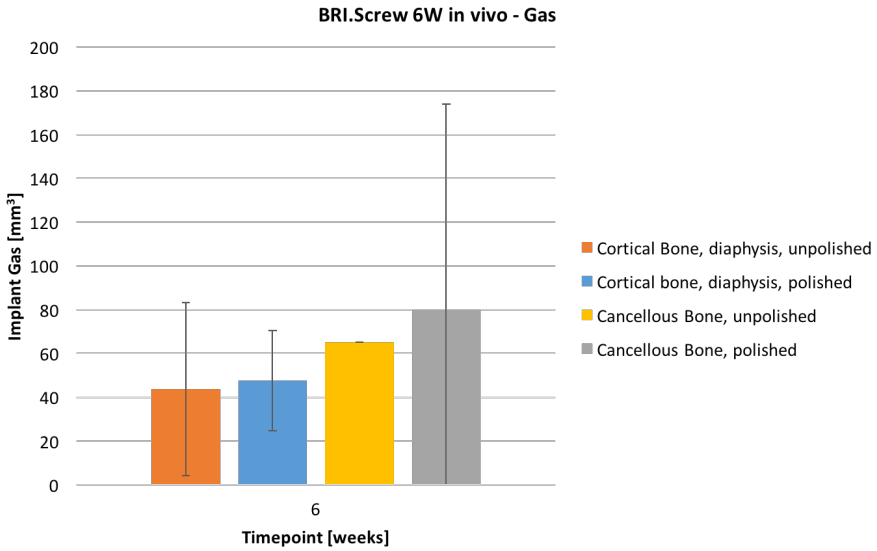

Figure 3.46: The produced amount of hydrogen gas was measured to be higher for the polished screws which corresponds to the μCT images.

was also noticed to be lower for the polished screws, which indicates the smoothing influence of the polishing process. A slight increase in gas development in fig. 3.46 was measured for the polished screws, especially in the trabecular epi- and metaphyseal areas.

4 Discussion

4.1 Aim 1: Radiological observation of degradation and interface characteristics of Polyhydroxybutyrate (PHB) composite materials

All evaluated PHB composite materials in aim 1 exhibited no noticeable degradation during the whole study period of 36 weeks. They rather seemed to gain volume after 12W, 24W and 36W in vivo already described in literature for PLGA by Dumitru et al. [56]. This behaviour was caused by diffusion and uptake of solvent molecules and may be an explanation for this behaviour of PHB composites too. Generally, very long degradation times were reported for polymers used in the medical industry in Eglin et al. [57]. Poly-Glycolic-Acid (PGA), Poly-L-Lactic-Acid (PLLA) and also Poly-Lactic-Co-Glycolic-Acid (PLGA) were described with degradation rates up to 52 weeks and even more for PLLA, which is also expected for the observed PHB composites. Saito et al. published a study, where PHB granules were injected directly into organs like spleen, liver and lung of rats [58]. Especially in the liver, high PHB degradation rates were monitored within two months. Due to the fact

that PHBs degradation process needs an enzymatic reaction [57], the implantation site within a cortical rat bone may lack of those enzymes. Actually it is still unclear how the enzymatic environment is stated in this area. The bone substitute material Herafill® was added to the slow degrading PHB material in order to induce bone accumulation and enhance the degradation rate. From a radiological point of view, polymers exhibit low density and are not able to produce distinct contrast differences, as the X-ray photon energy is not reduced sufficiently. For this reason, they may not be an ideal implant material for observation in CT or X-ray imaging, especially when using in vivo scans. Native PHB was hardly visible during longitudinal μCT scans, which made a suitable quantification of implant volume and development impossible. However, the evaluation of bone ingrowth could also be done with low contrast data. To achieve better radiological information, the contrast medium ZrO_2 was added to the composite and resulted in a remarkable enrichment of image contrast. Additionally the numerical evaluation of bone ingrowth resulted in highest values of $\frac{BV}{TV}$ for the combination of Herafill and ZrO_2, while the ZrO_2 only material P3Z did not show any organic tissue on its surface on REM images published in Meischel and Eichler et al. [1]. In terms of the most important requirements for the choice of suitable implant materials, which are growth of callus, cartilage and bone tissue (published in Papakyriacou et al. [59]), all examined PHB composites except P3Z30H, were considered as unsuitable for degradable orthopaedic load bearing implants in Meischel and Eichler et al. [1].

4.2 Aim 2: Characterization of degradation behaviour of biodegradable iron (Fe) alloys under assessment of μCT based volume and surface data in vivo

The assessment of biodegradable Fe alloys within a growing rat model was performed in μCT with adapted scanning parameters for very dense materials. Only high resolution imaging was considered to ensure a distinct evaluation of changes in surface area and implant volume over a period of 52 weeks. Pure Fe and alloys containing Manganese (Mn) were already observed within in vitro test setups in Hermawan et al. [16] and also in an in vivo rabbit model in Peuster et al. [14]. Those publication show an highly increased degradation rate in vitro compared to in vivo, where pure Fe stents were still present after 18 months [14]. An increase also in in vivo degradation was expected by Hermawan et al. [16] through the additional alloying of Mn. Another enhancement of degradation rate was hypothesized by Schinhammer et al. [49] with the induction of microgalvanic corrosion due alloying of Palladium (Pd). For this in vivo study the two alloys Fe-10Mn-1Pd and Fe-21Mn-0.7C-1Pd were selected, where the latter is expected to show enhanced strength and ductility in comparison to Fe and Fe-10Mn-1Pd and was examined in vitro by Schinhammer et al. [49]. However, lower degradation rates were expected in vivo, like examined by Witte et al. [60] for biodegradable Mg alloys too. To ensure a distinct measurement with high resolution μCT scans, explanted bone samples had to be used precautions to avoid metallic artifacts by beam hardening [9, 12, 61]. Created high resolution μCT scans could be successfully evaluated concerning implant shapes including small details on the surface (see fig. 3.6 b) and e)) after beam hardening reduction by 1.5 mm aluminium filtration.

Evaluated numerical values for implant volume showed a maximum decrease of 0.5 mm^3 within 48 weeks in vivo. Accuracy of measurements may be sill limited by the remaining metallic artifacts [2]. The corresponding macroscopic images 3.9, 3.10, 3.11 and 3.12 show the formation of a corrosion layer which seems to be darker after week 24. A possible explanation for the slow in vivo degradation, may be the missing oxygen concentration in the surrounding tissue which is needed for the oxidation of built ferrous oxides (Fe^{2+}) to ferric oxides (Fe^{3+}), as described in Kraus et al. [2]. The formed protective layer containing Phosphor (P) and Calcium (Ca) may influence the degradation velocity as stated in [2].

4.3 Aim 3: Fluorescence Molecular Tomography (FMT) in transcortical rat model with osteoclast and osteoblast activity labelling fluorescent imaging agents in combination with micro CT imaging

Radiological μCT imaging has been mentioned frequently as an exact method for the characterisation of degradation characteristics and also bone morphology. The distinct representation of small structures and bone-implant interfaces is a huge benefit of this technology. However, distinguishing between new bone structures, degradation products of Mg implants and implant residuals gets more and more challenging due to very similar contrast values during in vivo imaging. A graphical distinction between new and old bone structures would be desirable. Those molecular processes can not be directly measured with the Siemens Inveon μCT device without an additional positron-emission tomography (PET) scanner. Furthermore,

the production, storage and handling of radionuclide tracers is non trivial and needs special facility equipment and skilled staff. FMT imaging allows to select a suitable molecular tracer and offers a possibility to examine molecular procedures in vivo. For the special purpose of assessing biodegradable implants in a growing rat skeleton, a fluorescent tracer for osteoblast activity was used to quantify bone remodelling according to Zaheer et al. in [62]. A validation of those tracers in combination with the used Perkin Elmer FMT 2500 has been published for rats by Vonwil et al. [63]. Osteosense 750EX was successfully used in Zilberman et al. [64] to assess the healing of non union fractures in mice by engineerd mesenchymal stem cells. Measured fluorescence intensity and area of hydroxyapatite (HA) bonding was proven to correspond with the μCT measurements of bone volumes.

FMT measurements of experimental animal groups resulted in baseline values of fluorescence intensities within the control group KM. Differences in baseline may be affected by growth stages in the used young rats during the monitored time points. The SHAM group SM was measured after applying only a drill through both tibiae without insertion of any implant. Measured fluorescence values were almost doubled in comparison to the KM group's baseline values. The other experimental groups with Mg-10Gd (GD) implants and BRI.Mag (BR) implants showed a quite similar behaviour to the SM group until week 5. The GD group experienced a huge increase in fluorescence intensity at week 8, decreasing slightly at week 10. A possible explanation of this behaviour may be the incorporation of gadolinium into surrounding bone tissue, which was also examined for clinical contrast media by Darrah et al. and Ramalho et al. [65, 66] during a phase of high release. A second theory may be the increased amount of bone remodelling induced by the high corrosion rate of the material, which seems reasonable in fig. 3.15. Kraus et al. published the extensive degradation and hydrogen gas formation for the material ZX50 in [67], which was followed by a complete restitutio ad integrum of the distorted bone.

Besides the measurement of fluorescence intensity, μCT scans of the lower limbs of the animal were conducted using the supplied rat imaging cassette with markers for FMT co-registration (see fig.3.15). Due to a too small FOV of the Siemens Inveon device in lowest magnification setting, the cassette could not be imaged using at least three markers for co-registration like performed in Jermin et al. and Vonwil et al. [68, 63].

4.4 Aim 4: Micro CT supported biomechanical evaluation of ESIN interlocking systems in cadaveric sheep tibiae

The overall mechanical stability of ESIN interlocking systems was evaluated using biomechanical tests in combination with μCT data and the displacement value by measuring the risen cavity after screw pull-out. Especially in case of ender nails, μCT data may lack in accuracy due to beam hardening artifacts around the stainless steel implant (see fig. 3.17). Also a bending of the fixation screw(s) or the ESIN nail within the plug can be considered in order to suggest a failure mode for the different systems. The smallest measured screw displacement was calculated for 3.0 plug systems (see fig. 3.19) which may be an obvious result considering the fact that the screw heads broke off during loading and there was no heavy screw pull out possible anymore. The highest internal bone damage was caused by the ender nail, which may be a result of the freely moving screw in the eye of the ender nail and the resulting forces. In contrary, the angle stable TwinPlug, FixPlug and 3.5 Plug systems may add resistance to oblique pull out forces and therefore a higher resistance against internal bone damage. The biomechanical analysis was performed by DI Leopold Berger and the prescribed analysis method of micro CT data was

performed by the diploma student Jonathan Ryll.

4.5 Aim 5: Clinical CT imaging of degradable Magnesium ESIN implants in the growing sheep model

Several stages of material quality were tested in a sheep model. Inspired by common Ti implants for clinical ESIN osteosynthesis, 3 mm nails were manufactured out of the alloys BRI.Mag® and ZX10. Those implants were used for intramedullary application without any fracture and crossing the epiphyseal plate. No special surface treatment was applied in this material stage. Results of BRI.Mag® in group G1 (see fig. 3.21) show the formation of hydrogen gas during in vivo degradation, which is known as a common effect through Mg corrosion in aqueous solutions [69, 39]. First hydrogen gas cavities appeared already after week 2. The highest level of intramedullary gas bubbles was reached after week 12, which is also the time point where first superficial degradation signs can be noticed on human CT scans (see fig. 3.23). Superficial pitting corrosion may have appeared in advance on the untreated surface or even may have been initiated by the operation process, where the implant is fixed in a T-handle during insertion via a lateral approach. The effect of pitting corrosion and fatigue cracks was also demonstrated for AZ91 alloys by Rozali et al. [70]. The hydrogen gas formation of ZX10 implants exhibited a more constant behaviour for steadily increasing gas volumes until week 52. The chemical compositions of BRI.Mag® (Mg-0.3Zn-0.4Ca) and ZX10 (Mg-1Zn-0.3Ca) only differ in 0.7 % of Zn and 0.1 % Ca. One possible explanation of the lower corrosion rate of ZX10 may be an increased ductility by the markable higher Zn content of the alloy, which increases its resistance against mechanical influences during the

surgical procedure [71, 72]. Another possibility is given by a probably lower grain size, which is also a known consequence of alloying Zn and leads to lower and more homogeneous degradation [72]. After 52W and 76w in vivo, gas formation was retarded and clearly visible bone islets were examined in inside the medullary cavity. This behaviour may be a result of the degradation product Magnesium Hydroxide Mg-OH, which was mentioned to act as osteoblast activity enhancing material in Janning et al. [19]. Injuries of the growth plate may induce the formation of bone bridges (see Pichler et al. in [73]), depending on the defect size within the epiphysis. Standard paediatric ESIN osteosynthesis by two single nails often needs to be performed crossing the physis was explained to do not cause any growth disturbance in Metaizeau et al. [23]. However, the implantation of 3 mm BRI.Mag® and ZX10 ESIN nails through the epiphyseal plate did not influence the bone length in comparison to the control animals in fig. 3.26, despite high gas formation in the epiphyseal areas. A high degradation activity was also noticed within this area for group G4, where the same 3 mm BRI.Mag® rods were implanted transcortically in proximal and distal epiphyseal sites. The higher gas formation after week 2 may be a direct consequence of higher vascularisation and metabolic activity within this area, especially after epiphyseal injury [74]. Also in this case, no rest of growth was detected and the proximal and distal implants were transported away from the epiphyses during growth. Unilateral, proximal development in bone length may also have caused implant breach after 52W in fig. 3.29.

A clinical study of Khallaf et al. [75] shows an average healing time for long bone fractures of 6.9 weeks for adults around 30 years age. The transcortical Mg implant in the diaphyseal area shows the highest callus formation at 12W, the Ti control group did not show comparable callus formation at the same time before metal removal. The conducted fracture study with 3 mm BRI.Mag® ESIN material and external fixation shows exactly this healing behaviour in fig. 3.32, where a fully consolidated callus was built up between week 6 and week 12. However, the used

animal model is actually a growing skeleton, which usually shows a higher healing rate in humans. To apply a suitable fracture stabilization by ESIN osteosynthesis, which was only possible with additional external fixation for the 3 mm nails in G6, implant diameter was increased to 4.5 mm. The application was changed from two single nails to one nail, which can be implanted through a lateral approach. BRI.Mag 4.5 mm implants were additionally surface treated by grinding, which should remove impurities from the manufacturing process. A lower initial degradation and also a more homogeneous attack over time was expected by removal of micro-galvanic corrosion pits induced by surface impurities also mentioned in Waizy et al. [76]. The simple grinding procedure lowered the average hydrogen formation within the medullary cavity by around one half. Except at week 24, where intense bulk release of gas was examined for the unpolished material. Further implantations were done with polished BRI.Mag® 4.5 and fractures were produced within groups G8 and G9 to assess load bearing and fracture healing of the ESIN osteosynthesis. Stabilization of tibia osteotomy was successful in n=2 out of 7 animals with support of a cast. Unlike human beings, sheep apply full loading on the fractured leg as a getaway reflex, which could not be compensated by the cast-implant combination in all cases. However, the application of an additional external fixation was pretty stable but led to further problems and loss of experimental animals by infections. After 6W in vivo, the fracture healing was almost solid with a visible fracture gap in fig. 3.38. This was comparable to clinical results in Khallaf et al. [75]. The external fixation had a positive influence on the initial bone healing until removal at week 6. No visible fracture gap could be noticed anymore. However, damage of the implants may occure during insertion of bicortical fixateur pins, which leads to increased corrosion. Also radiological observation was not possible without distortion until metal removal at week 6.

4.6 Aim 6: Micro CT ex vivo characterization of BRI.Mag® screws in ovine metaphyseal, epiphyseal and diaphyseal tibia

The polished and unpolished 16 mm long BRI.Screws were implanted and imaged in clinical CT after week 2 and week 6. The clinical CT results with the quite low resolution of 0.6 mm per voxel were used for qualitative analysis during the study. Distinct measurement in μCT imaging could show detailed views of differences in bone contact and also gas evolution. A tight bone-implant interface with very low gas formation in the surrounding tissue was experienced for unpolished BRI.Screws in cortical diaphysis. The quick overgrow of periosteum in 3.41 a) and d) may be a sign for beginning bone formation around the screw head, like examined in Chaya et al. [77]. The lower bone contact in the trabecular region of the proximal metaphysis in fig. 3.42 is comparable to the bone incorporation of implants in Chaya et al. and Schaller et al. [78]. Chemically polished BRI.Screws exhibit a lower bone contact in fig. 3.43 including small gaps and gas cavities around the implants. A possible explanation for this result is the volume loss caused by the chemical polishing process in combination with slight movements of the screws by influence of the surrounding soft tissue. Higher gas evolution along the threads inside the medullary cavity may be a result of non optimal chemical polishing or also over-etching of the surface which may lead to new pitting corrosions.

5 Conclusion

Two different aspects were addressed within this work: On the one hand, several imaging methods were shown in order to achieve a maximum of information about the degradation performance of different biomaterials. On the other hand, those biomaterials were characterised and tested according to their clinical suitability by the parameters gained through used imaging methods.

5.1 Imaging

Most of the radiological methods within this work were conducted using X-ray source and the corresponding photon radiation, which may result in unwanted side effects by the application of high patient, or in our case, animal doses. In vivo scans were applied at different time points during all studies with best effort details and a minimized radiation dose, in order to avoid any damage or emerging cancer. However, the development of one or more soft tissue tumors in the Sprague Dawley® rat model is very likely after a long study period of about two years. Two different scanning protocols were measured by dosimetry and the certificates were added to the appendix section. Mitsumatsu et al. [79] published a significant decrease of proliferating cells and immature neurons in rats after applying a dose of 2 Gy. 2.3 Gy were also found to influence the visual cortex in Davis et al. [80]. More influ-

ences in inflamed connective tissue were published by Maximow in 1923 [81]. A very high radiation value of 2.759 Gray (Gy) was emitted within one μCT scan using a very accurate and protocol which will deliver optimal contrast. For standard in vivo examination, a low dose protocol with 1.159 Gy is recommended, especially when the study needs to be conducted over a long time with the used animals. In contrast to high radiation emitting μCT scans, the clinical CT protocol was run with a dose of 13.42 mGy, which is still 90% higher than the dose of a usual patient scan. This protocol is highly recommended to achieve a maximum of possible contrast and details. Both methods showed high applicability to achieve detailed images of bioresorbable and non-bioresorbable, metallic implants during this study. However, small structures like screw threads or the formation of new bone have to be examined ex vivo in μCT imaging to achieve reliable and quantifiable results. Dense metallic materials like stainless steel or Ti may be imaged in both technologies depending on the implant size. However, beam hardening filtration is able to reduce artifacts around the implants but a distinct observation of the implant's surrounding may be problematic. On the other hand, the precise imaging of polymers like PHB is challenging because of their low radiological density. For quantification bone morphology and also implant characteristics, ex vivo evaluation with high resolution μCT is highly recommended.

Fluorescence molecular tomography showed interesting results for the in vivo assessment of molecular processes. The ability to quantify those activities like the new bone forming osteoclast actions directly at the implant sites provide a useful supplement to radiological imaging. Actually the fluorescent tracers are usually administered in mice and are rather expensive when considering the needed dose in a rat model. However, the method was already validated by Vonwil et al. [63]. This method may also be interesting for further in vivo studies regarding Mg implants in an osteoporotic environment where bone tracers (Osteosense for osteoblasts, Cathepsine K for osteoclasts) and also vascular and inflammatory tracers (Angiosense) may

give new insights in osteoporosis procedures.

5.2 Implants

Results of Fe an PHB implants were already published in Kraus et al. [2] and Meischel and Eichler et al. [1]. Both materials did not show suitable characteristics for a further application as degradable implants. Also the examined implant material Mg10Gd does not seem to achieve necessary characteristics for clinical use, which was also published by Myrissa et al. [38]. Very interesting Mg alloys are however, BRI.Mag and ZX10, which showed homogeneous and slow degradation in rat studies and was successfully upscaled to full size orthopaedic implants like ESIN rods and screws. In comparison to conventional Ti, both materials provide lower stiffness and strength, which has to be taken into account for implant design strategies and also during the surgical operation. For example, torque limiters are recommended for inserting bioresorbable BRI.Screws to avoid breaking the heads off. Also a self tapping design may ease the implantation process, although thread tapping by a thread cutting tool is recommended. For the application of ESIN nails, which may be rather used in a 4.5 mm diameter than the common 3 mm diameter, infringing of the surface during implantation should be avoided. The main goal towards the final clinical application may be achieved by the materials BRI.Mag and ZX10 and may be reached by considering an optimal manufacturing process in combination with tailored surface treatment (polishing). This will ensure key points like homogeneous degradation, together with load bearing until reconsolidation of bone with low gas formation to avoid irritation of tissue.

References

[1] M. Meischel, J. Eichler, E. Martinelli, U. Karr, J. Weigel, G. Schmöller, E. Tschegg, S. Fischerauer, a.M. Weinberg, and S. Stanzl-Tschegg, "Adhesive strength of bone-implant interfaces and in-vivo degradation of PHB composites for load-bearing applications," *Journal of the Mechanical Behavior of Biomedical Materials*, vol. 53, pp. 104–118, 2016.

[2] T. Kraus, F. Moszner, S. Fischerauer, M. Fiedler, E. Martinelli, J. Eichler, F. Witte, E. Willbold, M. Schinhammer, M. Meischel, P. J. Uggowitzer, J. F. Löffler, and A. Weinberg, "Biodegradable Fe-based alloys for use in osteosynthesis: Outcome of an in vivo study after 52 weeks," *Acta Biomaterialia*, vol. 10, no. 7, pp. 3346–3353, 2014.

[3] J. Nagels, M. Stokdijk, and P. M. Rozing, "Stress shielding and bone resorption in shoulder arthroplasty.," *Journal of shoulder and elbow surgery / American Shoulder and Elbow Surgeons ... [et al.]*, vol. 12, pp. 35–9, jan 2003.

[4] H. Windhagen, K. Radtke, A. Weizbauer, J. Diekmann, Y. Noll, U. Kreimeyer, R. Schavan, C. Stukenborg-Colsman, and H. Waizy, "Biodegradable magnesium-based screw clinically equivalent to titanium screw in hallux valgus surgery: short term results of the first prospective, randomized, controlled clinical pilot study.," *Biomedical engineering online*, vol. 12, no. 1, p. 62, 2013.

[5] R. a. Lindtner, C. Castellani, S. Tangl, G. Zanoni, P. Hausbrandt, E. K. Tschegg, S. E. Stanzl-Tschegg, and A. M. Weinberg, "Comparative biomechanical and radiological characterization of osseointegration of a biodegradable magnesium alloy pin and a copolymeric control for osteosynthesis," *Journal of the Mechanical Behavior of Biomedical Materials*, vol. 28, pp. 232–243, 2013.

[6] M. Reiser, F.-P. Kuhn, and J. Debus, *Radiologie*. Duale Reihe, Stuttgart: Georg Thieme Verlag, 2011.

[7] H. Li, H. Zhang, Z. Tang, and G. Hu, "Micro-computed tomography for small animal imaging: Technological details," *Progress in Natural Science*, vol. 18, no. 5, pp. 513–521, 2008.

[8] L. A. Feldkamp, S. A. Goldstein, A. M. Parfitt, G. Jesion, and M. Kleerekoper, "The direct examination of three-dimensional bone architecture in vitro by computed tomography.," *Journal of bone and mineral research : the official journal of the American Society for Bone and Mineral Research*, vol. 4, pp. 3–11, feb 1989.

[9] J. A. Meganck, K. M. Kozloff, M. M. Thornton, M. Stephen, and S. A. Goldstein, "Beam Hardening Artifacts in Micro-Computed Tomography Scanning can be Reduced by X-ray Beam Filtration and the Resulting Images can be used to Accurately Measure BMD," *Bone*, vol. 45, no. 6, pp. 1104–1116, 2010.

[10] M. Carlo, P. Adriano, M. Francesco, R. Franco, S. J. Awad, L. Giovanna, and G. Alessandra, "Histological and Synchrotron Radiation-Based Computed Microtomography Study of 2 Human-Retrieved Direct Laser Metal Formed Titanium Implants," *Implant Dentistry*, vol. 0, no. 0, pp. 1–5, 2013.

[11] J. C. Andrews, P. Pianetta, F. Meirer, J. Chen, E. Almeida, M. C. H. Van der Meulen, J. S. Alwood, C. Lee, J. Zhu, and Y. Cui, "Hard X-ray Full Field

Nano-imaging of Bone and Nanowires at SSRL," in *AIP Conf Proc*, pp. 79–82, 2010.

[12] W. Dewulf, Y. Tan, and K. Kiekens, "Sense and non-sense of beam hardening correction in CT metrology," *CIRP Annals - Manufacturing Technology*, vol. 61, pp. 495–498, jan 2012.

[13] A. Atlić, M. Koller, D. Scherzer, C. Kutschera, E. Grillo-Fernandes, P. Horvat, E. Chiellini, and G. Braunegg, "Continuous production of poly([R]-3-hydroxybutyrate) by Cupriavidus necator in a multistage bioreactor cascade," *Applied Microbiology and Biotechnology*, vol. 91, pp. 295–304, 2011.

[14] M. Peuster, C. Hesse, T. Schloo, C. Fink, P. Beerbaum, and C. von Schnakenburg, "Long-term biocompatibility of a corrodible peripheral iron stent in the porcine descending aorta.," *Biomaterials*, vol. 27, pp. 4955–62, oct 2006.

[15] R. Waksman, R. Pakala, R. Baffour, R. Seabron, D. Hellinga, and F. O. Tio, "Short-term effects of biocorrodible iron stents in porcine coronary arteries," *Journal of Interventional Cardiology*, vol. 21, no. 1, pp. 15–20, 2008.

[16] H. Hermawan, A. Purnama, D. Dube, J. Couet, and D. Mantovani, "Fe-Mn alloys for metallic biodegradable stents: degradation and cell viability studies.," *Acta biomaterialia*, vol. 6, pp. 1852–60, may 2010.

[17] M. Schinhammer, A. C. H??nzi, J. F. L??ffler, and P. J. Uggowitzer, "Design strategy for biodegradable Fe-based alloys for medical applications," *Acta Biomaterialia*, vol. 6, no. 5, pp. 1705–1713, 2010.

[18] T. Kraus, S. F. Fischerauer, A. C. Hänzi, P. J. Uggowitzer, J. F. Löffler, and A. M. Weinberg, "Magnesium alloys for temporary implants in osteosynthesis: in vivo studies of their degradation and interaction with bone.," *Acta biomate-*

rialia, vol. 8, pp. 1230–8, mar 2012.

[19] C. Janning, E. Willbold, C. Vogt, J. Nellesen, A. Meyer-Lindenberg, H. Windhagen, F. Thorey, and F. Witte, "Magnesium hydroxide temporarily enhancing osteoblast activity and decreasing the osteoclast number in peri-implant bone remodelling," *Acta Biomaterialia*, vol. 6, no. 5, pp. 1861–1868, 2010.

[20] T. McKinley, "Principles of Fracture Healing," *Surgery (Oxford)*, vol. 21, pp. 209–212, sep 2003.

[21] P. Lascombes, H. Huber, R. Fay, D. Popkov, T. Haumont, and P. Journeau, "Flexible intramedullary nailing in children: nail to medullary canal diameters optimal ratio.," *Journal of pediatric orthopedics*, vol. 33, pp. 403–8, jun 2013.

[22] N. E. Bishop, M. van Rhijn, I. Tami, R. Corveleijn, E. Schneider, and K. Ito, "Shear does not necessarily inhibit bone healing.," *Clinical orthopaedics and related research*, vol. 443, no. 443, pp. 307–14, 2006.

[23] J. P. Metaizeau, "Stable elastic intramedullary nailing for fractures of the femur in children.," *The Journal of Bone & Joint Surgery [Br]*, vol. 86, no. 7, pp. 954–957, 2004.

[24] J. Nyman, S. Munoz, S. Jadhav, a. Mansour, T. Yoshii, G. Mundy, and G. Gutierrez, "Quantitative measures of femoral fracture repair in rats derived by micro-computed tomography," *Journal of biomechanics*, vol. 42, no. 7, pp. 891–897, 2009.

[25] S. J. Shefelbine, U. Simon, L. Claes, A. Gold, Y. Gabet, I. Bab, R. Müller, and P. Augat, "Prediction of fracture callus mechanical properties using micro-CT images and voxel-based finite element analysis," *Bone*, vol. 36, no. 3, pp. 480–488, 2005.

[26] K. Baldwin, J. E. Hsu, D. R. Wenger, and H. S. Hosalkar, "Treatment of femur fractures in school-aged children using elastic stable intramedullary nailing: a systematic review.," *Journal of pediatric orthopaedics. Part B / European Paediatric Orthopaedic Society, Pediatric Orthopaedic Society of North America*, vol. 20, no. 5, pp. 303–308, 2011.

[27] L. Berger, S. Fischerauer, B. Weiß, A. Celarek, C. Castellani, A.-M. Weinberg, and E. Tschegg, "Unlocked and locked elastic stable intramedullary nailing in an ovine tibia fracture model: a biomechanical study.," *Materials science & engineering. C, Materials for biological applications*, vol. 40, pp. 267–74, jul 2014.

[28] K. Hora, K. P. Vorderwinkler, V. V??csei, and C. G??bler, "Entfernung von verriegelungsn??geln an der oberen und unteren extremit??t: Soll diese operation generell empfohlen werden?," *Unfallchirurg*, vol. 111, no. 8, pp. 599–606, 2008.

[29] B. Hanson, C. van der Werken, and D. Stengel, "Surgeons' beliefs and perceptions about removal of orthopaedic implants.," *BMC musculoskeletal disorders*, vol. 9, p. 73, 2008.

[30] E. A. Gorter, D. I. Vos, C. F. M. Sier, and I. B. Schipper, "Implant removal associated complications in children with limb fractures due to trauma," *European Journal of Trauma and Emergency Surgery*, vol. 37, no. 6, pp. 623–627, 2011.

[31] J. Eichler, S. F. Fischerauer, E. Martinelli, A. Myrissa, T. Kraus, L. Berger, P. J. Uggowitzer, J. F. Löffler, and A.-M. Weinberg, "Pre-clinical characterization of full-size bioresorbable magnesium osteosynthesis implants in a growing sheep model," *European Cells and Materials*, vol. 30, no. Supplement 3, 2015,

p. 103, 2015.

[32] J. Hofstetter, M. Becker, E. Martinelli, a. M. Weinberg, B. Mingler, H. Kilian, S. Pogatscher, P. J. Uggowitzer, and J. F. Löffler, "High-Strength Low-Alloy (HSLA) Mg–Zn–Ca Alloys with Excellent Biodegradation Performance," *Jom*, vol. 66, no. 4, pp. 566–572, 2014.

[33] J. Hofstetter, E. Martinelli, S. Pogatscher, P. Schmutz, E. Povoden-Karadeniz, a.M. Weinberg, P. Uggowitzer, and J. Löffler, "Influence of trace impurities on the in vitro and in vivo degradation of biodegradable Mg–5Zn–0.3Ca alloys," *Acta Biomaterialia*, pp. 0–6, 2015.

[34] A. Göpferich, "Mechanisms of polymer degradation and erosion," *Biomaterials*, vol. 17, no. 2, pp. 103–114, 1996.

[35] C. S. K. Reddy, R. Ghai, Rashmi, and V. C. Kalia, "Polyhydroxyalkanoates: An overview," *Bioresource Technology*, vol. 87, pp. 137–146, 2003.

[36] M. Meischel, S. Tschegg, L. Berger, E. Tschegg, L. Fischer, T. Prohaska, E. Martinelli, and A. Weinberg, "Biodegradable bone implants," in *Jahrestagung der Deutschen Gesellschaft für Biomaterialien in Erlangen*, (Erlangen), 2013.

[37] E. Martinelli, *Dissertation Intramedullary application of novel bioresorbable implants in the growing rat for osteosynthesis*. Doctoral thesis, Medical University of Graz, 2015.

[38] A. Myrissa, N. Ahmad, Y. Lu, E. Martinelli, J. Eichler, G. Szakács, C. Kleinhans, R. Willumeit-römer, U. Schäfer, and A.-m. Weinberg, "In vitro and in vivo comparison of binary Mg alloys and pure Mg," *Materials Science & Engineering C*, vol. 61, pp. 865–874, 2016.

[39] J. Hofstetter, E. Martinelli, A. M. Weinberg, M. Becker, B. Mingler, P. J. Ug-

gowitzer, and J. F. Löffler, "Assessing the degradation performance of ultrahigh-purity magnesium in vitro and in vivo," *Corrosion Science*, vol. 91, pp. 29–36, 2015.

[40] D. P. Clark and C. T. Badea, "Micro-CT of rodents: State-of-the-art and future perspectives," *Physica Medica*, no. JUNE, 2014.

[41] S. Inveon, "Inveon ™ Operator Manual," tech. rep.

[42] G. A. Rost and P. Keller, *Die Wirkung des Lichtes auf die gesunde und kranke Haut*, pp. 1–163. Vienna: Springer Vienna, 1929.

[43] N. B. Smith and A. Webb, *Introduction to Medical Imaging*. Cambridge: Cambridge University Press, 2010.

[44] O. Watzke and W. a. Kalender, "A pragmatic approach to metal artifact reduction in CT: merging of metal artifact reduced images.," *European radiology*, vol. 14, pp. 849–56, may 2004.

[45] R. Gillani, B. Ercan, A. Qiao, and T. J. Webster, "Nanofunctionalized zirconia and barium sulfate particles as bone cement additives," *International Journal of Nanomedicine*, vol. 5, pp. 1–11, 2010.

[46] X. Gu, Y. Zheng, Y. Cheng, S. Zhong, and T. Xi, "In vitro corrosion and biocompatibility of binary magnesium alloys," *Biomaterials*, vol. 30, no. 4, pp. 484–498, 2009.

[47] M. Franceschini, A. Di Matteo, H. Bösebeck, H. Büchner, and S. Vogt, "Treatment of a chronic recurrent fistulized tibial osteomyelitis: Administration of a novel antibiotic-loaded bone substitute combined with a pedicular muscle flap sealing," *European Journal of Orthopaedic Surgery and Traumatology*, vol. 22, pp. 245–249, 2012.

[48] S. Liu, J. Broucek, a. S. Virdi, and D. R. Sumner, "Limitations of using micro-computed tomography to predict bone-implant contact and mechanical fixation," *Journal of Microscopy*, vol. 245, no. 1, pp. 34–42, 2012.

[49] M. Schinhammer, P. Steiger, F. Moszner, J. F. Löffler, and P. J. Uggowitzer, "Degradation performance of biodegradable FeMnC(Pd) alloys.," *Materials science & engineering. C, Materials for biological applications*, vol. 33, pp. 1882–93, may 2013.

[50] F. Vohra, M. Q. Al-Rifaiy, K. Almas, and F. Javed, "Efficacy of systemic bisphosphonate delivery on osseointegration of implants under osteoporotic conditions: Lessons from animal studies.," *Archives of oral biology*, vol. 59, pp. 912–920, sep 2014.

[51] J. Jarrell, J. Morin, K. O. Vasquez, G. Cuneo, B. Bao, S. Kossodo, and J. D. Peterson, "Imaging of Cathepsin K activity in rodent models of bone turnover and soft tissue calcification," no. 800, p. 4602, 2009.

[52] M. a. Gentile, D. Y. Soung, C. Horrell, R. Samadfam, H. Drissi, and L. T. Duong, "Increased fracture callus mineralization and strength in cathepsin K knockout mice.," *Bone*, vol. 66C, pp. 72–81, jun 2014.

[53] A. M. Weinberg and H. Tscherne, *Unfallchirurgie im Kindesalter, Volume 1.* Springer Science & Business Media, 2006.

[54] I. Marzi, *Kindertraumatologie*. Berlin, Heidelberg: Springer Berlin Heidelberg, 2010.

[55] J. Guillen, "FELASA guidelines and recommendations.," *Journal of the American Association for Laboratory Animal Science : JAALAS*, vol. 51, no. 3, pp. 311–21, 2012.

[56] a. C. Dumitru, F. M. Espinosa, R. Garcia, G. Foschi, S. Tortorella, F. Valle, M. Dallavalle, F. Zerbetto, and F. Biscarini, "In situ nanomechanical characterization of the early stages of swelling and degradation of a biodegradable polymer," *Nanoscale*, vol. 7, no. 12, pp. 5403–5410, 2015.

[57] D. Eglin and M. Alini, "Degradable polymeric materials for osteosynthesis: Tutorial," *European Cells and Materials*, vol. 16, pp. 80–91, 2008.

[58] T. Saito, K. Tomita, K. Juni, and K. Ooba, "In vivo and in vitro degradation of poly(3-hydroxybutyrate) in rat," *Biomaterials*, vol. 12, no. 3, pp. 309–312, 1991.

[59] M. Papakyriacou, "Effects of surface treatments on high cycle corrosion fatigue of metallic implant materials," *International Journal of Fatigue*, vol. 22, pp. 873–886, 2000.

[60] F. Witte, J. Fischer, J. Nellesen, H. A. Crostack, V. Kaese, A. Pisch, F. Beckmann, and H. Windhagen, "In vitro and in vivo corrosion measurements of magnesium alloys," *Biomaterials*, vol. 27, pp. 1013–1018, 2006.

[61] O. Watzke and W. a. Kalender, "A pragmatic approach to metal artifact reduction in CT: merging of metal artifact reduced images.," *European radiology*, vol. 14, pp. 849–56, may 2004.

[62] a. Zaheer, R. E. Lenkinski, a. Mahmood, a. G. Jones, L. C. Cantley, and J. V. Frangioni, "In vivo near-infrared fluorescence imaging of osteoblastic activity.," *Nature biotechnology*, vol. 19, pp. 1148–54, dec 2001.

[63] D. Vonwil, J. Christensen, S. Fischer, O. Ronneberger, and V. P. Shastri, "Validation of fluorescence molecular tomography/micro-CT multimodal imaging in vivo in rats," *Molecular Imaging and Biology*, vol. 16, no. 3, pp. 350–361, 2014.

[64] Y. Zilberman, I. Kallai, Y. Gafni, G. Pelled, S. Kossodo, W. Yared, and D. Gazit, "Fluorescence molecular tomography enables in vivo visualization and quantification of nonunion fracture repair induced by genetically engineered mesenchymal stem cells.," *Journal of orthopaedic research : official publication of the Orthopaedic Research Society*, vol. 26, pp. 522–30, apr 2008.

[65] T. H. Darrah, J. J. Prutsman-Pfeiffer, R. J. Poreda, M. Ellen Campbell, P. V. Hauschka, and R. E. Hannigan, "Incorporation of excess gadolinium into human bone from medical contrast agents.," *Metallomics : integrated biometal science*, vol. 1, pp. 479–88, nov 2009.

[66] J. Ramalho, R. C. Semelka, M. Ramalho, R. H. Nunes, M. AlObaidy, and M. Castillo, "Gadolinium-Based Contrast Agent Accumulation and Toxicity : An Update," *Am J Neuroradiol*, pp. 1–7, 2016.

[67] T. Kraus, S. F. Fischerauer, A. C. Hänzi, P. J. Uggowitzer, J. F. Löffler, and A. M. Weinberg, "Magnesium alloys for temporary implants in osteosynthesis: in vivo studies of their degradation and interaction with bone.," *Acta biomaterialia*, vol. 8, pp. 1230–8, mar 2012.

[68] M. Jermyn, H. Ghadyani, M. a. Mastanduno, W. Turner, S. C. Davis, H. Dehghani, and B. W. Pogue, "Fast segmentation and high-quality three-dimensional volume mesh creation from medical images for diffuse optical tomography.," *Journal of biomedical optics*, vol. 18, p. 86007, aug 2013.

[69] M. P. Staiger, A. M. Pietak, J. Huadmai, and G. Dias, "Magnesium and its alloys as orthopedic biomaterials: a review.," *Biomaterials*, vol. 27, pp. 1728–34, mar 2006.

[70] S. Rozali, Y. Mutoh, and K. Nagata, "Effect of frequency on fatigue crack growth behavior of magnesium alloy AZ61 under immersed 3.5mass% NaCl

environment," *Materials Science and Engineering A*, vol. 528, no. 6, pp. 2509–2516, 2011.

[71] R. A. Antunes and M. C. L. De Oliveira, "Corrosion fatigue of biomedical metallic alloys: Mechanisms and mitigation," *Acta Biomaterialia*, vol. 8, no. 3, pp. 937–962, 2012.

[72] a.C. Hänzi, F. Dalla Torre, a.S. Sologubenko, P. Gunde, R. Schmid-Fetzer, M. Kuehlein, J. Löffler, and P. Uggowitzer, "Design strategy for microalloyed ultra-ductile magnesium alloys," *Philosophical Magazine Letters*, vol. 89, pp. 377–390, jun 2009.

[73] K. Pichler, G. Musumeci, I. Vielgut, E. Martinelli, P. Sadoghi, C. Loreto, and A.-M. Weinberg, "Towards a better understanding of bone bridge formation in the growth plate - an immunohistochemical approach.," *Connective tissue research*, vol. 54, no. 9, pp. 408–15, 2013.

[74] R. Chung, B. K. Foster, and C. J. Xian, "The potential role of VEGF-induced vascularisation in the bony repair of injured growth plate cartilage," *Journal of Endocrinology*, vol. 221, no. 1, pp. 63–75, 2014.

[75] F. G. Khallaf, E. O. Kehinde, and S. Hussein, "Bone Healing and Hormonal Bioassay in Patients with long Bone Fractures and Concomitant Head Injury," *Medical Principles and Practice*, 2016.

[76] H. Waizy, J. M. Seitz, J. Reifenrath, A. Weizbauer, F. W. Bach, A. Meyer-Lindenberg, B. Denkena, and H. Windhagen, "Biodegradable magnesium implants for orthopedic applications," *Journal of Materials Science*, vol. 48, no. 1, pp. 39–50, 2013.

[77] A. Chaya, S. Yoshizawa, K. Verdelis, N. Myers, B. J. Costello, D.-t. Chou,

S. Pal, S. Maiti, P. N. Kumta, and C. Sfeir, "Acta Biomaterialia In vivo study of magnesium plate and screw degradation and bone fracture healing," *Acta Biomaterialia*, vol. 18, pp. 262–269, 2015.

[78] B. Schaller, N. Saulacic, T. Imwinkelried, S. Beck, E. Wei, Y. Liu, J. Gralla, K. Nakahara, W. Hofstetter, and T. Iizuka, "In vivo degradation of magnesium plate / screw osteosynthesis implant systems : Soft and hard tissue response in a calvarial model in miniature pigs," *Journal of Cranio-Maxillofacial Surgery*, vol. 44, no. 3, pp. 1–9, 2016.

[79] S. Mizumatsu, M. L. Monje, D. R. Morhardt, R. Rola, T. D. Palmer, and J. R. Fike, "Extreme Sensitivity of Adult Neurogenesis to Low Doses of Extreme Sensitivity of Adult Neurogenesis to Low Doses of X-Irradiation," *Cancer research*, vol. 63, no. 14, pp. 4021–4027, 2003.

[80] C. M. Davis, P. G. Roma, E. Armour, V. L. Gooden, J. V. Brady, M. R. Weed, and R. D. Hienz, "Effects of X-ray radiation on complex visual discrimination learning and social recognition memory in rats," *PLoS ONE*, vol. 9, no. 8, 2014.

[81] A. A. Maximow, "Studies on the Changes Produced By Roentgen Rays in Inflamed Connective Tissue.," *The Journal of experimental medicine*, vol. 37, no. 3, pp. 319–40, 1923.

Appendices